

2022-08

Kayak-specific Motion Constraints for an Improved Android Smartphone GPS/INS Navigation Solution

Harke, Kelly

Harke, K. (2022). Kayak-specific motion constraints for an improved Android smartphone GPS/INS navigation solution (Master's thesis, University of Calgary, Calgary, Canada).

Retrieved from <https://prism.ucalgary.ca>.

<http://hdl.handle.net/1880/115141>

Downloaded from PRISM Repository, University of Calgary

UNIVERSITY OF CALGARY

Kayak-specific Motion Constraints for an Improved Android Smartphone GPS/INS Navigation

Solution

by

Kelly Harke

A THESIS

SUBMITTED TO THE FACULTY OF GRADUATE STUDIES
IN PARTIAL FULFILMENT OF THE REQUIREMENTS FOR THE
DEGREE OF MASTER OF SCIENCE

GRADUATE PROGRAM IN GEOMATICS ENGINEERING

CALGARY, ALBERTA

AUGUST, 2022

© Kelly Harke 2022

Abstract

In this thesis, a Global Positioning System (GPS) / inertial navigation system (INS) smartphone navigation solution to track a kayak accurately and continuously down a river is developed, implemented, and tested. A Google Pixel 4 was used to log raw GPS, accelerometer, and gyroscope measurements. Four field datasets were collected with commercial grade GNSS receivers for a reference solution and the smartphone fixed to the deck of a kayak. Traditional closed loop loosely and tightly coupled GPS/INS algorithms were compared. Both implementations were found to perform similarly with complete satellite coverage and both degraded rapidly in the event of a GPS outage. GPS signal outages may frequently occur on a river due to vegetation, canyon walls, and water splashing over the receiver and the solution becomes reliant on the INS alone. Low-cost inertial sensors, such as those found in a smartphone, were incapable of providing an accurate solution for a long period of time during GPS outages due to the accumulation of sensor errors.

To minimize this INS error, the motion of a kayak was analyzed and constraints exclusive to kayaking were proposed to improve the solution. These kayak-specific motion constraints estimated the gyroscope bias, pitch and roll angles, and accelerometer bias based on the assumption that the kayak's pitch and roll angles are centered around zero, cyclic in nature, and return to the same orientation at regular time intervals. These motion constraints were applied to the collected datasets in a loosely coupled filter to verify this solution. The velocity and position errors during a GPS outage were improved with motion constraints as opposed to a traditional filter without motion constraints. After a simulated 20 second GPS outage on one dataset, the horizontal and vertical errors improved from 31.077 to 12.538 metres and 8.874 to 1.342 metres respectively with the motion constraints applied. This improvement was verified with three additional datasets. Therefore, the proposed kayak-specific motion constraints were found to improve the GPS/INS navigation solution, particularly during a GPS outage.

Preface

Some parts of this thesis contain materials from the conference paper:

Harke, K. and O'Keefe, K (2022) "Gyroscope Drift Estimation of a GPS/MEMS-INS Smartphone Navigation System for Kayaking", in Proceedings of ION GNSS+ 2022, 19-23 September, Denver, CO, U. S., 15 pages.

Acknowledgements

This project would not have been possible without the support from everyone throughout my graduate studies.

I would like to extend a sincere thank you to my supervisor, Dr. Kyle O'Keefe for his guidance and mentorship throughout my studies. Your enthusiasm and genuine interest in this project have kept me inspired and determined. Thank you for your salient advice and the opportunities you have provided, you have my deepest gratitude for all your support.

I would also like to thank the Natural Sciences and Engineering Research Council of Canada (NSERC), the Institute of Navigation (ION), and the Geomatics Engineering Department at the University of Calgary for providing financial support throughout my studies. A special thanks to Roslynn Peters with Topcon Positioning Systems for providing software support that made it possible complete this project.

To my colleagues and friends, Matt, Rene, Sandra, Hani, Kent, and to my peers in the PLAN Group, thank you for the brainstorming sessions, collaborations, and support over the past couple years. Thank you for your friendship and for being a part of my journey through graduate school.

I would also like to thank my kayak crew for their willingness to hop onto the rivers at moments notice to assist and run safety so I could collect field data. Thanks always for the many adventures and much laughter.

A special thanks to Donovan, without whom I would not have made it this far. I do not have enough words to truly express my gratitude for all the gym invites and for the hours spent with me to get through the most difficult of times.

Most of all I would like to thank my parents. For their constant love and support and guidance of wherever my feet lead me. The opportunities, encouragement, and freedom you have given me is treasured more than I can express to you.

Table of Contents

Abstract	i
Preface	ii
Acknowledgements	iii
Table of Contents	iv
List of Tables	vi
List of Figures	vii
List of Symbols	x
List of Abbreviations	xiv
Chapter 1 : Introduction	1
1.1 Background	2
1.1.1 GNSS Smartphone Positioning	3
1.1.1.1 GNSS Measurement Errors	4
1.1.1.2 Different Antenna Configurations	5
1.1.1.3 Absolute and Relative Positioning	6
1.1.1.4 GNSS/INS Positioning	7
1.1.1.5 Google Pixel 4 Performance	9
1.1.2 Low-Grade GNSS/INS for Dynamic Applications	10
1.1.3 Inertial Navigation System Positioning	12
1.1.4 Kayaking Biomechanics and Performance	14
1.1.5 Anatomy of Kayak Movement	16
1.2 Objectives and Scope	18
1.3 Outline	20
Chapter 2 : Systems Overview	22
2.1 GPS Measurements	22
2.1.1 GPS Measurements	23
2.1.2 GPS Errors	27
2.1.3 GPS Measurement Quality from Google Pixel 4	28
2.2 Inertial Navigation Systems	31
2.3 Reference Frames	33
2.3.1 Earth-Centered Inertial Frame (<i>i</i> -frame)	33
2.3.2 Earth-Centered Earth-Fixed Frame (<i>e</i> -frame)	34
2.3.3 Local-level Frame (<i>l</i> - or <i>ENU</i> -frame)	34
2.3.4 Body and Device Frame (<i>b</i> - and <i>d</i> -frame)	34
2.4 Frame Rotations	36
2.5 MEMS Sensors	37
2.6 Inertial Sensor Errors	39
2.7 Alignment and Initialization	40
2.8 Low-Cost INS Mechanization	41
2.9 Misalignment	42

Chapter 3 : Estimation Techniques and GPS/INS Integration.....	46
3.1 Least Squares	46
3.2 Kalman filter	49
3.2.1 Innovation Based Quality Control	53
3.3 GPS-only Model	54
3.4 GPS/INS Integration Types	56
3.4.1 Loosely Coupled Integration.....	57
3.4.2 Tightly Coupled Integration.....	58
3.4.3 Loosely Coupled vs Tightly Coupled	59
3.5 Loosely Coupled Model.....	60
3.6 Tightly Coupled Model.....	61
Chapter 4 : Data Collection and Results	64
4.1 Equipment Setup and Data Collection.....	64
4.2 Reference Trajectory Results and Data Selection.....	67
4.3 Software Development	75
4.4 GPS-only Solution	75
4.5 Comparison of Loose and Tight GPS/INS Coupling.....	78
Chapter 5 : GPS/INS Motion Constraints and Results	85
5.1 Motion Constraints	86
5.1.1 Height Constraints	87
5.1.2 Gyroscope Bias Constraints	88
5.1.2.1 Periodic Extended Kalman Filter.....	91
5.1.3 Tilt Angle Offset Constraints	93
5.1.3.1 Pitch Constraint.....	94
5.1.3.2 Roll Constraint.....	95
5.1.4 Accelerometer Bias Constraints.....	96
5.2 Dataset 1 Results.....	97
5.3 Summary of Results.....	108
Chapter 6 : Conclusions and Recommendations	117
6.1 Conclusions.....	118
6.2 Recommendations for Future Work	121
References	123
Appendix A : Raw GNSS and IMU Measurements on Android Smartphones	139
Appendix B : Conversion of Cartesian and Geodetic Coordinates in the <i>e</i> -Frame	143
Appendix C : Results of Datasets 2-4	145
C.1 Dataset 2 Results	145
C.2 Dataset 3 Results	148
C.3 Dataset 4 Results	151

List of Tables

Table 1: Raw GPS measurements.....	29
Table 2: Topcon HiPer SR specifications.....	68
Table 3: Datasets and descriptions.....	72
Table 4: Average standard deviations of reference trajectory for each dataset	74
Table 5: RMSE of GPS-only EKF solution errors.....	77
Table 6: RMSE and standard deviations of GPS/INS LC and TC with complete GPS satellites	79
Table 7: RMSE of GPS/INS LC and TC position of dataset 1	83
Table 8: Summary of GPS/INS navigation errors 20 seconds into GPS outage	114
Table 9: Summary of GPS/INS navigation position RMSE of full datasets with 20 second GPS outage (metres).....	115
Table 10: Summary of GPS/INS navigation azimuth RMSE of full datasets with 20 second GPS outage	116
Table A.1: GPS Clock measurements.....	139
Table A.2: GPS measurements	140
Table A.3: IMU measurements.....	142

List of Figures

Figure 1.1: Anatomy of a kayak	16
Figure 1.2: Kayak pitch, roll, and yaw.....	17
Figure 1.3: Kayak cadence.....	18
Figure 2.1: Carrier phase availability.....	30
Figure 2.2: LS residuals as a function of satellite elevation angle and time.....	31
Figure 2.3: Inertial navigation schematic.....	32
Figure 2.4: i-, e-, and ENU-frames	33
Figure 2.5: Body and device frame.....	35
Figure 2.6: Device and body frames misalignment	43
Figure 2.7: Measured accelerations before and after misalignment correction	45
Figure 3.1: Kalman filter schematic.....	52
Figure 3.2: LC integration schematic.....	57
Figure 3.3: TC integration schematic.....	58
Figure 4.1: Equipment setup	65
Figure 4.2: North Saskatchewan and Kananaskis Rivers	67
Figure 4.3: Reference trajectory fixed and float solutions.....	69
Figure 4.4: Reference trajectory baseline length	69
Figure 4.5: Reference trajectory velocity standard deviations.....	70
Figure 4.6: Reference trajectory position standard deviations.....	70
Figure 4.7: Reference trajectory azimuth.....	71
Figure 4.8: Trajectory of each dataset.....	72
Figure 4.9: Reference solution number of satellites for each dataset	73
Figure 4.10: Reference velocity standard deviations of datasets 1-3.....	73
Figure 4.11: Reference velocity standard deviations of datasets 1-3.....	74
Figure 4.12: Dataset 1 GPS position and velocity errors	76
Figure 4.13: Number of satellites for each dataset	77
Figure 4.14: Dataset 1 LC, TC, and reference azimuth	79
Figure 4.15: Dataset 1 reference trajectory and simulated satellite data outages	80
Figure 4.16: Position and velocity errors of dataset 1 during GPS partial and complete outages	81
Figure 4.17: RMS position and velocity errors during all partial or complete GPS data outages	82

Figure 4.18: Estimated LC and TC standard deviations during all GPS data outages	82
Figure 4.19: Estimated LC and TC standard deviations	84
Figure 5.1: Motion constraint schematic	87
Figure 5.2: Drifting and non-drifting angles calculated from gyroscope measurement integration	89
Figure 5.3: Cycle selection	91
Figure 5.4: Observed roll and estimated roll from periodic EKF	93
Figure 5.5: Offset and non-offset roll calculated from gyroscope measurement integration	94
Figure 5.6: Tilt angles of dataset 1 with and without motion constraints	98
Figure 5.7: Gyroscope bias of dataset 1 with and without motion constraints	99
Figure 5.8: Velocity of dataset 1 with and without motion constraints in the body frame	100
Figure 5.9: Accelerometer bias of dataset 1 with and without motion constraints	102
Figure 5.10: Velocity errors of dataset 1 during a GPS outage with and without motion constraints	103
Figure 5.11: Position errors of dataset 1 during a GPS outage with and without motion constraints	104
Figure 5.12: Trajectory of dataset 1 and reference solution with and without motion constraints	105
Figure 5.13: Azimuth of dataset 1 and reference trajectory with and without motion constraints	106
Figure 5.14: Estimated standard deviations of horizontal and vertical positions of dataset 1 during a GPS outage with and without motion constraints	107
Figure 5.15: Horizontal and vertical position errors of dataset 1 during a GPS outage with and without motion constraints	108
Figure 5.16: Attitude of dataset 2 with and without motion constraints	109
Figure 5.17: Horizontal and vertical position errors of dataset 2 during a GPS outage with and without motion constraints	110
Figure 5.18: Attitude of dataset 3 with and without motion constraints	111
Figure 5.19: Horizontal and vertical position errors of dataset 3 during a GPS outage with and without motion constraints	112
Figure 5.20: Attitude of dataset 4 with and without motion constraints	113

Figure 5.21: Horizontal and vertical position errors of dataset 4 during a GPS outage with and without motion constraints..... 114

List of Symbols

Symbol	Definition
A_0	DC Offset
A_1	Magnitude of the fundamental harmonic waveform
b_a	Accelerometer sensor biases
b_g	Gyroscope sensor biases
c	Speed of light
$C_{\hat{x}}$	Covariance of observation errors
C_v	Innovation sequence covariance
d	Number of degrees of freedom
D	Transformation matrix to transform velocity rectangular coordinates into curvilinear coordinates in the e -frame
$dopplershift$	Dopplershift derived from the raw GPS measurements
D_f	Diagonal matrices of the time rate of change of the accelerometer errors
D^n	Doppler shift of the n th satellite
D_ω	Diagonal matrices of the time rate of change of the gyroscope errors
e	Earth's eccentricity
ECEF	Earth-Centered Earth-Fixed
ECI	Earth-Centered Inertial
ENU	East-North-Up
f^b	Measured specific force in the body frame (f_x^b, f_y^b, f_z^b)
\tilde{f}^b	True specific force in the body frame (f_x^b, f_y^b, f_z^b)
F_r	Skew-symmetric matrix of the position errors
F_v	Skew-symmetric matrix of the velocity errors
F_ε	Skew-symmetric matrix of the attitude errors
g^l	Earth's gravity field in the local level frame
G	Process noise shaping matrix
h_k	Function relating the unknown states to the measurements
H	Jacobian (design) matrix of the measurements with respect to the unknown states
J	Least squares function to be minimized
n	Number of satellites observed at k th epoch
N	Carrier phase integer ambiguity

N_a	Non-orthogonality of the accelerometer triad
N_g	Non-orthogonality of the gyroscope triad
p	Pitch angle
P	Prediction and estimated error covariance of state vectors
P_p	Pseudorange measurement
\dot{P}_p	Pseudorange-rate measurement
q_c	Power spectral density of an estimated state vector
Q	Spectral density of system noise
r	Roll angle
R	Measurement noise covariances
R_j^k	Transformation matrix from coordinate frame j to coordinate frame k
R_N	Earth's prime vertical radius of curvature
\dot{R}_b^l	Rate of change of rotation in the l -frame
S_a	Accelerometer scale factor
S_g	Gyroscope scale factor
t	Time
t_{Rx}	Received measurement time
t_{Tx}	Transmitted measurement time
T	Transformation matrix from local level to Earth-centered Earth-fixed frame
w	Measurement noise
W	Least squares weighting function
x	State vector of unknown parameters
x^R, y^R, z^R	Receiver position ECEF coordinates
x^S, y^S, z^S	Satellite position ECEF coordinates
v	Innovation vector
v_{noise}	Measurement noise vector
v_e, v_n, v_u	Velocity in the east, north, and up respectively
z	Measurement or innovation vector
δb_r	Receiver clock offset
$\dot{\delta b}_r$	Receiver clock drift
δb_s	Satellite clock offset
$\dot{\delta b}_s$	Satellite clock drift

δd_{ion}	Ionosphere error
$\delta \dot{d}_{ion}$	Ionosphere drift
δd_{trop}	Troposphere error
$\delta \dot{d}_{trop}$	Troposphere drift
δd_{orb}	Orbital error
$\delta \dot{d}_{orb}$	Orbital drift
$\delta \varepsilon^l$	Attitude error vector (p, r, ψ_y)
δr^e	Position error vector in the Earth-centered Earth-fixed frame (r_x, r_y, r_z)
δr^l	Position error vector in the local geodetic WGS-84 frame containing Latitude ($\delta\varphi$), Longitude ($\delta\lambda$), and Height (h)
$\delta \dot{r}^l$	Rate of change of position in the l -frame
δv^e	Velocity error vector in the Earth-centered Earth-fixed frame (r_x, r_y, r_z)
δv^l	Velocity error vector in the local level frame ($\delta v_e, \delta v_n, \delta v_u$)
$\delta \dot{v}^l$	Rate of change of velocity l -frame
Δt	Prediction time interval
$\varepsilon_{carrier}$	Measurement noise and error
ε_{code}	Pseudorange measurement error including multipath and noise
$\dot{\varepsilon}_{code}$	Code multipath and noise drift
ε_f	Sensor noise of the accelerometer
ε_ω	Sensor noise of the gyroscope
ρ	True geometric range between the satellite and receiver
$\dot{\rho}$	True pseudorange rate between the satellite and the receiver
ξ	Misalignment angle
σ	Standard deviation
φ, λ, h	Geodetic Latitude, Longitude, and Height
ϕ	Rotation angle offset of the fundamental waveform
Φ	State transition matrix
Φ_λ	Measured carrier phase
λ	Carrier wavelength
ψ_A	Azimuth angle (measured clockwise)
ψ_y	Yaw angle (measured counterclockwise)
ω_e	Earth's rotation rate

ω^b	Measured angular rate in the body frame ($\omega_x^b, \omega_y^b, \omega_z^b$)
$\tilde{\omega}^b$	True angular rate in the body frame ($\omega_x^b, \omega_y^b, \omega_z^b$)
ω_r	Rotation velocity of waveform
Ω_{ie}^l	Skew-symmetric matrix of the rotation rate (ω_{ie}^e)
Ω_{el}^l	Skew-symmetric matrix of the Earth's rotation rate (ω_{el}^l)
Ω_{ib}^b	Skew-symmetric matrix of the rotation rate (ω_{ib}^b)
Ω_{il}^l	Skew-symmetric matrix of the rotation rate (ω_{il}^l)
Ω_{ε^l}	Skew-symmetric matrix of the attitude errors ($\varepsilon_p, \varepsilon_r, \varepsilon_{\psi_y}$)

List of Abbreviations

Abbreviation	Definition
3D	Three-Dimensional
API	Application Programming Interface
C/A	Coarse Acquisition
C/No	Carrier-to-Noise-density ratio
ECEF	Earth-Centered Earth-Fixed
ECI	Earth-Centered Inertial
EKF	Extended Kalman Filter
ENU	East-North-Up
GNSS	Global Navigation Satellite Systems
GPS	Global Positioning System
IMU	Inertial Measurement Unit
INS	Inertial Navigation System
KF	Kalman Filter
LC	Loosely Coupled
LS	Least Squares
MEMS	Micro-ElectroMechanical System
NMEA	National Marine Electronics Association
NHC	Non-Holonomic Constraint
PPP	Precise Point Positioning
PRN	PseudoRandom Noise
PVT	Position, Velocity, and Time
RMSE	Root Mean Square Error
RTK	Real-Time Kinematic
TC	Tightly Coupled
ZARU	Zero Angular Rate Update
ZVU	Zero Velocity Update
ZUPT	Zero Velocity UPdate

Chapter 1: Introduction

In the next 10 years, the number of Global Navigation Satellite System (GNSS) devices in use globally is forecast to be over 10 billion, 86% of which are estimated to be for consumer solutions by 2031 (EU Agency for the Space Programme, 2022). Smartphone and wearable devices are expected to contribute to 92% of annual shipments of GNSS receivers. Handheld devices such as Android smartphones are rapidly becoming the prevailing base for navigation and tracking in consumer applications, particularly with the recent release of Android 7 (Nougat) in 2016. This release has made it possible for developers to create, implement, and test raw GNSS measurement level navigation algorithms and techniques using an Android device, whereas previously these methods could only be implemented on dedicated hardware.

Despite these advances, the applicability of Global Positioning System (GPS) navigation in some environments and applications can still be insufficient due to satellite signal outages. The integration of inertial navigation systems (INS) with GPS measurements can be used to overcome this limitation and provide a continuous solution when intermittent gaps in the GPS solution occur. Expensive, high-grade INS can be used to achieve high accuracy position in the occurrence of GPS signal outages; however, smartphones contain low-cost micro-electromechanical system (MEMS) sensors, and it would not be feasible to fit a high-grade INS in a consumer level device. Many modern smartphone devices today are equipped with inertial sensors including gyroscopes and accelerometers.

In this thesis, the focus is to track a kayak accurately and continuously through a river using a low-cost, strapdown smartphone GPS/INS based positioning system. GPS signal outages may frequently occur due to water splashing over the smartphone sensors, or tall canyons along the river causing the navigation solution to be reliant on INS only. However, low-cost INS, such as those found in a smartphone, are incapable of providing accurate positions over long periods of time because of the accumulation of errors that occur over short time intervals (X. Niu et al., 2007). Multiple methods and studies have been proposed to mitigate these errors. In vehicle navigation, non-holonomic constraints can be applied in which the perpendicular direction of travel and up direction of the vehicle's velocities are assumed to be zero (Dissanayake et al., 2001). In strapdown pedestrian navigation, methods like zero updates and dead reckoning can be used with every step

when the foot is stationary (Z. Wang et al., 2015). Dead reckoning and non-holonomic constraints can also be adapted and used for other applications like cycling for example (Chang et al., 2015). The kinematics of a kayak provides a unique scenario to propose, test, and evaluate a low-grade smartphone navigation system. The distinct difference between kayaking and pedestrian or vehicular navigation is that the kayak is never stationary, and it is always moving in all directions; therefore, non-holonomic or zero updates are not feasible. This thesis analyzes the motion of a kayak and proposes GPS/INS motion constraints exclusive to kayaking to improve the solution for continuous, reliable tracking of a kayak, particularly during a GPS outage.

This chapter provides an overview of the background and related previous work pertaining to this research. Then the objectives and scope of this project are presented, followed by an outline of this thesis.

1.1 Background

The challenge of accurately tracking a river kayak through its environment requires an understanding of the following: smartphone positioning and performance, low grade GPS/INS integration, INS positioning, and kayaking kinematics and dynamics. This section provides an overview of existing research works completed discussing these elements.

Section 1.1.1 provides an overview of current studies to date that have been completed regarding Android device positioning. The increase in availability of smartphones coupled with recent feasibility of accurate smartphone positioning from raw GNSS measurements has triggered a heightened interest in research in the field of Android positioning.

The dynamic nature and environment of river kayaking challenges the capabilities of GPS navigation and in some cases, may create GPS outages for a period of time. In these instances, an INS can be utilized to provide a continuous solution. There have been many projects to date that have applied low-grade GNSS/INS (similar to that in a smartphone) for kinematic applications similar to kayaking; these are discussed in section 1.1.2.

Section 1.1.3 reviews publications that have used an INS solution and various methods to correct or calibrate errors in an INS. In the event of a GPS outage, a low-grade INS will degrade rapidly

due to the accumulation of errors over time. Prior solutions to compensate for inertial measurement unit (IMU) sensor errors include applying zero updates or motion constraints to aid the inertial sensor measurements.

Some of these INS error mitigation techniques utilize the motion of the application to correct drifting errors. These motion constraints are constructed based upon the assumptions of movement in an application. For example, an inertial sensor strapped to a pedestrian's foot will observe walking gait and it can be assumed that the foot will have zero motion during the foot-flat part of each step. Therefore, an understanding of a kayak's kinematics through water is essential to apply constraints to the navigation solution to mitigate sensor errors. Section 1.1.4 presents several publications discussing watercraft movement and section 1.1.5 describes the dynamic motion specifically of a kayak travelling through a river.

1.1.1 GNSS Smartphone Positioning

In 2016, Google released application programming interface (API) 24 on Android smartphones which allowed users to access raw GNSS measurements (European GNSS Supervisory Authority., 2017). An API is used to connect Android applications with mobile sensors integrated in the phone. This release led to more development and research on GNSS processing techniques that, until recently, had only been possible on GNSS-specific hardware.

Prior to this release, API 23 (Android 6 Marshmallow) had limited access to GNSS data which mainly included satellite information such as carrier-to-noise-density ratio (C/No), azimuth, elevation, National Marine Electronics Association (NMEA) sentences, and position, velocity, and time (PVT) time-stamped solutions. GNSS configurations and algorithms were not accessible to users and was contained to the pre-programmed chipset itself. The release of API 24 has enabled developers to access more GNSS information in addition to the satellite information which was only accessible prior to this API.

Currently, there are several manufacturers producing smartphones that can access raw GNSS measurements: including Google, Huawei, Samsung, Xiaomi, and Honor. A list can be found at the website *Dual-Frequency GNSS on Android* (n.d.). Some models of phones are fitted with a GNSS chipset that can record measurements from one satellite constellation, one frequency, and

are unable to record carrier phase measurements. Other GNSS chipsets may support multi-constellation, dual-frequency, and carrier phase measurement positioning, this varies across phone models.

Android 7 Nougat (API 24) made it possible for developers to create, implement, and test raw-measurement-level navigation algorithms and techniques gathered with a smartphone, compared to the past where these methods could only be studied using dedicated hardware. In recent years, there have been many publications related to GNSS smartphone positioning for a range of applications from pedestrian to vehicular navigation, and GNSS-denied and centimetre level positioning with Android devices.

This sub-section provides an overview of recent publications using Android device positioning. This includes research with Android devices regarding the quality of code and carrier phase measurements, external antenna configurations, GNSS errors, precise point positioning (PPP), real-time kinematic positioning (RTK), and GNSS/INS. Next, a review is provided about of the quality of measurements and positioning performance of the specific smartphone used in this project (Google Pixel 4). In addition to this section, an excellent literature review of GNSS smartphone positioning research completed up to 2021 can be found in Zangenehnejad & Gao (2021).

1.1.1.1 GNSS Measurement Errors

The quality of observations and subsequent positioning performance is heavily influenced by several GNSS measurement errors.

In Massarweh et al. (2020), the effect of multipath was investigated in a Xiaomi Mi 8 smartphone by exploiting the dual-frequency capabilities using code-minus-phase and multipath-linear-combination techniques. Multipath was found to be more prevalent in locations with higher elevations and multi-frequency GNSS improves the positioning solution as compared to a single-frequency GPS solution. Humphreys et al. (2016) used a customized Android Marshmallow API to access and process the raw code and carrier observations from a Samsung Galaxy S5 smartphone to assess if a smartphone could yield a centimeter-accurate solution. The analysis concluded that

multipath effects was the main challenge to achieving centimeter level positioning from a smartphone.

In Wang et al. (2020), an ionosphere-constrained single frequency PPP model was used and compared to traditional algorithms using two smartphones. This model was utilized to circumvent the poor measurement quality and loss of lock that occurs in code and carrier phase measurements. The results show that the ionosphere-constrained model improved the positioning accuracy as compared to a non-ionosphere-constrained model.

The viability of carrier-phase resolution on Android smartphones was investigated in Geng & Li (2019). This study tested several Android devices and concluded that fluctuations present in the phase observations which prevent centimeter-accurate positioning are caused by initial phase biases in the chipset. By calibrating the initial phase biases, Geng & Li (2019) found that centimeter-accurate positioning is achievable through double differencing with an external antenna attached to the Android device.

1.1.1.2 Different Antenna Configurations

Low-quality antennas lead to receiver measurement errors such as multipath and receiver noise, frequent cycle slips, and missing phase observations (G. Li & Geng, 2019; Zangenehnejad & Gao, 2021). These qualities limit the capabilities of high-performance positioning in Android devices. Therefore, many studies use an external antenna in lieu of the embedded device antenna to provide the opportunity to isolate and investigate the performance of GNSS measurements, ambiguity resolution, and solution accuracy.

Siddakatte et al. (2017) investigated the performance of a Huawei Mate9 Android smartphone using different antenna configurations in an urban canyon. The use of an external antenna in this study improved the quality of the carrier-to-noise-ratio, code measurements, and corresponding positional data. The cause of these measurement error characteristics from the embedded antennas was explored in Li & Geng (2019). They concluded that the omnidirectional passive linear polarized internal antenna in a smartphone contributes to the error characteristics in these measurements. The carrier phase was also investigated in this study using a Samsung Galaxy S8 and Huawei Honor v8; it was concluded that the phase measurements were discontinuous due to

duty-cycling. An Android update released in 2018 rectified the duty-cycling discontinuity problem and allowed users to disable the duty-cycling in the device to access continuous carrier phase observations.

Wanninger & HeBelbarth (2020) performed an antenna calibration to find the phase center on a Huawei P30 using the available frequencies of L1, L5, G1, E1, E5a, B1-2, and L5. It was determined that not all carrier phase observations have the integer ambiguity property, only L1 frequencies have the capabilities for ambiguity fixing. Using only the L1 frequency, they fixed the carrier phase ambiguities and found the phase center to be located at the top of the device. The results presented indicated that the three-dimensional (3D) position errors of 2 centimeters can be obtained after 5 minutes of static observations after the ambiguities are fixed. Wen et al. (2020) replaced the embedded Xiaomi Mi 8's antenna with an external survey-grade antenna and investigated PPP ambiguity resolution. They demonstrated the feasibility of centimeter-level accuracy with this method, along with the possibility to fix undifferenced ambiguities with dual-frequency from Android GNSS data.

1.1.1.3 Absolute and Relative Positioning

PPP is becoming a predominate navigation solution due to its ease of use and availability of precise satellite orbit and clock corrections available from GNSS service stations (Lachapelle & Gratton, 2019). With the availability of dual-frequency Android devices, carrier phase integer ambiguity can be solved allowing for PPP and RTK to be applied to mitigate GNSS errors and improve the navigation solution.

Fortunato et al. (2019) analyzed the performance of PPP and RTK of a dual-frequency Xiaomi Mi 8 smartphone for sub-meter positioning. Wu et al. (2019) and Elmexayen & El-Rabbany (2019) investigated dual-frequency GNSS PPP on a Xiaomi Mi 8 in both static and kinematic modes. The static experiments resulted in sub-decimeter accuracy with long time convergence, while the kinematic experiments resulted in meter-level accuracy due to difficulty obtaining continuous results.

The characteristics of code and carrier-phase measurements from a Huawei Honor 9, Huawei P10, and Xiaomi Mi8 were analyzed in Chen et al. (2019). It was concluded that the difference between

these measurements is not fixed and a single frequency PPP solution which estimated the clock biases separately was proposed to correct this issue. It was noted that utilizing dual frequency can eliminate ionospheric delay error and improve the positioning performance.

Additional works on GNSS PPP with Android devices include Aggrey et al (2020), Lachepelle & Gratton (2019), and Robustelli et al (2020). These studies proved the possibility of decimeter- and meter-level positioning accuracy for both static and kinematic scenarios utilizing dual-frequency. H. Zhu et al. (2020) developed a multi-GNSS PPP stochastic model that is based on carrier-to-noise ratio observations. The proposed model was testing on a Huawei Mate 30 and improved horizontal and vertical errors.

In addition to absolute positioning PPP, relative positioning techniques including differential GPS and RTK have been studied on Android devices. In Bakula et al. (2022), a comparison of L1 and L5 code measurements using differential GPS positioning was presented using Huawei P30 Pro smartphones. It was concluded that the positioning errors for L5 code observations were smaller than those from L1 observations.

Niu et al. (2019) combined RTK with an IMU pedestrian navigation algorithm to overcome GNSS challenges in urban environments. Their experiment utilized a Xiaomi Mi 8 smartphone and proved the feasibility of robust positioning in challenging environments. A single-baseline RTK experiment with multi-frequency and multi-constellation was conducted in Dabove & Di Pietra (2019). They demonstrated that it was not possible to fix phase ambiguities and achieve real-time centimeter-level accuracy. The GPS-only and GPS+Galileo float solutions obtained better precision results than those obtained with the GLONASS constellation added as well. Finally, Zhang et al. (2019) proposed an approach called Smart-RTK where an optimized kinematic approach is used with a Doppler-smoothed-code and constant acceleration model. These were implemented in lieu of using carrier measurements, which are prone to cycle slips, to reduce code measurement noise

1.1.1.4 GNSS/INS Positioning

Modern Android devices are embedded with GNSS and IMU sensors such as gyroscopes, accelerometers, and magnetometers. Combining these sensors into a GNSS/INS solution provides

the capability of a position, velocity, and attitude solution. Several methods and applications have been completed using Android GNSS/INS as presented below.

A smartphone vehicular navigation system was developed in Grochowski et al. (2018) where a closed-loop GPS/INS loosely coupled filter was implemented using a Samsung Galaxy S4. The quality of the navigation solution was highly dependent on the quality of the measurements from the inertial sensors and these sensor errors will limit the systems performance. However, the study stated that the GPS solution was extracted from the Android API and did not provide a thorough analysis on the quality of both the GPS and GPS/INS solution. Similarly, Sheta et al. (2018) investigated the performance of an INS-only and GPS/INS loosely coupled solution from a Huawei Mate 8 device strapped to the dash of a vehicle. This research illustrated a significant drift in the GPS/INS solution during a 10 second GPS outage. The results of the previous two studies also concluded that a GPS/INS solution is better than an INS-only solution.

Yan et al. (2019) assessed the quality of raw IMU measurements from a Xiaomi 8 and Honor Play smartphone by comparing them to higher grade IMUs. The IMUs in the Android devices were determined to have good performance in determining the position, velocity, and attitude angles. A further study was then conducted by Yan et al. (2020) in which it was determined that the accelerometer and gyroscopes have different sampling rates. A modified Kalman filter (KF) was proposed to integrate the different rate sensors in a GNSS/IMU system, and it resulted in a significant solution improvement of the position and attitude accuracy during a simulated GNSS outage.

K. Xu et al. (2021) investigated the application of non-holonomic constraints in vehicle navigation with a smartphone. The experiments in this study were conducted using both a simulated and real tunnel to evaluate the performance of the system and concluded a feasible accuracy can be achieved through a tunnel. However, the study did not specify the type of smartphone used, the GNSS constellations used, nor the quality of the GNSS solution.

Studies have also been conducted evaluating GNSS/INS integration for Android devices utilizing different systems such as ultra-tightly coupled or incorporating additional sensors such as cameras. Luo et al. (2019) developed an ultra-tightly coupled GNSS/INS system and tested it with vehicle navigation on a Huawei Mate 9 which resulted in a better solution than a loosely coupled system.

Chiang et al. (2020) also created vehicle navigation system by integrating GNSS/INS with visual simultaneous location and mapping from an Android smartphone.

Centimeter level positioning was targeted in Bochkati et al. (2020) with a Xiaomi Mi 8. The smartphone IMU was found to be more reliable and steadier as compared to a commercial MEMS IMU and was investigated using an Allen variance analysis. A RTK GNSS/IMU solution with carrier-phase ambiguity fixing was also proposed which resulted in a meter level solution as only a float solution could be found. This research also concluded that a choke-ring platform attached to the smartphone improved the positioning accuracy significantly because of multipath mitigation. Finally, Rehman et al. (2020) created a GNSS/pedestrian dead reckoning system for an Android device to test the feasibility of high-level positioning with low-grade hardware. They proved the possibility of using smartphone pedestrian dead reckoning in a GNSS-denied environment with a sub-meter positioning error in GNSS challenged areas.

1.1.1.5 Google Pixel 4 Performance

The Google Pixel 4 smartphone is the Android device that is used in this project. This smartphone contains a Qualcomm chipset which enables the use of dual-frequency (L1 + L5, E1 + E5a) and multi-constellation positioning (Zangenehnejad & Gao, 2021). A small number of studies have been conducted with this phone assessing the quality of its observations and capabilities of positioning performance.

Zangenehnejad & Gao (2021) analyzed a 30-minute dataset that was collected for a competition named Google Smartphone Decimeter Challenge (Fu et al., 2020) using a Google Pixel 4, Google Pixel 5, Xiaomi Mi 8, and a Samsung S20 Ultra. The dataset was collected with duty-cycle disabled to allow for continuous carrier phase observations and Zangenehnejad & Gao (2021) used measurements from GPS, GLONASS, Galileo constellations with the L1-frequency only. The results indicated that of the four Android devices used, the Pixel smartphones had the best carrier-to-noise density performance with better uniformity. However, the phase observation continuity and availability from the Pixel phones were inconsistent with continuity ranging from 1.45%-94.02% availability for GPS satellites while code observations were still observable. The counterpart phones, Xiaomi Mi 8 and Samsung S20 Ultra, produced 100% phase continuity.

GLONASS and Galileo constellations generated similar results to those from GPS in terms of phase continuity.

A single-baseline RTK solution was assessed in Yong et al. (2021) using dual-frequency and phase observations with Samsung Galaxy S20 and Google Pixel 4 devices. The effect the orientation of the smartphone has on positioning performance was evaluated and concluded that smartphones lying down will deteriorate the solution as opposed to an upright smartphone. In the upright position, centimeter-level results from the Google pixel 4 were achieved using short-baseline RTK with a static receiver.

Most recently, Bahadur (2022) evaluated the performance of code based, single-frequency observations from a Xiaomi Mi 8, Google Pixel 4, and Google Pixel 4XL in a vehicular kinematic environment. They used ultra-rapid and IGS real-time service products for real-time processing with a variance component method applied to estimate multi-GNSS observation weights. This study concluded that the integration of multiple constellations (GPS, GLONASS, Galileo, BeiDou) improved the position accuracy by an average of 23.6% and IGS real-time service produced a better solution than ultra-rapid products.

These existing studies completed with Android devices focus mainly on the quality of observations, standalone positioning, and relative positioning. Most of these experiments have been conducted in ideal environments such as open-sky and utilized external hardware or correction services to improve the solution. There has been a limited amount work completed in standalone GNSS/INS kinematic positioning in a challenging environment using the embedded Android device sensors. Considering this gap in Android-specific positioning studies, publications utilizing low-grade GNSS and IMU sensors for kinematic applications are reviewed in the following section to provide further clarification of GNSS/INS integration techniques used for dynamic applications like kayaking.

1.1.2 Low-Grade GNSS/INS for Dynamic Applications

Low cost GNSS/INS have become increasingly popular in dynamic applications due to the technological improvements of MEMS sensors, making them smaller, light weight, low cost, and low power usage (X. Niu et al., 2007). Accelerometers, magnetometers, and gyroscopes can be

combined into an INS to overcome the GPSs signal lack of continuity (Falco et al., 2012). There have been many studies investigating the integration of MEMS with GPS to track dynamic applications such as downhill skiing, ski jumping, mountain biking, and rowing

Tan et al. (2008) integrated GPS and IMU data with a Kalman filter based complementary filter to determine a runners stride average speed and variation. Another study integrated GPS and an IMU consisting of an accelerometer and gyroscope with high sampling rates to measure sprinting velocity (Mertens et al., 2018). Integrating the IMU measurements with GPS proved to be a more stable and accurate system to measure sprinting performance parameters when GPS errors occurred.

Brodie et al. (2008) combined GPS and IMU data with video and theodolite measurements to capture the 3D kinematics of alpine ski racing. In Waegli & Skaloud (2009), GPS with MEMS-IMUs was integrated using both a loosely and tightly coupled (TC) approach for downhill skiing. Both approaches performed similarly with complete satellite constellations, however, the tightly coupled approach outperformed the loosely coupled (LC) method in instances without a completed satellite constellation.

H. Xu et al. (2010) reviewed the capabilities of integrating the position data of two MEMS gyroscopes and two GPS receivers in an extended Kalman filter (EKF) for wheelchair sports. The velocity and position measurement system introduced improved the position update rate while maintaining position accuracy.

Most similar to kayaking, Hermsen (2013) estimated the position, speed and stroke rate of a rower with a consumer grade accelerometer and GPS fused with a linear Kalman filter. Cloud et al. (2019) mounted an iPhone 7 smartphone to the deck of a boat to collect GPS and accelerometer data for estimating rowing kinematics. To compute measurements of boat speed and distance travelled, a complementary filter and Kalman filter were implemented and compared; both filters proved to improve the accuracy and precision of the metrics when compared to GPS only smartphone data.

The studies presented in this section proved the feasibility of using low grade GPS and IMU sensors for dynamic applications. However, the positioning accuracy of these solutions in the event of a GPS outage will degrade rapidly because of high sensor errors and noise in low grade IMUs.

Several researchers have investigated and implemented various methods to mitigate these errors and improve the INS solution, these methods are presented in the next section.

1.1.3 Inertial Navigation System Positioning

Major challenges occur in the inertial solution in GPS-denied environments because of the quality of inertial sensors.

In a low grade system, accelerometer and gyroscope measurements are subject to significant errors in both bias and drift which degrade the estimation accuracy of the navigation solution over time (Y. Li et al., 2012). The angular rates measured from a gyroscope are integrated using the rigid body motion model of rotation to estimate the orientation of the IMU (Noureldin et al., 2013). INS rely on this knowledge of the IMUs alignment to determine the orientation of the accelerometer and remove the Earth's gravity from the specific force measurements. MEMS sensors, such as those used in smartphones, can exhibit high error sources over short time intervals. These errors may present themselves as a bias which degrades the accuracy of the sensor, limiting the possibility of using MEMS sensors for high-accuracy applications. A bias in the gyroscope will introduce a second order error in velocity and a third order error in position (Skog & Handel, 2009). An uncompensated accelerometer bias will introduce a first and second order error in velocity and position respectively. A gyroscope with no bias will output a value of zero when no input is applied, and an ideal accelerometer will only output the Earth's gravity with no other motion present. Any deviation from these values for stationary sensors indicates an error in the sensor. Therefore, MEMS sensors are accurate for a short amount of time without additional aiding sensors or proper calibration. These errors can be mitigated or eliminated using calibration procedures, additional sensors, or motion constraints.

The sensor bias can be split into a deterministic and a stochastic part which are referred to as bias offset and bias drift respectively (Aggarwal et al., 2010, p.35-61). A bias offset is a constant error that is exhibited by inertial sensors and can be determined by calibration. Bias drift is the rate in which error accumulates with time; this error is random in nature and can be modelled as a stochastic process. The deterministic part of the gyroscope bias can be removed by calibration techniques such as carouseling (Renkoski, 2008) and angle rate tests; whereas the accelerometer

bias can be removed using a six-position static test (Titterton & Weston, 2004). Further methods for calibrating the MEMs IMUs using both field and laboratory techniques can be found in Fong et al. (2008), Y. Li et al. (2012), and Nieminen et al. (2010). While laboratory calibration procedures can be used to mitigate sensor errors, it is not feasible to perform a calibration procedure prior to each use for a consumer application. Furthermore, stochastic biases will vary with time and environmental conditions on a run-to-run basis and must be mitigated for each run.

One approach to reduce these sensors errors is to integrate additional sources of measurements. Inertial systems can be augmented with external sensors such as GPS (Leung et al., 2011), magnetometers (Mansoor et al., 2019), ultra-wideband (Z. Li et al., 2018), vision technology (W. Wang & Wang, 2008), and more to improve the navigation solution. However, additional sensors make the system more complex and expensive and may not be readily available for a consumer grade device and application. These additional sensors can be integrated with IMUs using non-linear estimation techniques to improve bias estimation and observability. For instance, Grip et al. (2015) uses GPS observations to estimate the gyroscope bias and provide a position reference. Heading of an inertial solution can be corrected from magnetometers (Mansoor et al., 2019) or GPS measurements, but this technique may not be wholly reliable due to the unpredictable nature of the Earth's geomagnetic field (Fan et al., 2018) or when GPS signals are unavailable. Accelerometers and gyroscopes can be used in conjunction in a self-calibrating system. The orientation tilt angles (pitch and roll) from a gyroscope can be corrected by the accelerometers; the dynamic motion of the system will still affect the linear accelerations measured by the accelerometer and the corresponding gravity vector making this method complex for kinematic applications. Therefore, in the absence of additional sensors, an important problem arises on how to acquire a reliable navigation solution from an IMU that contains only an accelerometer and gyroscope.

The use of motion constraints pertaining to the host vehicle/body application are a viable option to improve an INS solution. There have been several different techniques that have been previously used in different applications. These include zero updates, non-holonomic constraints, and dead reckoning techniques. Zero updates rely on periods of time that the system is stationary and can be used to update measurements in the gyroscope or accelerometer or velocity states. Zero velocity updates (ZVU or ZUPT) are applied when the host vehicle is stationary, most commonly found in

vehicle or pedestrian navigation applications (Foxlin, 2005; Grejner-Brzezinska et al., 2001; Z. Wang et al., 2015). A zero angular rate update (ZARU) is used to estimate the gyroscope bias (Rajagopal, 2008). Non-holonomic constraints (NHCs) can be applied by utilizing information about the host vehicle/body motion. In vehicular navigation, it can be assumed that the vehicle travels in a forward direction and velocity along the perpendicular and up axis are assumed zero (Dissanayake et al., 2001; X. Niu et al., 2007). The limitations of zero updates and non-holonomic constraints is that the host vehicle must have stationary periods, or that the velocity in a direction can be assumed zero.

Dead reckoning is another technique that is most often used for pedestrian applications and exploits the kinematics of a human walking (Chang et al., 2015; Rehman et al., 2020; F. Zhu et al., 2019). Strapdown inertial navigation estimates position, velocity, and attitude from integration over time whereas dead reckoning uses steps to estimate relative position and heading displacement. Dead reckoning is mainly composed of three components including heading determination, step or cycle detection, and step or cycle distance determination. The integration of GPS and dead reckoning often complement each other to provide continuous position in GPS-denied environments similar to a GPS/INS solution (F. Zhu et al., 2019). Similar to strapdown inertial navigation, errors in dead reckoning accumulate and grow with time because of sensor errors.

In this thesis, strapdown inertial navigation is used to estimate the trajectory of a kayak. Motion constraints applicable for kayaking must be used to prevent the low-grade inertial solution from drifting during a GPS outage. The next two sections describe studies pertaining to the motion of the kayak and an analysis of a kayak's movement is presented to understand a kayak's kinematics for motion constraints.

1.1.4 Kayaking Biomechanics and Performance

Multiple approaches to data recording and evaluation have been used in different experiments which have led to a clearer understanding of the biomechanics of kayaking. Primary areas of biomechanical research pertaining to kayaking mainly focus on rate strategy, kinematics, dynamics, and training exercises, and have been conducted with kayak ergometers and on-water

tests (M. Li, 2017). The majority of these studies have been focused on the analysis of a paddler's motion, and the measurement of the forces acting upon the paddle and kayak. Kinematic parameters such as speed, distance, stroke rate, and stroke force have been analyzed using video filming, INS, and GPS devices along with computational algorithms and software analysis. These parameters and methods of evaluation have helped athletes and coaches improve on paddling technique.

Kinematic studies have been conducted for flat water conditions to analyze power, stroke rate, impulse, and other parameters. Movement for upper body (Fleming et al., 2012), lower limbs (Nilsson & Rosdahl, 2016), and joint (whole body) (Bjerkefors et al., 2018) has been captured on a kayak ergometer to analyze range of motion, rotation, and kinematics of the body during paddling. Inertial sensors like accelerometers and gyroscopes have been used to capture kayak motion. In Janssen & Sachlikidis (2010), an accelerometer was mounted to the kayak to assess velocity and acceleration. In Vadai, Gingl, et al. (2013) and Vadai, Makan, et al., (2013), a 3-axis accelerometer and gyroscope micro-controller was mounted under the kayak seat to measure inertial fluctuations to find paddle stroke rate and impulse. Croft and Ribeiro mounted a tri-axial accelerometer to a paddle to measure the cadence of kayak strokes per minute to inform athletes if they are performing within the optimal efficiency (Croft & Ribeiro, 2013). Other biomechanical studies include an in-board accelerometer to measure boat dynamics (Robinson, 2011), or using force transducers in Aitken & Neal (1992) to quantify on-water forces and paddler power. Nakashima et al. (2017) developed a comprehensive simulation model of the paddler, paddle and hull using cameras in a water tank to capture the paddling motion. The relationship between the paddling motion and the hull behaviour of a kayak was then investigated to connect paddling motion with propulsive efficiency.

While there are many studies on the biomechanics of a kayaker, there has been very little research done on the effects of boat motion itself on its speed or velocity. The most similar publication to kayak motion on water was conducted by Loschner et al. (2000) with rowing sculls. In this work, gyroscopes were used to measure the 3D angular velocity of the boat axes and found that changes in yaw and roll created by the rower negatively influenced the boat propulsion efficiency more than the pitch. In K1 kayaking, high speed cameras were used to determine how the path chosen by athletes influenced the time taken to travel through a gate point on a race course (Hunter, 2009).

Halvorsen & Olsson (2016) proposed a method of estimation under the assumption that the body returns to the same position and orientation at regular time intervals; the movement is cyclic. This paper modelled the cyclic motion of a kayak paddle with the amplitude and phase of sinusoidal waves. Then a nonlinear weighted least squares (LS) estimation was implemented to find the maximum likelihood solution. This method successfully generated the cyclic movement of a kayak paddle from sensor data and used the assumption of periodicity to eliminate the drift.

1.1.5 Anatomy of Kayak Movement

Kayaking is a sport in which a small boat is manually propelled through water. The paddler sits in the hull of the boat and uses a double-bladed paddle to transfer force from the paddler to the water to move forward. Figure 1.1 shows the parts of a kayak.

The paddle stroke itself consists of a movement called the forward stroke. The forward stroke happens when one of the paddle blades catches the water at the bow of the kayak, then a back swing occurs in which the paddle blade ends at the stern of the kayak. This movement is symmetrically completed with the other paddle blade to complete a full cycle of paddle strokes.

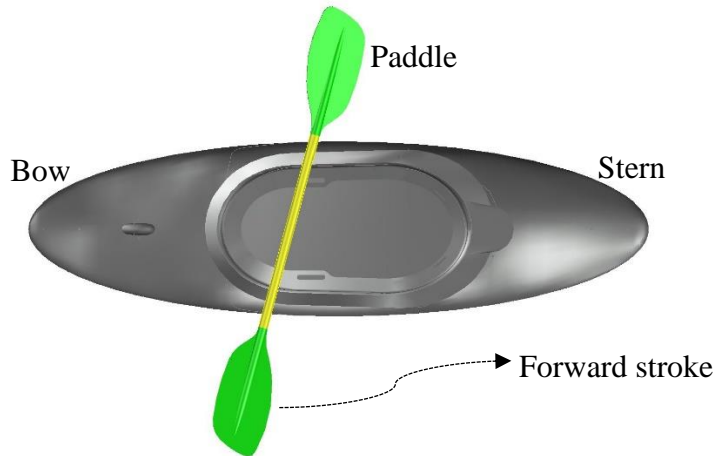


Figure 1.1: Anatomy of a kayak

The effect of this paddling motion is reflected in the dynamics of the hull of the boat. The cadence of the kayak due to a paddle stroke is dependant on the type of kayak used, the hydrographic environment, and the paddler themselves. Most importantly, the length and style of a kayak will contribute to the type of movement the kayak exhibits with each paddle stroke. For example, a

long kayak such as those used in sprint racing is optimized for forward movement, whereas a freestyle short kayak is designed for quick maneuverability in all directions. The kayak chosen for this project is a freestyle kayak, therefore the dynamics associated with this type of kayak are presented here and may not be applicable for all variations of kayaking. Another factor that affects kayak kinematics is the hydrographic environment. Flat or calm waters will most accurately reflect the paddle stroke movements on the kayak while choppy waters with rapids contain more noise in the kayak's kinematics. Finally, different paddlers will exhibit different cadence and variations in paddle strokes, which can contribute to different hull motions as well.

The dynamics of a kayak can be classified in terms of pitch, roll, and yaw which are illustrated in Figure 1.2. The pitch is defined as a up-down rotation about the perpendicular axis, the roll is defined as a side-to-side tilting rotation around the bow-stern axis, and the yaw (heading) is defined as a turning rotation around the up axis.

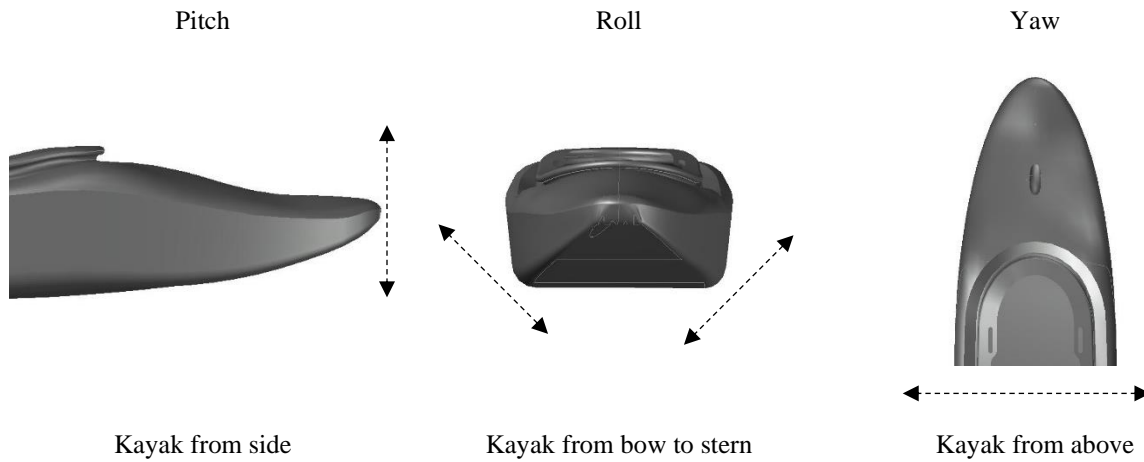


Figure 1.2: Kayak pitch, roll, and yaw

The forward stroke movement is most predominantly reflected in the roll and yaw angles of the kayak. The force of pushing water on one side of the kayak will rotate the bow of the kayak in the opposite direction, reflecting a variation in yaw. Each paddle stroke is completed by a rotation of the torso of the paddler which results in a shifting of weight in the kayak and a cadence in the roll angle from this shift. This cadence is shown in Figure 1.3. Similar to the findings in Halvorsen & Olsson (2016), the body of the kayak will return to the same orientation periodically creating a cyclic motion in the roll and yaw angles of the boat. The pitch of the kayak is a non-uniform motion and a function of paddler movement and water conditions creating a noise-like signal.

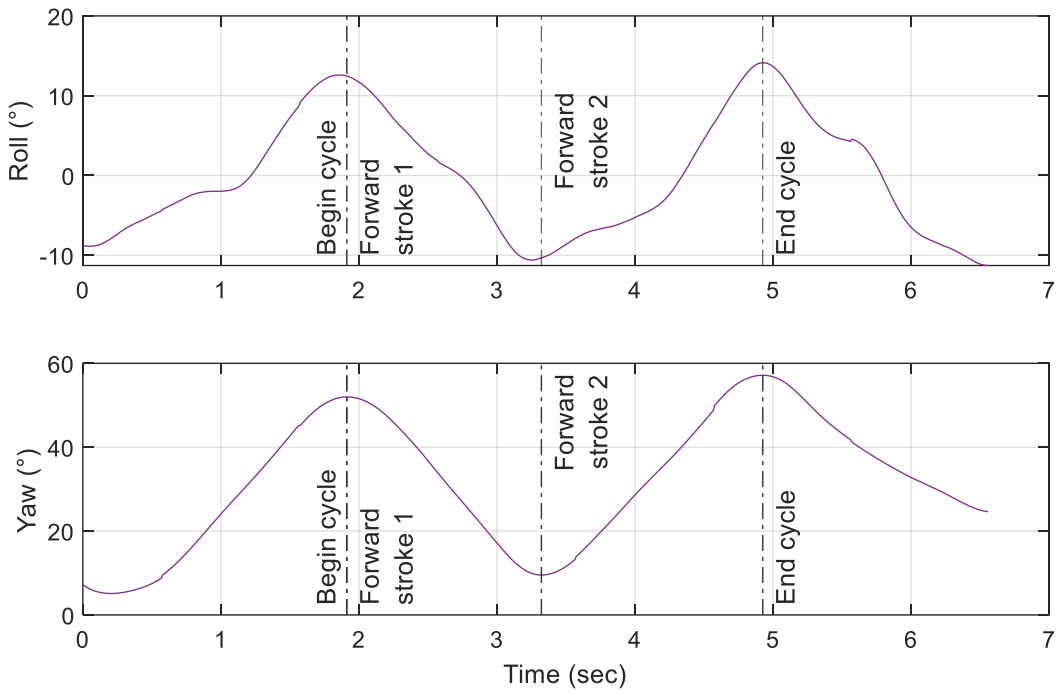


Figure 1.3: Kayak cadence

The cycle begins at ~2 seconds with the first paddle blade in the water at the beginning of the first forward stroke. The movement of the body weight as the paddle blade is pulled back shifts both the roll and yaw of the kayak as shown between 2 – 3.3 seconds. Forward stroke 2 then begins with the opposite paddle blade and the movement in these angles repeats itself in the opposite direction. A full cycle is completed once drive 2 is finished, then the cycle is repeated.

1.2 Objectives and Scope

There is a significant gap in literature regarding absolute positioning and tracking in river kayaking using smartphones. Previous kayaking literature primarily focus on the biomechanics of a paddler by utilizing ergometers, cameras, accelerometers, gyroscopes, force transducers, and GPS. Previous work regarding Android smartphones includes positioning for vehicular or pedestrian applications. Kayaking is a sport enjoyed both competitively and recreationally and the requirements for these different users vary. Boater cross and slalom canoe-kayak are both competitive sports in which athletes race down a course and navigate by passing in and out of gates. Performance in these races rely on both the dynamics of the paddler and the trajectory or

boat path of the kayak. These metrics often require sub-decimetre level positioning to be useful in determining an athlete's performance on the racecourse. In recreational kayaking, the safety of a paddler on a river is contingent on boat path or "lines" through various rapids or splits in the river. This line to navigate a rapid safely may have a small tolerance, therefore the trajectory recorded must be as accurate as possible, ranging from half-metre to metre level positioning depending on the type of river or creek. The knowledge of a rivers' characteristics is often shared verbally through paddling communities, which is vitally important given the ever-changing nature of rivers. While there are existing applications and databases designed for land-based activities to track and share hiking, cycling, and running trails, there are currently no applications tailored for kayaking.

The objective of this thesis is to develop and assess a strapdown, smartphone-based GPS/INS navigation solution for kayaking with an emphasis on improving the accuracy of the stand-alone INS during GPS outages. Given the lack of research in kayak specific navigation with low-cost GPS/INS systems, the objectives of the research are defined as the following:

- Develop and analyze traditional closed-loop loosely and tightly coupled GPS/INS configurations using raw smartphone observations from the accelerometer, gyroscope, and GPS. The relative difference in the performance of these navigation solutions is analyzed and compared to a reference trajectory from a higher-grade system to assess the benefits of each approach.
- Investigate the system positioning accuracy of the inertial solution during GPS outages. Partial and full GPS outages are simulated where insufficient satellites or no satellites are available for the GPS solution to assess the performance of the loosely and tightly coupled GPS/INS filters.
- Develop kayak-specific motion constraints to improve the stand-alone INS performance during GPS outages. Gyroscope errors are investigated as they have the most significant impact on the INS and a solution is proposed to estimate gyroscope bias based on the knowledge of a kayak's movement.
- Investigate the performance of the GPS/INS system aided by the proposed motion constraints. The effectiveness of the proposed solution is evaluated by comparing it to the traditional GPS/INS configuration.

The scope of this project is defined by the following:

- GPS/INS integration configurations are limited to loosely and tightly coupled only. Ultra-tightly integration is not considered or used because access to the internal GPS hardware is normally required which is not readily available for consumer devices.
- The sensors used in this research are limited to an accelerometer, gyroscope, and GPS. The main objective of this work is creating a consumer grade solution with the available hardware that is commonly found on an Android device. Therefore, additional hardware such as external antennas or relative position techniques like RTK are not in the scope of the project.
- The data collection is limited to strapdown navigation from an Android smartphone capable of collecting raw GPS and IMU measurements. The smartphone is rigidly mounted to the deck of the kayak and the methods proposed in this thesis are only valid for this scenario and not for a paddle-mounted, handheld, or pocketed smartphone.

1.3 Outline

This project incorporates the design and implementation of a low-cost GPS/INS system for the continuous tracking of a kayak. This thesis includes six chapters and three appendices.

Chapter 1 presents the motivation, problem definition, and scope of this work. Previous related works and limitations are provided to identify the research objective of this work.

Chapter 2 provides an overview of the navigation systems used in this work. GPS measurements and errors are discussed. The fundamentals of GPS is introduced with an emphasis on different types of GPS measurements and quality of smartphone GPS measurements. Then, reference frames, associated mechanization equations, and error equations are presented for inertial systems.

In Chapter 3, the estimation techniques used in this work are reviewed. These include least squares and Kalman filtering. GPS/INS integration techniques are then presented with an overview and comparison of both loosely and tightly coupled architectures. This chapter also presents the system models used in this work for GPS-only positioning, loosely coupled GPS/INS positioning, and tightly coupled GPS/INS positioning.

Chapter 4 describes the procedures completed for real world data collection including details on the hardware used, reference trajectory, and software development. The results obtained from this data are compared with the reference solution for a performance evaluation. Specific emphasis is given to the results obtained during a partial or full GPS outage and some challenges related to INS positioning are raised.

In Chapter 5, motion constraints applied specific to kayak dynamics to address the INS positioning issues of the previous chapter are presented. An assessment of the performance of the system with and without constraints is compared and evaluated.

Chapter 6 concludes the thesis, summarizes major results, and provides recommendations for future work.

The appendices include detailed information and are referenced throughout this thesis on the relevant topics they pertain to.

Chapter 2: Systems Overview

Background information pertaining to the fundamentals of GPS navigation and INS used in this research are described in this chapter. Firstly, the principles of GPS and smartphone GPS measurement quality are introduced. Next, inertial navigation including MEMS sensors and associated errors, alignment, and mechanization procedures are reviewed.

2.1 GPS Measurements

GNSS is a satellite-based positioning system that provides a 3D absolute position of a user's location on the Earth's surface via trilateration by tracking satellites. GNSS is composed of multiple different constellations of satellites that are in use today including GLONASS, Galileo, QZSS, and BeiDou which are maintained by Russia, Europe, Japan, and China respectively. The GPS constellation is operated and maintained by the United States of America and GPS will be used as an example of GNSS in this thesis. The methods described in this work are for GPS positioning and applications and can be used for other constellation systems as well.

The GPS signal is composed of a carrier that is modulated with a pseudorandom noise (PRN) code and a navigation message. The navigation message contains a dynamic model for the prediction of parameters such as satellite orbital position, clock corrections, ionospheric corrections, and tropospheric corrections. A PRN code is used to modulate each signal transmitted from each GPS satellite. The use of different PRN codes for each satellite enables code division multiple access, in which multiple signals can be transmitted on the same frequency at the same time without major interference. The decoding of each PRN code through a correlation process also enables the measurement of time of flight which is then converted into a pseudorange observation. GPS satellites also modulate a lower rate navigation data message onto most signals. Modern GPS satellites transmit on three radio frequencies: L1, L2, and L5 which have the frequencies of 1575.42, 1227.60, and 1176.45 MHz respectively (Misra & Enge, 2011). Each frequency is modulated by several PRN sequences or codes that support ranging measurements for different classes of users. On L1, the course acquisition (C/A) code is primarily for civilian use, while the encrypted P(Y) and M codes are restricted to authorized security and military users. The C/A code is modulated on L1, while the P-code is modulated on both L1 and L2 frequencies. L2 originally

only carried the P(Y) code but now transmits a new civil code called L2C and new signals are available on L5. The L1 C/A signal is the most widely used signal in GPS navigation for civilian applications. Further details regarding GPS signals and receiver architecture are found in literature (Kaplan & Hegarty, 2006; Misra & Enge, 2011; Wells et al., 1987). While raw GPS measurements have been used since the 1970s, they have only been available on Android devices for a few years.

A receiver's position is calculated by using distances from each known satellite position to the receiver in a trilateration algorithm. A clear line of sight is necessary to receive GPS signals from a satellite. Forestry, urban areas and buildings, and canyons can block the availability of these signals from the satellite to the receiver. GPS measurements are often paired with complementary systems such as magnetometers, barometers, odometers, map matching, and/or inertial sensors to overcome loss of line of sight between the satellite and receiver. More details on inertial sensor navigation are provided in section 2.2.

2.1.1 GPS Measurements

There are three basic types of GPS measurements that are available: pseudorange (code), phase, and Doppler measurements.

Pseudorange measurements are derived from PRN codes and is the measured distance between a satellite and receiver. The time taken for the signal to travel from a satellite to a receiver is translated into a distance by multiplying it by the speed of light. The generalized pseudorange measurement equation for a satellite is shown in (2.1) (Spilker Jr. et al., 1996).

$$P_p = \rho + c(\delta b_r - \delta b_s) + \delta d_{ion} + \delta d_{trop} + \delta d_{orb} + \varepsilon_{code} \quad 2.1$$

where:

P_p is the measured pseudorange

ρ is the true geometric range between the satellite and receiver antennas

c is the speed of light

δb_r is the receiver clock offset with respect to GPS time

δb_s is the satellite clock offset with respect to GPS time

δd_{ion} is the ionosphere error

δd_{trop} is the troposphere error

δd_{orb} is the orbital error

ε_{code} is the remaining error including multipath and noise

Carrier phase measurements are the distance between receiver to satellite that are measured by a sum of wavelengths or cycles of the carrier signal. Phase measurements can achieve an estimated precision of 2 mm for GPS L1 signals (Wells et al., 1987) which is much higher than that achieved by pseudorange measurements. This is because the carrier wavelength is small, it is about 19 cm for GPS L1 signals. The total carrier phase measurement is made up of the integer and fractional cycles as shown in (2.2). The fractional phase or change in integer offsets of the cycle can be accurately measured by the GPS receiver whereas the total number of wavelengths between the receiver and satellite is initially unknown and is referred to as integer ambiguity. Integer ambiguity can be estimated from the pseudorange measurements or position solution over multiple epochs and remains constant if no loss of lock occurs. However, finding the initial number of carrier integer cycles between the satellite and the receiver is very difficult. A loss of lock event, known as a cycle slip, results in a change in the carrier phase ambiguity. Cycle slips occur due to noisy signals, multipath, shaded antennas, and high receiver dynamics, and are most frequent in low quality receivers. The phase measurement equation is shown in 2.2.

$$\Phi_\lambda = \lambda N + \rho + c(\delta b_r - \delta b_s) - \delta_{ion} + \delta_{trop} + \delta_{orb} + \varepsilon_{carrier} \quad 2.2$$

where:

Φ_λ is the measured carrier phase (expressed in units of distance)

λ is the carrier wavelength

N is the carrier phase integer ambiguity

$\varepsilon_{carrier}$ is the measurement noise and error

The detection and resolution of cycle slips and integer ambiguity is crucial for effective use of carrier phase measurements. Cycle slip detection is more challenging in kinematic applications due to the unpredictable user motion which causes Doppler shift and is difficult to predict.

The Doppler measurement shown in (2.3) is the frequency shift of the signal caused by relative motion between the receiver and satellite. This measurement is valuable for estimating velocity of the receiver and for predicting the change in the phase measurement from one epoch to the next. The Doppler observation equation, expressed in units of range rate is:

$$\dot{P}_{\rho} = \dot{\rho} + c(\delta\dot{b}_r - \delta\dot{b}_s) - \dot{\delta d}_{ion} + \dot{\delta d}_{trop} + \dot{\delta d}_{orb} + \dot{\varepsilon}_{code} \quad 2.3$$

where:

\dot{P}_{ρ} is the measured pseudorange rate

$\dot{\rho}$ is the true range rate between the satellite and the receiver

$\delta\dot{b}_r$ is the receiver clock drift

$\delta\dot{b}_s$ is the satellite clock drift

$\dot{\delta d}_{ion}$ is the ionosphere induced drift

$\dot{\delta d}_{trop}$ is the troposphere drift

$\dot{\delta d}_{orb}$ is the orbital drift

$\dot{\varepsilon}_{code}$ is the code multipath and noise drift

In this work, only the pseudorange and Doppler measurements from L1 C/A were used as measurements. This is because these measurements are the most commonly available in smartphone receivers. The phase measurement is rarely used because cycle slips occur more frequently in these low grade receivers making carrier phase ambiguity estimation difficult (Humphreys et al., 2016; Zangenehnejad & Gao, 2021).

GPS measurements require the availability of satellite signals from at least four different satellites to calculate a receiver position and clock offset. The distance between a satellite and the receiver

is computed by using the signal propagation time between the transmitter and receiver (Dabve et al., 2020). The clocks in the transmitter and receiver are assumed not to be completely synchronized with one another, resulting in the receiver and satellite clock errors listed above. These errors can be estimated in a standalone positioning with one receiver or eliminated in double differencing positioning with two receivers. In standalone positioning, the satellite clock error is partially compensated using a model included in the broadcast navigation data, but the receiver clock offset is estimated as a bias along with the 3D coordinates of the receiver. Other sources of GPS errors are reviewed in section 2.1.2 and include multipath, and ionospheric and tropospheric delays.

In standalone or “single point” positioning, there are four unknowns which are the three receiver coordinates (x_R, y_R, z_R) and the receiver clock offset (δb_r). A simplified GPS measurement solution (2.4) can be used to represent the geometric range between a satellite and receiver position.

$$\begin{aligned} P_n &= \rho_n + c\delta b_r + \varepsilon_{code} \\ P_n &= \sqrt{(x^S - x^R)^2 + (y^S - y^R)^2 + (z^S - z^R)^2} + c\delta b_r + \varepsilon_{code} \end{aligned} \quad 2.4$$

where:

n is the number of satellites observed in k th epoch

x^S, y^S, z^S is the satellite position

x^R, y^R, z^R is the receiver position

The range-rate (2.5) is derived from the Doppler frequency of the signal received from a respective satellite.

$$\dot{P} = \dot{\rho} + c\delta\dot{b}_r + \dot{\varepsilon}_{code} \quad 2.5$$

Systems of equations composed of the pseudorange and range-rate observations can be solved using Least-squares and Kalman filtering, to estimate a receiver’s position and velocity. These estimation techniques are presented in Chapter 3.

2.1.2 GPS Errors

The overall GPS accuracy of a navigation solution can be affected by several ranging error sources. Satellite-based errors include orbit and satellite clock errors, and propagation errors such as ionosphere, troposphere, and multipath errors. Receiver-based errors include noise and receiver clock errors (Kaplan & Hegarty, 2006).

The ionospheric delay changes the transit time of a GPS signal. The ionosphere is a layer of the Earth's atmosphere that contains ionized air that is caused by the Sun's radiation. This ionization affects the refractive indices in layers of the atmosphere and can have an affect on or disperse different GPS frequencies. Satellite elevation contributes to the variability of ionospheric delay. A lower satellite elevation increases the distance a GPS signal travels through the ionosphere than a higher satellite elevation. Ionosphere delay can be eliminated through differential positioning techniques or the use of a dual frequency receiver. Single point positioning, or single frequency, requires the use of a model broadcast by the satellites to mitigate ionospheric error. Models such as Klobuchar, NTCM-BC, and BDGIM can be found in Yang et al. (2020).

The troposphere is the lower part of the atmosphere and contains a dry and wet part which causes GPS signals to refract while travelling through it. The dry component is composed of dry gases and affects 90% of the tropospheric error and the wet component, made up of water vapour, makes up the other 10% of tropospheric error. Similar to the ionospheric delay, the dry and wet tropospheric components can be mitigated with double differencing or using models such as the Hopfield, Chao, or Sasstamoinen models (Spilker Jr. et al., 1996).

Multipath occurs when a GPS signal reflects off different surfaces and results in the signal reaching the receiver via a different path other than a direct line of sight path. The signal that is affected by multipath arrives at the receiver with a delay and a bias is introduced to the ranging measurements. Multipath is difficult to model and eliminate because it is dependent on the environment surrounding the receiver (Spilker Jr. et al., 1996).

Orbital errors occur when there is a difference between the actual position of a satellite and the calculated position by the receiver using ephemeris data. The orbital parameters are predicted by and uploaded to the satellites by the control segment, then transmitted to receivers by the broadcast ephemeris.

Differential positioning and dual-frequency receivers can be used to overcome some of the errors presented in this section. In this work, only single point positioning and single frequency is used as it is the most common mode of positioning for consumer smartphone receivers. These errors can still be reduced in single point positioning, and further resources for negating these errors can be found in Kaplan & Hegarty (2006), Misra & Enge (2011), and Wells et al. (1987).

2.1.3 GPS Measurement Quality from Google Pixel 4

The positioning performance of a GPS smartphone solution is reliant upon the observation quality of the measurements collected. As mentioned in section 1.1, precise positioning is challenged by noisy measurements because of multipath and receiver noise, therefore, the quality of measurements is important in precise positioning. An example of observation quality on GPS measurements collected from a Google Pixel 4 are provided in this section.

Since 2016, Android devices with an API 24 are able to access raw GPS measurements. However, these measurements do not directly provide pseudorange and Doppler but the data necessary to generate these measurements are observed in the raw GPS parameters (European GNSS Supervisory Authority., 2017). A few of the raw measurements recorded by an Android system are shown in Table 1, a comprehensive list of these measurements and their uses can be found in Appendix A.

Table 1: Raw GPS measurements

Field	Description
TimeNanos	Receiver's hardware clock value
FullBiasNanos	Difference between the receiver's clock and true GPS time since 0000Z, January 6, 1980
BiasNanos	Sub-nanosecond of FullBiasNanos
DriftNanosPerSecond	Receivers' clock's drift
HardwareClockDiscontinuityCount	Count of hardware clock discontinuities
LeapSecond	Leap second associated with the clock's time
ChipsetElapsedRealTimeNanos	Time since system boot
ConstellationType	BeiDou, Galileo, GLONASS, GPS, QZSS, SBAS
Svid	Satellite ID
State	Sync state including Code lock, bit sync, frame sync
ReceivedSvTimeNanos	Received satellite time at the measurement time
ReceivedSvTimeUncertaintyNanos	Error estimate of ReceivedSvTimeNanos
TimeOffsetNanos	Time offset if measurements are asynchronous
CarrierCycles	Number of full carrier cycles between the satellite and receiver
PseudorangeRateMetersPerSecond	Pseudorange rate (Doppler)
PseudorangeRateUncertaintyMetersPerSecond	Error estimate of PseudorangeRateMetersPerSecond
CarrierFrequencyHz	Carrier frequency of the tracked signal

These raw measurements can then be used to compute the GPS time, pseudorange, Doppler, and carrier phase measurements that are used in navigation algorithms to provide the user's position and velocity. A more substantive review of connecting raw GNSS measurements to pseudorange and Doppler measurements from an Android device can be found in the white paper published by the European GNSS Supervisory Authority (2017).

The pseudorange is computed as a function of received measurement time and transmitted time as shown in (2.6) and the Doppler measurement in (2.7).

$$\rho = \frac{t_{Rx} - t_{Tx}}{10^9} c \quad 2.6$$

$$\dot{\rho} = PseudorangeRateMetersPerSecond \quad 2.7$$

where:

t_{Rx} is the received measurement time (expressed in nanoseconds)

t_{Tx} is the transmitted measurement time (expressed in nanoseconds)

PseudorangeRateMetersPerSecond is a Doppler measurement given by the Android device

To analyze the quality of the GPS measurements from a Google Pixel 4 smartphone, a short kinematic dataset was collected with the phone strapped to the deck of a kayak in flat water with open-sky conditions for optimal satellite visibility. Figure 2.1 illustrates the availability of carrier phase measurements in this dataset. The blue lines indicate periods of time where these measurements were available, while the red lines indicate time when carrier phase observations were unobservable and code observations were still available. Carrier phase continuity is important to resolve integer ambiguities in phase measurements for precise positioning. However, low grade receivers make ambiguity resolution difficult due to the number of cycle slips. Loss of lock occurs more frequently making carrier phase ambiguity estimation and subsequently phase positioning via a Google Pixel 4 difficult.

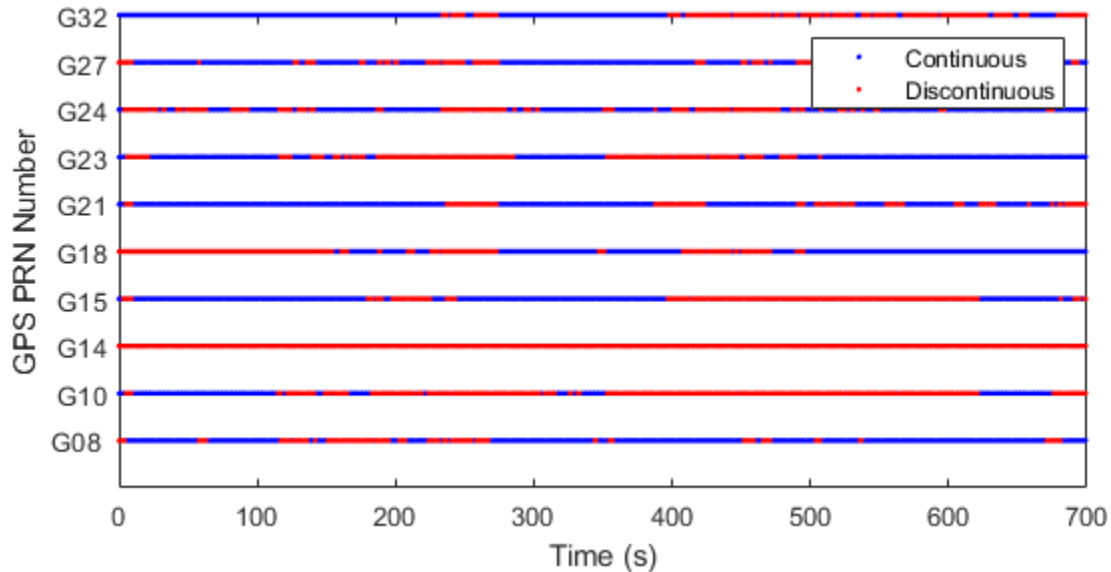


Figure 2.1: Carrier phase availability

As indicated in Figure 2.1, the code measurements are readily available throughout the observation time and can be relied upon to provide a position. Figure 2.2 illustrates the estimated residuals from a LS solution with code measurements as a function of satellite elevation and time. An elevation mask in this solution was set to 15° to minimize atmospheric errors in the GPS

measurements. The pseudoranges have an uncertainty of 2-5 metres with outliers that can be filtered to improve the accuracy of the solution.

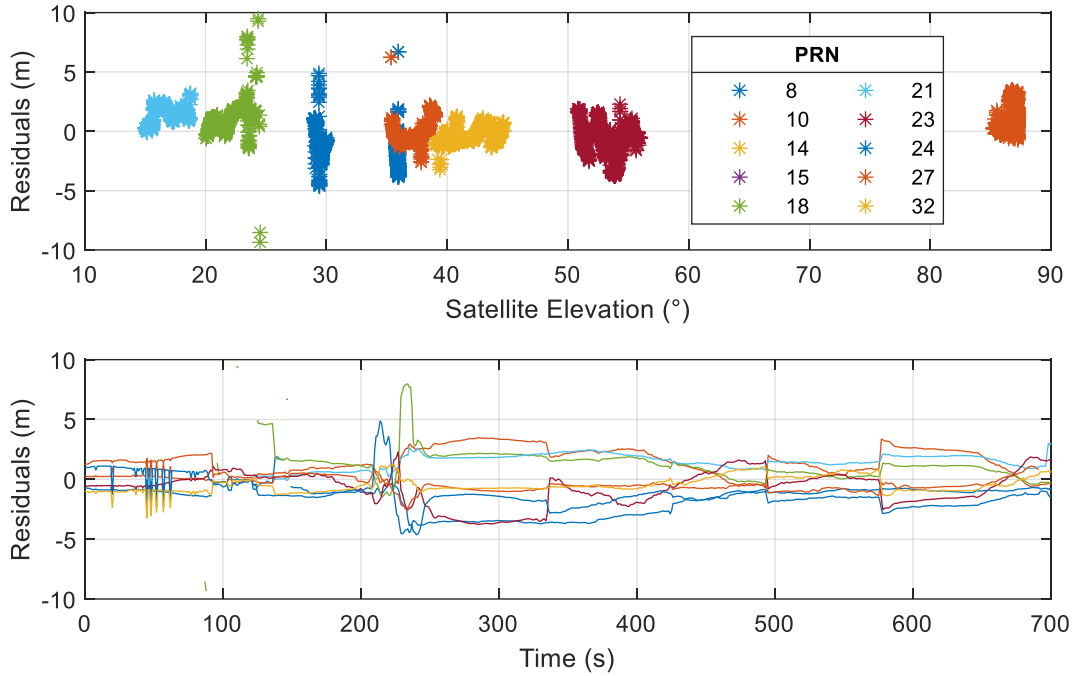


Figure 2.2: LS residuals as a function of satellite elevation angle and time

To overcome any limitations of GPS positioning such as outages in code observations, INS can be used. An overview of INS is provided in the next section.

2.2 Inertial Navigation Systems

INS-based positioning often works on the principle of dead reckoning in which accelerometers and gyroscopes are used to estimate the change in position, velocity, and attitude from a known previous position. Unlike GPS, which is a reference-based system, INS is wholly self contained and does not rely on external sources for measurements. Inertial navigation is an iterative process which makes use of the solution from the previous iteration, this process is shown in Figure 2.3. To begin the iterative process, the initial parameters of position, velocity, and attitude must be known; these parameters can be determined in a process known as ‘Alignment and Initialization’ and are described in section 2.7.

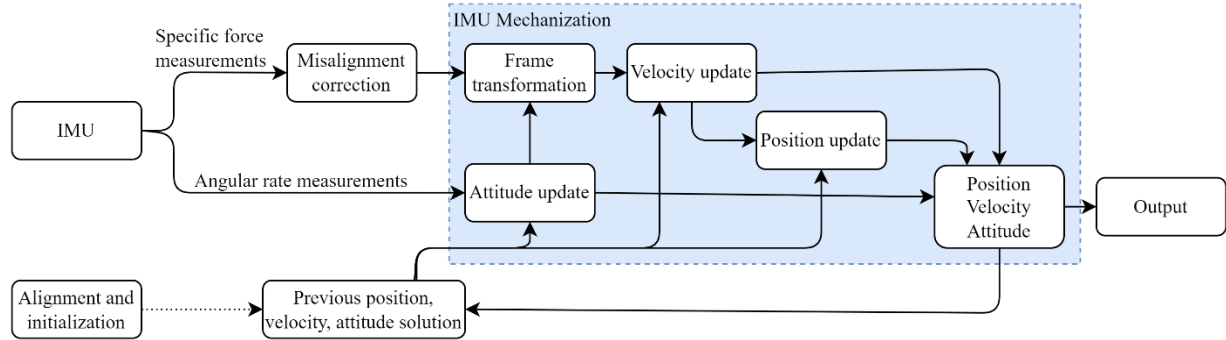


Figure 2.3: Inertial navigation schematic

INS often makes use of accelerometers and gyroscopes to measure specific force and angular velocity along 3 orthogonal axes respectively. The measurements from the sensors are recorded in a different frame from which position, velocity, and acceleration are expressed. A description of the difference reference frames used in this work is provided in section 2.3. The angular velocity of a device is used to transform parameters from an inertial reference frame to the navigation frame. The specific force measured from the accelerometer is integrated with respect to time to derive velocity, and velocity is further integrated to find the sensors displacement. This process is referred to as INS Mechanization and is further detailed in section 2.8. The measurements that are collected from the inertial sensors are in the device frame and must be rotated to the body frame before the mechanization process begins. This transformation uses a misalignment technique and is discussed in section 2.9.

All sensors are subject to errors which increase with every integration of time, these errors are discussed in section 2.6. Sensor calibration and modelling can be used to mitigate sensor errors and increase the performance of the INS. Sensor noise in a low grade platform will cause the performance of an INS to decrease significantly over time and must be corrected to maintain a precise solution (Sheta et al., 2018). High-cost INS are often used in aviation, marine, and vehicle navigation provide more precise solutions than low grade INS. However, high grade INS can be large and expensive, and therefore are not practical for most consumer or mainstream applications. The INS employed in this thesis is composed of a low-grade accelerometer and gyroscope which is built into the smartphone and some methods (discussed in Chapter 1) that reduce these sensor errors are ZUPT, ZVU, and non-holonomic constraints.

2.3 Reference Frames

Several different reference frames are used in inertial navigation, including an inertial frame, Earth-centered frame, local-level frame, and body frame (Figure 2.4). These frames provide 3D information of a point relating to a reference. The main coordinate frames used in this research and navigation are defined in this sub-section.

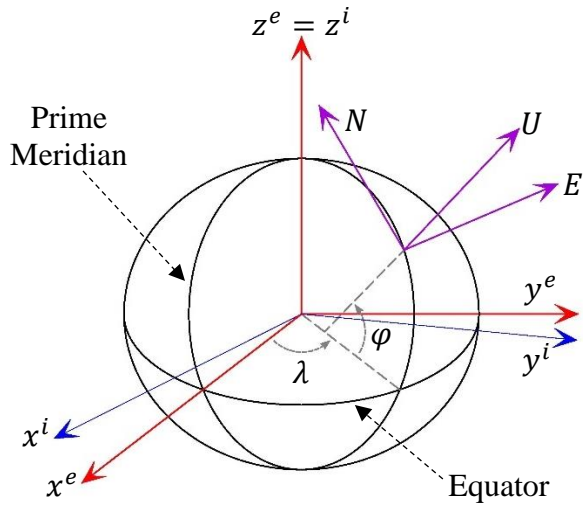


Figure 2.4: i-, e-, and ENU-frames

2.3.1 Earth-Centered Inertial Frame (*i*-frame)

In navigation, an Earth-centered inertial (ECI) frame (*i*-frame) is used which is centered at the Earth's center of mass and the Earth's spin axes and the direction of the vernal equinox define the orientation. The *ECI*- or *i*-frame frame does not accelerate nor rotate; it is defined to be stationary or moving at a constant velocity with no acceleration. Accelerometers and gyroscopes measure the movement of the implement they are attached to relative to the inertial frame. The origin of this frame coincides with the centre of the Earth. The *x*-axis is in the equatorial plane and points to the Vernal Equinox, the *z*-axis points along the Earth's axis of rotation through the North pole, and the *y*-axis completes the right-handed system.

2.3.2 Earth-Centered Earth-Fixed Frame (*e*-frame)

The Earth-centered Earth-fixed (ECEF) frame (*e*-frame) is a cartesian reference system and has an origin at the centre of the Earth's mass and rotates with the Earth's rotation about its vertical axis. The *z*-axis coincides with the Earth's axis of rotation along the North pole. The *x*-axis points through the intersection of the equator with the Greenwich meridian and the *y*-axis completes the right-handed system. The *e*-frame can be converted to geodetic coordinates using a geodetic datum; the datum used in this project is WGS 84. The geodetic coordinates are represented by Latitude (φ), Longitude (λ), and height (h), which are defined by angles in the meridian plane, and equatorial planes. Details of the conversion between cartesian and geodetic systems can be found in Appendix B.

2.3.3 Local-level Frame (*l*- or *ENU*-frame)

In the local level frame (*l*-frame), the origin coincides with the center of the target and the *x*-axis points to east, the *y*-axis points to geodetic north, and the *z*-axis is perpendicular to the reference ellipsoid in a right-handed coordinate system. This frame is also known as the navigation or East-North-Up (ENU) frame. Another version of the *l*-frame is the North-East-Down in which the *z*-axis is perpendicular to the reference ellipsoid. Note that North-East-Down is also a right-handed coordinate system. Both conventions are common in literature (Groves, 2007), however the ENU-frame will be used in this thesis

2.3.4 Body and Device Frame (*b*- and *d*-frame)

The body frame (*b*-frame) is often fixed with respect to the body of the navigating object and may also correspond to the orientation of the IMU axis. In strapdown navigation, the body frame often refers to the body of which the device is strapped down against. As such, the body or vehicle may have a forward-across-down or across-forward-up frame that may differ from the IMU axes.

The *b*-frame used in this thesis refers to the frame of the kayak that the smartphone is strapped on to and the device frame (*d*-frame) refers to the IMU axes within the smartphone. In both frames, the *y*-axis is defined as forward, the *z*-axis points up in the opposite direction of gravity, and the *x*-

axis completes a right-handed coordinate system for a across-forward-up frame. This is illustrated in Figure 2.5. The b -frame and d -frame are represented by the blue and green arrows respectively. In this project, the x -axis and y -axis will be interchangeably referred to as the across track and along track directions respectively, while the z -axis may be referred to as the up direction. However, the b - and d -frame defined in this project are not aligned exactly with each other and will be slightly skewed. Therefore, a misalignment technique is used to rotate and align the d -frame and the b -frame and is explained section 2.9.

The attitude angles of the body frame with respect to the navigation frame are called roll (r), pitch (p), and yaw (ψ_y). This work utilizes both yaw and azimuth angles which are measured as a rotation around the z -axis. The yaw angle is measured counterclockwise from north and is represented with ψ_y . Azimuth is measured clockwise from north and is represented with ψ_A . The roll of the body frame is a rotation around the y -axis, the pitch is a rotation around the x -axis, and the yaw or azimuth is a rotation about the z -axis in the right-hand system.

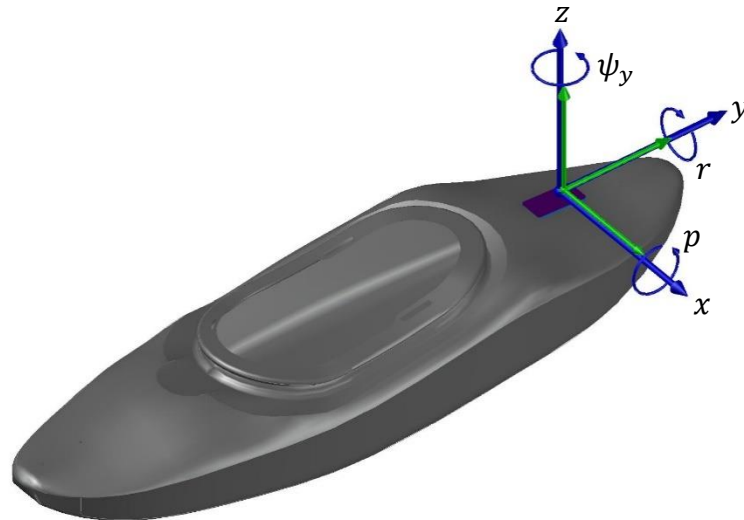


Figure 2.5: Body and device frame

2.4 Frame Rotations

Rotations between coordinate frames is necessary to convert measurements taken in the b -frame to the e -frame and the l -frame. The rotation matrix to transform a vector from one frame to another uses a combination of rotation matrices and is represented as R_j^k where the j indicates the original frame and k indicates the frame the vector will be rotated to. The inverse transformation from k to j is illustrated in equation 2.8.

$$R_k^j = (R_j^k)^T = (R_j^k)^{-1} \quad 2.8$$

The rotation around the X, Y, and Z axes in a right-handed system are expressed by the following elementary matrices respectively (Noureldin et al., 2013).

$$R_1(\xi) = \begin{bmatrix} 1 & 0 & 0 \\ 0 & \cos\xi & \sin\xi \\ 0 & -\sin\xi & \cos\xi \end{bmatrix} \quad 2.9$$

$$R_2(\xi) = \begin{bmatrix} \cos\xi & 0 & -\sin\xi \\ 0 & 1 & 0 \\ \sin\xi & 0 & \cos\xi \end{bmatrix} \quad 2.10$$

$$R_3(\xi) = \begin{bmatrix} \cos\xi & \sin\xi & 0 \\ -\sin\xi & \cos\xi & 0 \\ 0 & 0 & 1 \end{bmatrix} \quad 2.11$$

The transformation from the i -frame to the e -frame is a rotation around the Z-axis and is given by:

$$R_i^e = R_3(\omega_e t) \quad 2.12$$

where:

ω_e is the magnitude of the Earth's rotation rate

t is the time passed since the last reference epoch

The transformation from the e -frame to the l -frame is shown by equation 2.13.

$$R_e^l = R_3(-90 - \lambda)R_1(\varphi - 90) \quad 2.13$$

The transformation from the b -frame to the l -frame is given by:

$$R_b^l = R_3(-\psi_y)R_1(p)R_2(r) \quad 2.14$$

where (p, r, ψ_y) represent the pitch, roll, and yaw respectively.

Finally, the transformation from the d -frame to the b -frame is:

$$R_d^b = R_3(\xi_{\psi_y})R_1(\xi_p)R_2(\psi_r) \quad 2.15$$

where $(\xi_p, \xi_r, \xi_{\psi_y})$ represent the misalignment angles between pitch, roll, and yaw respectively.

2.5 MEMS Sensors

The inertial sensors built into the Google Pixel 4 smartphone are a MEMS accelerometer and a gyroscope that provide raw motion sensor data. MEMS sensors are characterized by their small size, light weight, low cost, and low power consumption comparatively to high-cost inertial sensors. These features lend MEMS sensors to be more accessible for consumer applications such as pedestrian navigation and smartphone integration. MEMS sensors have greater shock tolerance than conventional mechanical designs; however, they typically have poorer performance (Groves, 2007). Because of this limited performance, MEMS sensors are unable to be used independently for extended periods of time and are therefore often integrated with external navigation solutions to improve the solution. The performance of a MEMS-based inertial sensor can be improved through sensor calibration or modelled as a random process to mitigate systematic or stochastic errors; these errors are explained in section 2.6. An accelerometer and gyroscope triad can measure specific force and angular velocity along three orthogonal axes respectively. These accelerometers and gyroscopes operating in conjunction form an IMU.

Accelerometers measure specific force of a motion and are used to derive 3D linear motion. The body frame for accelerometers is the case in which they are attached to, and the reference is the inertial frame; therefore, an accelerometer measures specific force of the body frame with respect to the inertial frame. Accelerometers measure specific force of what they are attached to, not the

total acceleration. For instance, if the accelerometer were placed in a vacuum with no movement, the force read by the device is zero because there are no external forces acting upon the device nor movements of the device. However, the force of gravity outside of a vacuum will cause the accelerometer measurement to be displaced downwards with respect to the gravity axis. Therefore, it is important to counteract the force of gravity measured by the accelerometer to compute an accurate output of acceleration of the device.

There are many categories of accelerometers including proof mass, pendulous, vibrating-beam, and drag cup (Grewal et al., 2007; Kraft & Lewis, 1997; Noureldin et al., 2013). The different types of accelerometers vary by size, mass, sensitivity, and cost depending on the performance of an accelerometer. MEMS accelerometers are built with axes both in the plane of the device and perpendicular to that plane, creating a three-axis triad. Proof mass and vibrating beam accelerometers are the most common types used for MEMS sensors.

A gyroscope is a sensor that measures angular rates (Noureldin et al., 2013). These angular rates can then be integrated with respect to time to provide the change in angle that has occurred from an initially known orientation. A few different types of gyroscopes are dry tuned, vibrating, and MEMS gyroscopes.

MEMS gyroscope sensors use vibrating mechanical elements to sense rotation with no rotating parts, this makes them easily miniaturized and fabricated (Yazdi et al., 1998). There have been several different types of MEMS gyroscopes produced including vibrating beams or rings, tuning forks, spinning disks, and surface-acoustic waves (Xie & Fedder, 2003).

The components in low-cost MEMS sensors are not yet precise enough to detect the Earth's rotation rate (Chandra, 2019). The sensor integrated in the smartphone (Google Pixel 4) is a Bosch BMI263 (*BMI263*, n.d.; *Pixel Phone Hardware Tech Specs - Pixel Phone Help*, n.d.; *Snapdragon 855 Mobile Platform*, 2018). The gyroscope in the BMI263 measurement per least significant bit (LSB) is 16.4 LSB/deg/sec which is equivalent to 0.0610 deg/sec (219.51 deg/hr) (*BMI263*, n.d.). This low-grade gyroscope measures at a rate higher than the Earth's rotation rate of approximately 0.0042 deg/sec or 15 deg/hr and is therefore unable to measure the Earth's rotation rate.

2.6 Inertial Sensor Errors

Gyroscopes and accelerometers are subject to errors which can limit the accuracy, repeatability, and stability of the observations measured. Sensor bias offset, scale factor error, non-orthogonal axes, and sensor noise are the primary systematic or deterministic errors of these sensors. Stochastic errors of these sensors occur with randomness of the inertial sensors and are classified as random walk by sensor manufacturers. The accelerometer and gyroscope measurement models with errors are shown in (2.16). For further review regarding inertial sensor errors including non-linear scale factor and cross-coupling errors, refer to Groves (2007) and Noureldin et al. (2013).

$$\begin{aligned} f^b &= \tilde{f}^b + b_a + S_a f^b + N_a f^b + \varepsilon_f \\ \omega^b &= \tilde{\omega}^b + b_g + S_g \omega^b + N_g \omega^b + \varepsilon_\omega \end{aligned} \quad 2.16$$

where:

f^b and \tilde{f}^b is the measured and true specific force in the body frame (f_x^b, f_y^b, f_z^b)

ω^b and $\tilde{\omega}^b$ is the measured and true angular rate in the body frame ($\omega_x^b, \omega_y^b, \omega_z^b$)

b_a and b_g is the accelerometer and gyroscope sensor biases respectively

S_a and S_g is the accelerometer and gyroscope scale factors respectively

N_a and N_g is the non-orthogonality of the accelerometer and gyroscope triad respectively

ε_f and ε_ω is the sensor noise of the accelerometer and gyroscope respectively

MEMS sensors can exhibit high error sources over short time intervals such as bias which degrades the accuracy of the system, thus limiting the possibility of using MEMS technology for high-accuracy applications. Therefore, MEMS sensors are only accurate for a short amount of time without additional aiding sensors or proper calibration. An ideal gyroscope with no bias will output a value of zero when no input is applied. An ideal accelerometer will output a value for gravity acceleration only when no input is applied. However, MEMS sensors will output a non-zero value which is known as the bias. The sensor bias can be split into a deterministic part and a stochastic part which are referred to as bias offset and bias drift respectively. A bias offset is a constant error

that is exhibited by inertial sensors and can be determined by calibration. Bias drift is the rate in which error accumulates with time, this error is random in nature and can be modelled as a stochastic process. MEMS-based gyroscopes exhibit sensor bias of 100°/hr and above (Aggarwal et al., 2010).

Scale factor error is the ratio of change between the output of a sensor and the input measurement. Accelerometer scale factor error is proportional to the specific force and gyroscope error is proportional to the angular rates about the sensitive axis. This error is deterministic and can be determined by calibration. It is generally evaluated as a slope and can be determined by least squares.

Accelerometers and gyroscopes are assumed to have triads that are mounted orthogonal. A deviation or misalignment of the sensitive axes with respect to the orthogonal axes results in a non-orthogonality error.

All sensors exhibit random noise and stochastic models can be used to represent and mitigate errors caused by noise, and the appropriate model is determined by the autocorrelation sequence of the output. Random noise from accelerometers or gyroscopes can sometimes be classified as velocity random walk and angular random walk respectively. Random noise on specific force or angular rate measurements is integrated to produce random walk errors.

2.7 Alignment and Initialization

Inertial navigation is wholly self-contained and does not rely on external information to provide a navigation solution; consequently, an initial starting position, velocity, and attitude are required (Groves, 2007), this process is known as alignment and initialization.

Attitude alignment is necessary to determine the platforms roll, pitch, and yaw. The pitch (2.17) and the roll (2.18) of the system are estimated using the Earth's gravity and accelerometer when the system is held stationary (Noureldin et al., 2013).

$$p = \tan^{-1} \left(\frac{f_y^b}{\sqrt{f_x^2 + f_z^2}} \right) \quad 2.17$$

$$r = \tan^{-1} \left(\frac{-f_x}{f_z} \right) \quad 2.18$$

In high-grade INS, the Earth's rotation rate is used in gyro-compassing to measure the rotation of the b -frame with respect to the e -frame to determine the yaw angle. However, the method of gyro-compassing in low-cost IMUs is not feasible due to the limitations of the sensors to detect and measure the Earth's rotation rate. Therefore, the heading initialization of yaw of low-cost systems rely on external sources such as GPS. Once the system has started to move, the GPS velocities are used to compute the initial yaw as shown in (2.19).

$$\psi_y = -\tan^{-1} \left(\frac{v_e}{v_n} \right) \quad 2.19$$

where v_e and v_n are east and north velocities respectively

2.8 Low-Cost INS Mechanization

Mechanization is the process of integrating the outputs from an IMU with respect to time to produce a relative position, velocity, and attitude solution. This process is recursive and begins with an initial set of values and iterates over the output. Further details of the mechanization equations can be found in various literature (Groves, 2007; Noureldin et al., 2013). The INS mechanization used in this thesis is completed in the l -frame and rotates the raw observations from the b -frame to the l -frame is shown in equation (2.20).

$$\begin{bmatrix} \delta \dot{r}^l \\ \delta \dot{v}^l \\ \dot{R}_b^l \end{bmatrix} = \begin{bmatrix} D^{-1} v^l \\ R_b^l f^b - (2\Omega_{ie}^l + \Omega_{el}^l) v^l + g^l \\ R_b^l (\Omega_{ib}^b - \Omega_{il}^b) \end{bmatrix} \quad 2.20$$

where:

δr^l is the position vector in the local geodetic WGS-84 frame containing Latitude ($\delta\varphi$), Longitude ($\delta\lambda$), and Height (h)

δv^l is the velocity state vector in ENU ($\delta v_e, \delta v_n, \delta v_u$)

$\delta \dot{r}^l, \delta \dot{v}^l, \dot{R}_b^l$ is the rate of change of position, velocity, and rotation states in the l -frame

D is the transformation matrix to transform velocity rectangular coordinates into curvilinear coordinates in the e -frame

Ω_{ie}^l is the skew-symmetric matrix of the rotation rate (ω_{ie}^e)

Ω_{el}^l is the skew-symmetric matrix of the Earth's rotation rate (ω_{el}^l)

Ω_{ib}^b is the skew-symmetric matrix of the rotation rate (ω_{ib}^b)

Ω_{il}^l is the skew-symmetric matrix of the rotation rate (ω_{il}^l)

g^l is the Earth's gravity field in the l -frame

Due to the inability of low-cost sensors to measure the Earth's rotation rate, the above mechanization equations can be simplified using the constraints in (2.21).

$$\begin{aligned}\omega_{ie}^i &= \omega_{el}^l = 0 \\ \Omega_{ie}^l &= \Omega_{el}^l = 0\end{aligned}\quad 2.21$$

2.9 Misalignment

Low-cost MEMS sensors, such as those found in a smartphone, are often used in portable devices, and may not be accurately aligned with the host body or vehicle. The device and body frame are assumed to have poor alignment accuracy which leads to a misalignment error. If the attitude angles of the INS can be negated, systems with no non-holonomic constraints and a misalignment error are able to produce sufficient results (Syed et al., 2008). However, the use of non-holonomic or motion constraints cannot be applied to a system if the IMU axis are not properly aligned to the host body of which the constraints are being applied to. In the case of GPS outages, INS applied motion constraints can improve navigation accuracy, therefore, it is important to align the IMU to the host body frame.

Tethered systems are mounted rigidly with the orientation between the sensor and host frame known, whereas the orientation in portable devices can change from run to run due to the detachment and attachment of the sensor to the host body. Therefore, it is important to calculate

the 3D misalignment between the device (smartphone) frame and the body (kayak) frame for each separate run to accurately track the trajectory and movement of the kayak itself. This enables the use of motion constraints in the navigation algorithm based upon the expected movement of a kayak.

Figure 2.5 describes the two frames used in this project and the corresponding misalignment angles. The b -frame (x^b, y^b, z^b) are represented by the blue arrows, d -frame (x^d, y^d, z^d) are represented by the green arrows, and the misalignment angles ($\xi_p, \xi_r, \xi_{\psi_y}$) are represented by the black arrows.

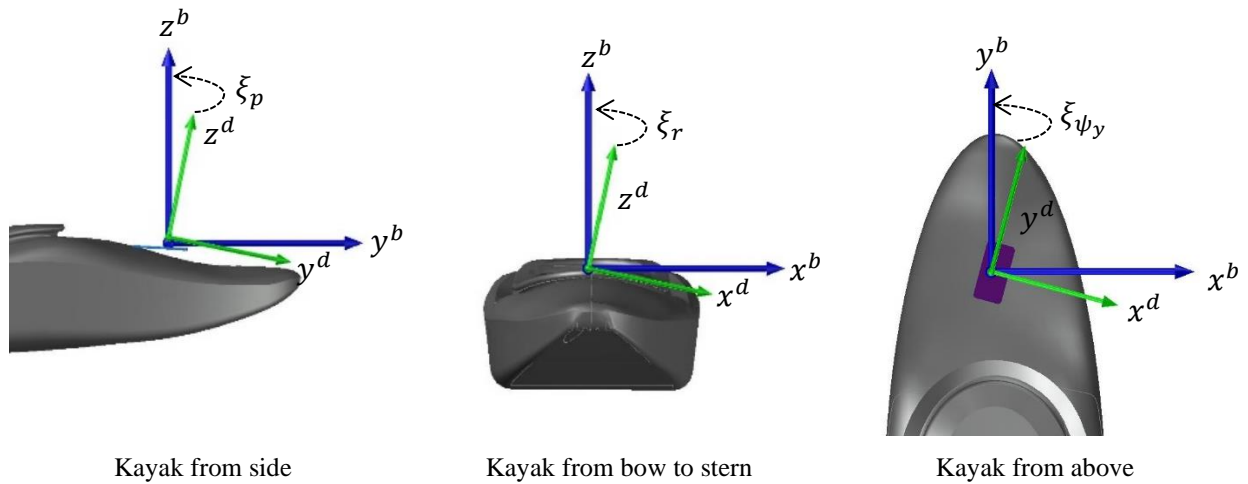


Figure 2.6: Device and body frames misalignment

The left diagram illustrates a side-view of the bow of a kayak with a pitch misalignment between the d -frame and b -frame; the center diagram is a backside view of a kayak with a roll misalignment, and the right diagram displays a top view of the bow of a kayak with a yaw misalignment.

Accelerometer levelling and heading misalignment are applied to align the d -frame to the b -frame. A direct cosine matrix is built to rotate the collected accelerometer data to coincide with the expected b -frame of the kayak. Yaw (ξ_{ψ_y}), pitch (ξ_p), and roll misalignment (ξ_r), are used in the misalignment matrix (R_d^b) to describe the rotation from the d -frame to the b -frame as expressed in (2.22).

$$R_d^b = R_3(\xi_{\psi_y}) R_1(\xi_p) R_2(\xi_r) \quad 2.22$$

Flat, calm water was used to complete accelerometer levelling based upon the assumption that calm water is a level, horizontal frame reflecting the kayak frame (*b*-frame). Prior to beginning each run, static data was collected for a length of time by sitting stationary in calm water. Accelerometers measure across-track and along-track acceleration in addition to gravity, therefore it is important that the data used to level the roll and pitch angles is stationary. Any movement side-to-side or forward-backward would contribute to the across-track and along-track accelerations that in turn would distort the misalignment. Theoretically, choppy water or paddler movement causing the kayak to shift during the alignment data collection can contribute to an incorrect misalignment being applied to the system. The recorded accelerations are then levelled by utilizing the roll and pitch values from the INS mechanization process. The roll and pitch values are assumed to be zero in stationary water and any deviation from these values contributes to a misalignment.

A combination of levelling and gyro-compassing can measure the specific force and Earth's rotation rate to determine the heading (Avrutov et al., 2017; Bao et al., 2013). This method is not feasible for low-cost systems because MEMS sensors are unable to measure the Earth's rotation rate. External sensors or sources can be used in lieu of gyro-compassing to determine heading of the *b*-frame, these may include heading from GPS velocity or other sensors such as a magnetometer. Once the host body begins to move, GPS velocity is used to find the heading as shown in (2.19). The yaw misalignment is evaluated as a difference between the measured d-frame yaw and GPS derived yaw in the b-frame (2.23).

$$\xi_{\psi_y} = \psi_{y_GPS}^b - \psi_{y_INS}^v \quad 2.23$$

The direct cosine matrix derived from the misalignment angles are then applied to the accelerations shown in (2.24).

$$f^b = R_d^b \cdot f_{raw}^b \quad 2.24$$

An example of the misalignment correction applied to measured specific forces is shown in Figure 2.7. The green lines represent the accelerations measured before the misalignment was applied (f_{raw}^b) and the blue lines represent accelerations after misalignment was applied (f^b). The expected

acceleration in the x and y directions is to be 0 when the kayak is stationary in the water. As depicted in the figure, the misalignment corrects the accelerations from the d -frame to the b -frame.

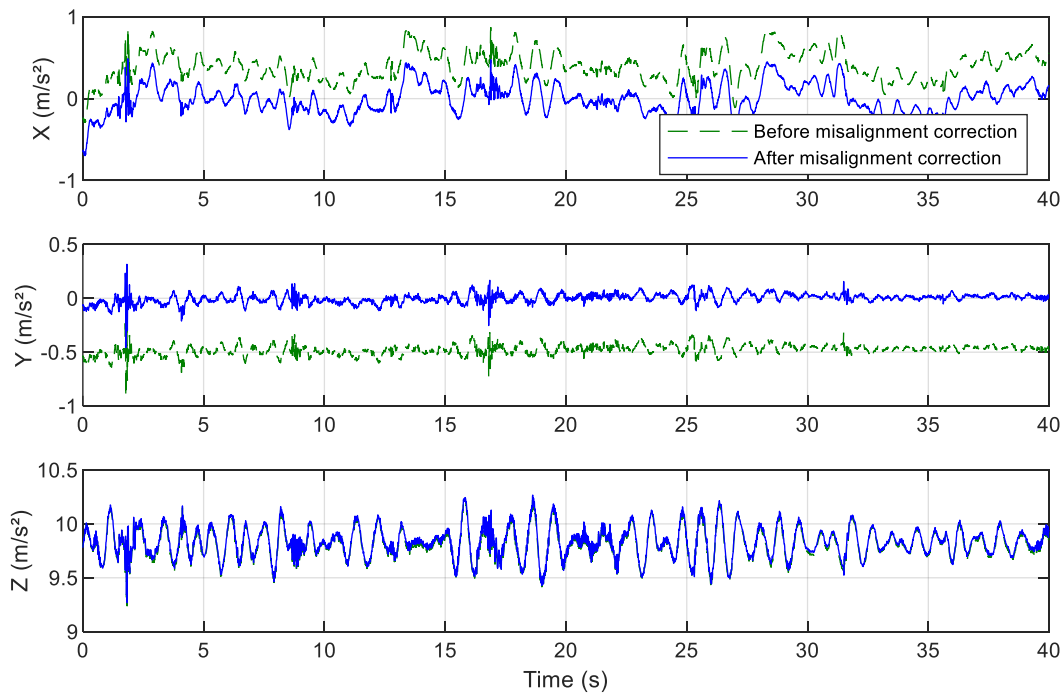


Figure 2.7: Measured accelerations before and after misalignment correction

Chapter 3: Estimation Techniques and GPS/INS Integration

Estimation is the process of obtaining the best estimate of unknowns or parameters from a set of observations (Petovello, 2003). Measurements may contain systematic errors, random errors, and blunders. Systematic errors can be removed through calibration methods; however, random errors or blunders remain within system measurements. Estimation algorithms and redundant observations can be used to minimize random errors and identify blunders in the data.

In estimation, a functional relationship called the measurement model is formed between the state estimates (unknowns) and the observations. The unknowns in this measurement model are then solved for using an estimation technique such as least squares (LS) or an extended Kalman filter (EKF). Both the LS and EKF can be used for satellite-based navigation algorithms, where LS computes a solution epoch-by-epoch and the EKF computes a solution based upon knowledge of how the state vector changes over time. The EKF estimator is also used as a means of integrating information from GPS and INS observations. In this section, estimation using LS is briefly presented followed by a review of estimation by EKF and a GPS estimation model. Next, GPS/INS integration is described along with the system models used in this thesis.

3.1 Least Squares

LS estimation is a mathematical model which minimizes the weighted sum-of-squares of the residuals (Gelb, 1974; Petovello, 2003; Sorenson, 1970). The principle used in LS is to minimize the difference between the observations and the estimates of the state vector (residuals) by means of maximum likelihood and minimum variance estimation. A discrete functional model, shown in (3.9), is used to describe linear LS and relates a set of measurements to unknown parameters or a state vector.

$$z_k = H_k x_k + w_k \quad 3.1$$

$$H_k = \frac{\partial z_k}{\partial x_k} \quad 3.2$$

where:

z_k is the measurement or innovation vector

H_k is the Jacobian (design) matrix of the measurements with respect to the unknown states

x_k is the state vector of unknown parameters

w_k is the measurement noise

k is k^{th} epoch at time t_k

LS estimates the state vector (\hat{x}_k) by minimizing the weighted sum of the squares of the residuals (3.3) in the function (3.4).

$$v_{noise_k} = z_k - H_k \hat{x}_k \quad 3.3$$

$$J_k = (z_k - H_k \hat{x}_k)^T W_k (z_k - H_k \hat{x}_k) \quad 3.4$$

where:

v_{noise_k} is the measurement noise vector

J_k is the function to be minimized

W_k is the weighting function

The LS estimate is found by differentiating J_k by the estimated state vector and setting the result to zero. The corresponding solution is:

$$\hat{x}_k = (H_k^T W^{-1} H_k)^{-1} H_k^T W_k^{-1} z_k \quad 3.5$$

The error covariance matrix of the estimated states ($C_{\hat{x}}$) is then found by applying the law of propagation.

$$C_{\hat{x}} = (H_k^T W^{-1} H_k)^{-1} (H_k^T W C_z W H_k) (H_k^T W H_k)^{-1} \quad 3.6$$

where C_z is the covariance matrix of observation errors

The weighting matrix in weighted LS can be set as an inverse of the observation error covariance matrix. This will simplify equation 3.5 and equation 3.6 respectively to:

$$\hat{x} = (H^T C_z^{-1} H_k)^{-1} H_k^T C_z^{-1} z_k \quad 3.7$$

$$C_{\hat{x}} = (H^T C_z^{-1} H)^{-1} \quad 3.8$$

In the context of GPS, the LS problem is a non-linear problem because the state vector is not directly observed, rather the state vector is derived using a measurement model relating the observations to the unknowns. The functional model of a non-linear LS is shown in (3.9) where equation (3.1) is linearized using Taylor series of expansion around the current state estimate (point of expansion) with a function that relates the unknown states to the measurements. The estimated state vector is used as a point of expansion to evaluate H .

$$z_k = h_k(\hat{x}_k) + w_k \quad 3.9$$

$$h_k = \left. \frac{\partial h_k}{\partial x_k} \right|_{x=\hat{x}_k} \quad 3.10$$

where:

$h_k(\hat{x}_k)$ is the predicted observation

h_k is a function relating the unknown states to the measurements

The measurement misclosure vector in (3.11) is the difference between the predicted and measured observation and the corresponding solution is shown in (3.12).

$$\delta z_k = H \delta x + w_k \quad 3.11$$

$$\delta \hat{x} = (H^T R^{-1} H)^{-1} H^T R^{-1} \delta z \quad 3.12$$

In a non-linear LS solution, multiple iterations are required for the solution to converge, while minimizing the residuals with each iteration. The estimated states are iterated until the convergence criteria is met when the correction vector ($\delta \hat{x}$) is small enough to be negligible in the solution.

3.2 Kalman filter

The LS method described in the section above provides state estimates on an epoch-by-epoch basis, meaning the estimates are time invariant and do not incorporate past and future states. The results from a Kalman filter are expected to be more accurate because past measurements are utilized recursively. The KF is a linear filter that supports estimations of past, present, and future states (Groves, 2007; Welch & Bishop, 1995). This filter adjusts current measured data by integrating past data to reduce the noise of the measured value (Park et al., 2019).

The discrete state measurement model for the KF is the same as in LS shown in (3.1). The linearized time system model is illustrated in (3.13). The state transition matrix in this equation is used to define the time evolution of the state estimates from epoch k to $k + 1$.

$$x_{k+1} = \Phi_{k,k+1}x_k + w_k \quad 3.13$$

where $\Phi_{k,k+1}$ is the state transition matrix from epoch k to $k + 1$. The states at epoch $k + 1$ are predicted as a linear combination of the states at epoch k including some errors.

The KF incorporates time updates to project the state estimates forward, with measurement updates to receive constant feedback for the state estimates. It is assumed that an a-priori state vector estimate and corresponding covariance is available to begin the filter. The state vector is assumed to be a random process that is uncorrelated with the noise of the system and can be modelled by a discrete system (Petovello, 2003; P. J. G. Teunissen et al., 2021). The KF operates on the assumption that the noise is random Gaussian distributed with a zero mean, and the process and measurement noise are uncorrelated with each other and the state vector.

The KF is a recursive algorithm consisting of two steps, prediction and update (Brown, 2012). The prediction step estimates the state vector (3.14) and the corresponding covariance matrix (P_k) (3.15) from the present epoch to the next epoch.

$$x_k^{(-)} = \Phi_{k,k-1}x_{k-1}^{(+)} \quad 3.14$$

$$P_k^{(-)} = \Phi_{k,k-1}P_{k-1}^{(-)}\Phi_{k,k-1} + Q_k \quad 3.15$$

where:

superscript $(-)$ represents a prior quantity (before measurement update)

superscript $(+)$ represents a corrected quantity (after measurement update)

P_k is the prediction and estimated error covariance of the state vector

Q_k is the process noise covariance of the state vector

The update step refines the estimated state vector from the predicted step using the measured value at the present time to compute an estimate closer to the true value (3.16). The associated error covariance matrix (3.17) is updated using the measurement model.

$$x_k^{(+)} = x_k^{(-)} + K_k v_k \quad 3.16$$

$$P_k^{(+)} = (I - K_k H_k) P_k^{(-)} \quad 3.17$$

where:

K_k is the Kalman gain defined in (3.18)

v_k is the innovation sequence defined in (3.19)

The Kalman gain (3.18) applies a weight to the correction that is applied to the state correction. The gain influences the amount of information the innovation sequence contributes to the final state prediction. It is a function of the uncertainty of the current state estimates and measurement noise.

$$K_k = P_k^{(-)} H_k^T \left(H_k P_k^{(-)} H_k^T + R_k \right)^{-1} \quad 3.18$$

where R_k is the measurement noise covariance

The innovation sequence (3.19) is a difference between the actual and predicted state measurement vector. In the Kalman filter, the innovations are a zero mean Gaussian white noise sequence and can be used to detect outliers, blunders, or biases. The covariance matrix of the innovation sequence is shown in (3.20). Further details regarding innovation-based blunder detection can be found in section 3.2.1.

$$v_k = z_k - H_k x_k^{(-)} \quad 3.19$$

$$C_v = R_k + H_k P_k^{(-)} H_k^T \quad 3.20$$

where C_v is the innovation sequence covariance matrix. Note that the innovation sequence is the difference between the measurement and the prediction, its uncertainty is the sum the measurement uncertainty and the uncertainty of the predicted states mapped into the measurement domain.

The process noise covariance of a system describes how the uncertainties of the state vector increase with time (Petovello, 2003). These uncertainties can be present in both the system and measurement noise. The continuous time spectral density is shown in (3.21).

$$Q_k = \int_{t_k}^{t_{k+1}} \Phi_{k+1,\tau} G(\tau) Q(\tau) G^T(\tau) \Phi_{k+1,\tau}^T d\tau \quad 3.21$$

where:

G is the shaping matrix.

Q is the spectral densities of the noise in the system

A numerical integration approach has been applied in this research using the methods from (Grewal, 2001) to determine the process noise of the system:

$$Q_k \approx \frac{\Delta t}{2} (\Phi_{k,k+1} G_k Q G_k^T \Phi_{k,k+1}^T + G_k Q G_k^T) \quad 3.22$$

The two-step process of predictions and updates is repeated until the algorithm converges. Figure 3.1 illustrates the Kalman filter algorithm.

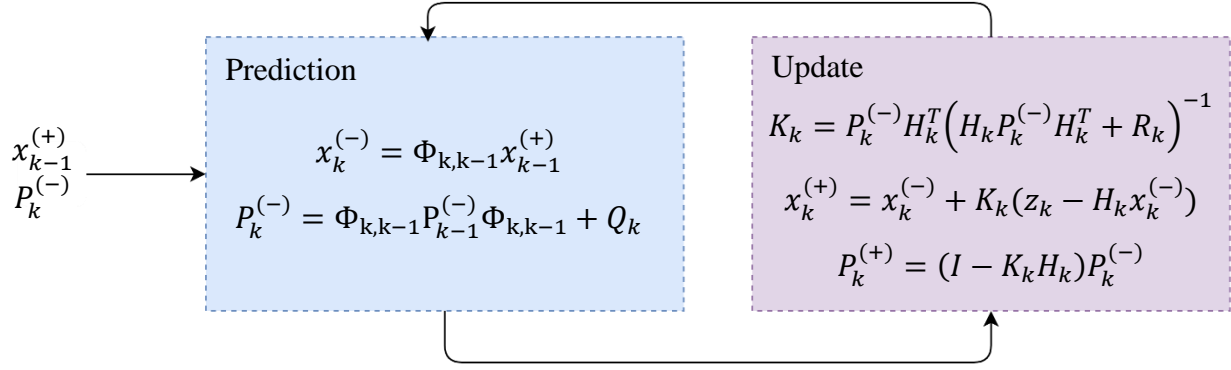


Figure 3.1: Kalman filter schematic

The KF assumes the measurement and system model to be linear. A linear approximation of the measurement model can introduce small errors into the system while a linear system model often requires a closed-loop system. The EKF is used to linearize a non-linear process (Welch & Bishop, 1995), it approximates the Bayes' rule by linearization to estimate the state of a dynamic system. The EKF requires knowledge of process and measurement models and noise to estimate the unknown states; the more accurate the noise model results in higher accuracy of the filter (NGOC et al., 2019). The advantage to the EKF is that estimated non-measured data can be computed. In navigation, the velocity from location measurements can be estimated (Park et al., 2019). GPS observables including pseudorange and range-rates, and low-grade sensor measurements require an EKF because the unknown states are not directly observed.

After linearization from KF to EKF. The innovation sequence and update is simplified (Petovello, 2003) to (3.23) and (3.16) respectively.

$$v_k = z_k - H_k x_k^{(-)} = z_k - H_k(0) = z_k \quad 3.23$$

$$x_k^{(+)} = x_k^{(-)} + K_k \delta z_k \quad 3.24$$

The innovation vector (δz_k) in the EKF is defined the same as the non-linear LS where the predicted states are used to evaluate the measurement function H at the point of expansion.

3.2.1 Innovation Based Quality Control

The GPS measurements collected from a smartphone are prone to outliers or blunders. GPS typically provides long-term stability, but short-term accuracy is limited by the signal quality which may be influenced by errors caused by multipath or atmospheric conditions. In the context of LS estimation, a blunder would affect a single epoch, whereas an error introduced in a KF will impact the state estimates moving forward. Therefore, in low-grade hardware such as that found in a smartphone, outlier detection and rejection of GPS measurements is essential to improve the navigation solution.

As mentioned previously, the measurements in a KF are assumed to follow a zero mean Gaussian distribution and the existence of an outlier will void this assumption. The innovation sequence, which represents the difference between new and estimated parameters, along with its corresponding covariances can provide an indication of abnormal behaviour in the system. A method of determination of whether the predicted innovation follows the assumed mathematical model is via hypothesis testing (Petovello, 2003; P. Teunissen, 1989). Hypothesis testing utilizes the information available about the estimated states to check the quality of the observations. Therefore, testing the validity of the mathematical model through the innovation sequence will provide an assessment of the reliability of the final state estimates. The process of testing begins with a global test, in which the presence of a fault or outlier may be detected, followed by a local test which identifies any individual measurements which may be faulty.

For an EKF with Gaussian distribution and measurement errors, a global test to identify the existence of outliers is completed using the null and alternative hypothesis shown in (3.25).

$$\begin{aligned} H_0: E(v_k^{(-)}) &= 0 \\ H_a: E(v_k^{(-)}) &\neq 0 \end{aligned} \tag{3.25}$$

The test statistic in (3.26) is the sum of squares of the innovations weighted by the measurements and is applied to all innovations together.

$$\begin{aligned}\xi|_{H_0} &= v_k^{(-)} \left(C_{v_k}^{(-)} \right)^{-1} v_k^{(-)} \sim \chi^2(d_k, 0) \\ \xi|_{H_a} &= v_k^{(-)} \left(C_{v_k}^{(-)} \right)^{-1} v_k^{(-)} \sim \chi^2(d_k, \lambda_k^2)\end{aligned}\quad 3.26$$

where d_k is the number of degrees of freedom

If the presence of an outlier is detected in the global test, a local test is then used on each measurement to identify which of the individual measurements are faulty. The test statistic is shown in (3.27) where it is applied to one measurement at a time. If the test fails, the corresponding measurement is identified as an outlier.

$$\xi|_{H_0} = \frac{M_i^T \left(C_{v_k}^{(-)} \right)^{-1} v_k^{(-)}}{\sqrt{M_i^T \left(C_{v_k}^{(-)} \right)^{-1} M_i}} \sim N(0,1) \quad 3.27$$

where M_i is a column vector consisting of $[0 \quad \cdots \quad 0 \quad 1 \quad 0 \quad \cdots \quad 0]$ where 1 is the i^{th} element

3.3 GPS-only Model

An EKF is used in this work for GPS-only positioning estimation using pseudorange measurements. The state error vector consists of 8 unknowns which are defined in (3.28). A constant velocity model was used to model the trajectory of a kayak over time, the state transition is shown in (3.29).

$$\delta x_{k,GPS_{KF}} = [\delta r_{3x1}^e \quad \delta b_r \quad \delta v_{3x1}^e \quad \delta \dot{b}_r] \quad 3.28$$

$$\Phi_{k,k+1} = \begin{bmatrix} I_{4x4} & \Delta t \cdot I_{4x4} \\ 0_{4x4} & I_{4x4} \end{bmatrix} \quad 3.29$$

where:

δr_{3x1}^e is the position error vector in the e -frame (r_x, r_y, r_z)

δv_{3x1}^e is the velocity error vector in the e -frame (v_x, v_y, v_z)

Δt is the prediction time interval

The design matrix (3.30) is constructed as a function of the observation equation (3.28) where n is the number of satellites (GPS pseudoranges and range-rates) available in epoch k , and i is the i^{th} satellite in epoch k .

$$H_{k,GPS} = \begin{bmatrix} H_{P_{nx3}} & 1_{nx1} & 0_{nx3} & 0_{nx1} \\ 0_{nx3} & 0_{nx1} & H_{\dot{P}_{nx3}} & 1_{nx1} \end{bmatrix} \quad 3.30$$

where H_P is the derivative matrices of equations with respect to the state error vector (3.31 - 3.33).

$$\begin{aligned} P_i &= \rho_i + c\delta b_r + \varepsilon_{code} = \rho_i - \rho_i(x_0) \\ \rho_i &= \sqrt{(r_x^R - r_x^S)^2 + (r_y^R - r_y^S)^2 + (r_z^R - r_z^S)^2 + \delta b_r} \end{aligned} \quad 3.31$$

$$H_{P_{nx3}} = \left[\frac{\partial \rho_i}{\partial x^R} \quad \frac{\partial \rho_i}{\partial y^R} \quad \frac{\partial \rho_i}{\partial z^R} \quad \frac{\partial \rho_i}{\partial b_r} \right] \quad 3.32$$

$$\frac{\partial \rho_i}{\partial x^R} = \frac{x_i^S - x_0^R}{\rho_i}, \quad \frac{\partial \rho_i}{\partial y^R} = \frac{y_i^S - y_0^R}{\rho_i}, \quad \frac{\partial \rho_i}{\partial z^R} = \frac{z_i^S - z_0^R}{\rho_i}, \quad \frac{\partial \rho_i}{\partial b_r} = 1 \quad 3.33$$

where x_0 is a point of linearization

The Doppler shift between a receiver and satellite and corresponding pseudo-range rate observation equations is shown in (3.34) and (3.35) respectively.

$$D^n = \frac{\left((v^S - v^R) \cdot \left(\frac{r^S - r^R}{\rho_i} \right) \right) Frequency_{L1}}{c} \quad 3.34$$

$$\dot{\rho} = -\frac{D^n c}{Frequency_{L1}} = \left(\frac{r^S - r^R}{\rho_i} \right) \cdot (v^S - v^R) + \delta \dot{b}_r \quad 3.35$$

where:

D^n is the Doppler shift of the n th satellite

The corresponding measurement models are shown below.

$$H_{\dot{\rho}_{nx3}} = \begin{bmatrix} \frac{\partial \dot{\rho}_i}{\partial v_x^R} & \frac{\partial \dot{\rho}_i}{\partial v_y^R} & \frac{\partial \dot{\rho}_i}{\partial v_z^R} & \frac{\partial \dot{\rho}_i}{\partial \delta \dot{b}_r} \end{bmatrix} \quad 3.36$$

$$\frac{\partial \dot{\rho}_i}{\partial v_x^R} = \frac{x_i^S - x_0^R}{\rho_i}, \quad \frac{\partial \dot{\rho}_i}{\partial v_y^R} = \frac{y_i^S - y_0^R}{\rho_i}, \quad \frac{\partial \dot{\rho}_i}{\partial v_z^R} = \frac{z_i^S - z_0^R}{\rho_i}, \quad \frac{\partial \dot{\rho}_i}{\partial \delta \dot{b}_r} = 1 \quad 3.37$$

3.4 GPS/INS Integration Types

This section describes the principles of GPS/INS integration and the corresponding system models used in this work. GPS and INS are complementary technologies to each other when combined (Groves, 2007). GPS can provide accurate, time invariant solutions dependent upon satellite availability. Conversely, INSs are wholly self contained and do not rely on external sources to provide a solution; they often have a high data rate and can provide data continuously to interpolate solutions between GPS updates or outages. An INS can also provide the attitude information of the system in addition to position and velocity, which a single GPS receiver cannot. However, INS errors in a low-grade platform increase proportional to time causing the solution performance to degrade significantly. Therefore, INS requires an external aiding system like GPS to correct the solution periodically.

The three most common forms of GPS/INS integration are loosely, tightly, and ultra-tightly/deeply coupled. These three approaches vary with performance and cost of the system.

The loosely coupled approach merges GPS position and velocity information with INS information. The tightly coupled approach integrates the raw measurements of pseudorange and pseudorange rates from the GPS with the inertial data.

In both implementations, corrections from the error-state KF may be applied in an open- or close-loop configuration (Groves, 2007). In an open-loop architecture, the INS solution is independent from the GPS/INS integration KF and the INS errors remain uncorrelated. This design corrects the solutions states at each filter integration stage; however, these corrections are not cycled back to the INS solution. In this configuration, the raw INS can be used to monitor the integrity of the KF, though the errors in the INS will grow over time due to unconstrained drift errors.

A closed-loop configuration feeds the inertial measurement errors estimated from the GPS/INS KF back to the INS solution. This is advantageous with low-grade IMUs to provide a more reliable raw INS solution with corrections applied for the mechanization process. Due to this reasoning, a close-loop configuration is implemented in this thesis.

The ultra-tightly coupled GPS/INS integration estimates the navigation states, IMU error states, and tracks the GPS signal navigation states in a single integration algorithm (Babu & Wang, 2004; Gao & Lachapelle, 2008; Lashley & Bevly, 2013). The navigation filter closes the carrier-tracking loop, unlike the loosely and tightly coupled algorithms, thus allowing the carrier-tracking loop bandwidth to be reduced which improves the quality of raw measurements and resistance to jamming. A low-cost MEMS-based INS may produce low accuracy data that contains blunders, causing the INS aiding information to be unreliable. It is worth noting that an ultra-tightly coupled GPS/INS integration system is an extension of the tightly coupled approach and is complex and computationally heavy, therefore it is not used in this project.

3.4.1 Loosely Coupled Integration

A loosely coupled GPS/INS integration algorithm, also known as a ‘*decentralized*’ approach, uses separate modules to estimate the GPS, INS, and GPS/INS integration solutions. The integration scheme is shown in Figure 3.2 below.

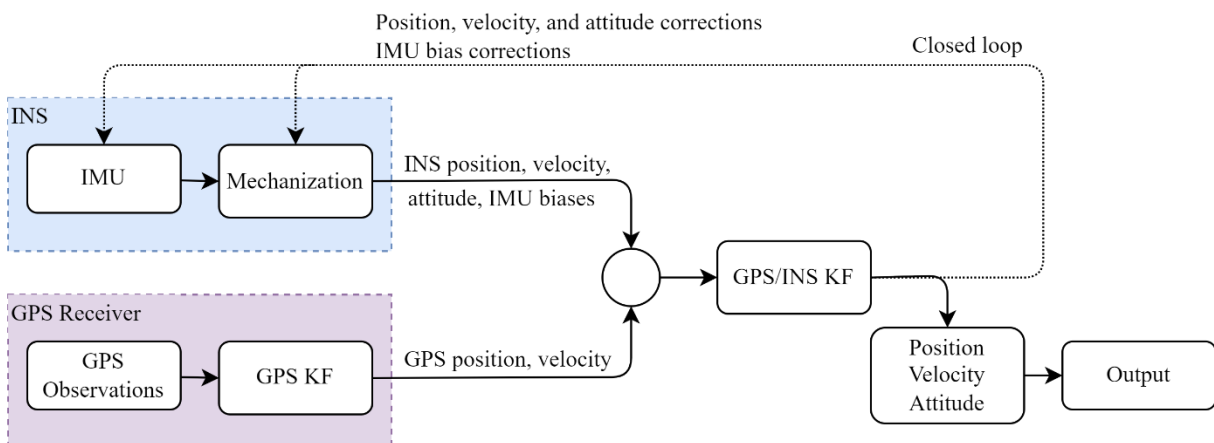


Figure 3.2: LC integration schematic

In the GPS module, the raw GPS measurements recorded by the smartphone are processed pseudorange and Doppler measurements. A KF algorithm is then applied to estimate the position

and velocity solutions using single point positioning as explained in section 3.3. The INS module derives the inertial solution by applying the mechanization equations (equation 2.20) to the accelerometer and gyroscope measurements. The GPS position and velocity estimates are then integrated with the INS derived position and velocity estimates in the GPS/INS KF module to output a final solution. In the event of a GPS outage or between GPS updates, the INS will continue to provide an output solution for each measurement recorded by the IMU.

3.4.2 Tightly Coupled Integration

A tightly coupled GPS/INS filter or ‘centralized’ filter is shown below in Figure 3.3.

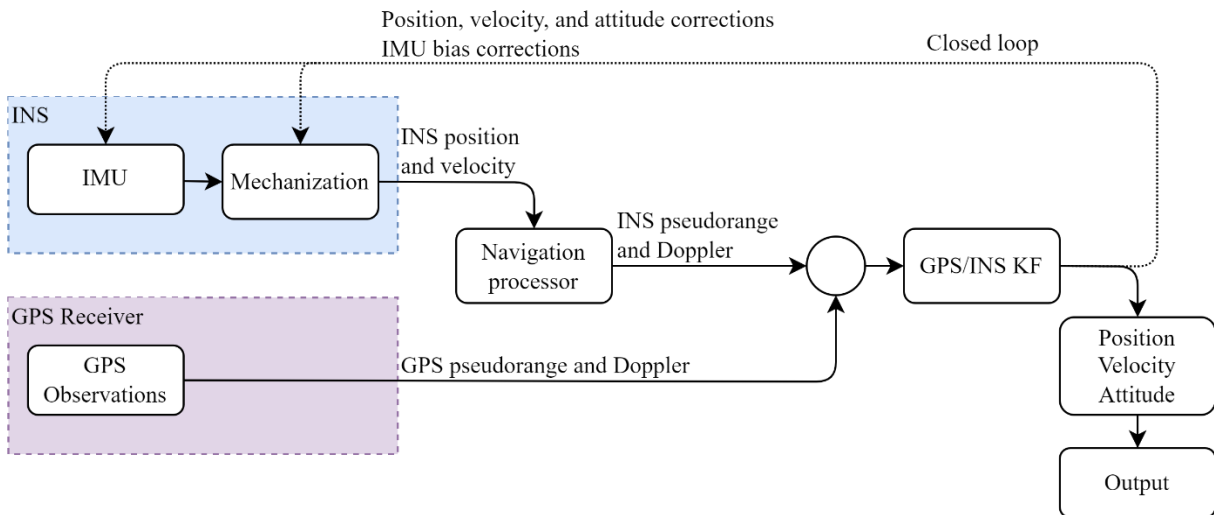


Figure 3.3: TC integration schematic

In this type of integration, the raw GPS observables of pseudorange (ρ) and pseudorange-rate ($\dot{\rho}$) measurements are combined with the INS navigation parameters in one central KF (Groves, 2007; Lachapelle et al., 2018). It is called a centralized integration because of the use of a single common master filter. In the loosely coupled system, a separate filter is used to calculate the GPS position and velocity which introduces a correlation problem. The tightly coupled GPS/INS system eliminates the issue of correlated measurements and can provide a GPS update even if the number of visible satellites drops below the minimum threshold required for an adequate stand-alone GPS solution.

3.4.3 Loosely Coupled vs Tightly Coupled

The main difference between the loose and tight GPS INS implementations is the measurements used in each filter. In LC, the processed GPS solution of position and velocity are combined with the INS. In TC, the raw GPS pseudoranges and pseudorange rates are fused with INS navigation parameters. This results in the LC implementation having two separate filters (GPS and GPS/INS) and the TC implementation having one centralized filter (GPS/INS).

The use of two separate filters in a LC architecture introduce two characteristics that can impair system performance. The first is the total process noise in the navigation solution increases by implementing separate filters for GPS and GPS/INS (Petovello, 2003). The second characteristic originates from using the time correlated outputs from the GPS KF within the GPS/INS KF, which violates the underlying assumption of uncorrelated measurement noise in a KF (Noureddin et al., 2013). However, due to the stand-alone modules for GPS and INS, the integration filter does not require as many states as in the TC solution. A LC implementation is therefore more robust than a TC. If one system fails than either a GPS or INS solution can be relied upon whereas in the TC implementation both systems must be operational to provide a solution. However, LC is unable to provide a GPS update when the number of visible satellites drops below the minimum number required for an adequate GPS solution. This can contribute to INS errors rapidly increasing over time without periodic GPS corrections provided in low-grade INS, thus decreasing the system performance over a short time. An advantage of a LC filter is that it can be used with systems or hardware that provide GPS solutions, rather than raw GPS measurements, therefore increasing the applications of GPS/INS navigation. This filter is simple to implement and provides multiple positioning solutions, from the GPS, INS, and GPS/INS integrated solution.

In comparison, a TC implementation is advantageous in areas where the number of visible satellites drop due to satellite line of sight obstructions that can be caused by tree canopies, bridges, and/or river canyons. The measurement update can be performed with only two satellites unlike the LC filter which requires at least four satellites for a measurement update. However, tight coupling often requires the software in a GPS receiver to output the raw observables, which may not be available on mass-market devices or receivers. This makes the filter more complex to implement as it involves processing raw GPS data.

3.5 Loosely Coupled Model

A 15-state discrete time EKF implementation was used in this work to process the GPS and INS measurements in a loosely coupled closed loop configuration. The state error vector is shown in (3.38) which was used to show how the state evolves with time in the system model.

$$\delta x_{k,GPSKF} = [\delta r_{3x1}^l \quad \delta v_{3x1}^l \quad \delta \varepsilon_{3x1}^l \quad \delta \omega_{3x1} \quad \delta f_{3x1}] \quad 3.38$$

where:

$\delta \varepsilon^l$ is the attitude error vector (p, r, ψ_y)

The l -frame discrete transition matrix for GPS/INS integration is modelled as:

$$\Phi_{k,k+1} = \begin{bmatrix} I_{3x3} & F_r & 0_{3x3} & 0_{3x3} & 0_{3x3} \\ 0_{3x3} & I_{3x3} & F_v & 0_{3x3} & R_b^l \Delta t \\ 0_{3x3} & F_\varepsilon & I_{3x3} & R_b^l \Delta t & 0_{3x3} \\ 0_{3x3} & 0_{3x3} & 0_{3x3} & I_{3x3} + D_\omega \Delta t & 0_{3x3} \\ 0_{3x3} & 0_{3x3} & 0_{3x3} & 0_{3x3} & I_{3x3} + D_f \Delta t \end{bmatrix} \quad 3.39$$

where:

F_r, F_v, F_ε are the skew-symmetric matrix of the position, velocity, and attitude errors respectively

D_ω, D_f are the diagonal matrices of the time rate of change of the gyroscope and accelerometer errors respectively

The design matrix (3.41) is created from the measurement vector (3.40) which consists of a difference between positions and velocities measured from the GPS and INS.

$$\delta z = \begin{bmatrix} r_{INS}^l - r_{GPS}^l \\ v_{INS}^l - v_{GPS}^l \end{bmatrix} \quad 3.40$$

$$H = \begin{bmatrix} I_{3x3} & 0_{3x3} & 0_{3x9} \\ 0_{3x3} & I_{3x3} & 0_{3x9} \end{bmatrix} \quad 3.41$$

The process noise covariance (Q_k), used to account for uncertainty in the system model, is obtained using numerical integration (Petovello, 2003).

$$Q_k = (\Phi_{k,k+1} G_k q_c G_k^T \Phi_{k,k+1} + G_k Q_c G_k^T) \frac{\Delta t}{2} \quad 3.42$$

where:

q_c is the power spectral density of estimated state

G_k is a coefficient matrix that shapes white noise input.

The navigation parameter errors of the position, velocity, and attitude of the INS solution following the integrated KF are defined below.

$$\begin{aligned} \hat{r}^l &= r^l - \delta \hat{r}^l \\ \hat{v}^l &= v^l - \delta \hat{v}^l \\ \hat{R}_b^l &= (I - \Omega_{\varepsilon^l}) R_b^l \end{aligned} \quad 3.43$$

where:

Ω_{ε^l} is the skew-symmetric matrix of the attitude errors ($\varepsilon_p, \varepsilon_r, \varepsilon_{\psi_y}$)

variables with the \wedge are estimated

3.6 Tightly Coupled Model

The TC configuration adopted in this thesis is a closed loop centralized approach in which the GPS raw pseudoranges and Doppler measurements are processed with the INS navigation parameters in one KF. The details of the corresponding system and measurement models are presented below.

The state error vector is an extended version of (3.38) to account for the GPS states as well. The TC model is the same as the LC model combined with the GPS-only model. In the LC model, the clock bias and drift are estimated in the GPS-only KF whereas the TC model augments these states in one central filter. The states of the TC model are shown as:

$$\delta x_{k,GPS_{KF}} = [\delta r_{3x1}^l \quad \delta v_{3x1}^l \quad \delta \varepsilon_{3x1}^l \quad \delta \omega_{b,3x1} \quad \delta f_{b,3x1} \quad \delta b_r \quad \delta \dot{b}_r] \quad 3.44$$

The measurement model is a difference between the INS derived observations and those measured from the GPS.

$$\delta z = \begin{bmatrix} \rho_{INS} - \rho_{GPS} \\ \dot{\rho}_{INS} - \dot{\rho}_{GPS} \end{bmatrix} \quad 3.45$$

By incorporating the extra GPS clock states and the measurement model of pseudorange and pseudorange rates, the transition matrix (3.46) and design matrix (3.47) become:

$$\Phi_{k,k+1} = \begin{bmatrix} I_{3x3} & F_r & 0_{3x3} & 0_{3x3} & 0_{3x3} & 0_{3x3} & 0_{3x3} \\ 0_{3x3} & I_{3x3} & F_v & 0_{3x3} & R_b^l \Delta t & 0_{3x3} & 0_{3x3} \\ 0_{3x3} & F_\varepsilon & I_{3x3} & R_b^l \Delta t & 0_{3x3} & 0_{3x3} & 0_{3x3} \\ 0_{3x3} & 0_{3x3} & 0_{3x3} & I_{3x3} + D_\omega \Delta t & 0_{3x3} & 0_{3x3} & 0_{3x3} \\ 0_{3x3} & 0_{3x3} & 0_{3x3} & 0_{3x3} & I_{3x3} + D_f \Delta t & 0_{3x3} & 0_{3x3} \\ 0_{1x3} & 0_{1x3} & 0_{1x3} & 0_{1x3} & 0_{1x3} & 1 & \Delta t \\ 0_{1x3} & 0_{1x3} & 0_{1x3} & 0_{1x3} & 0_{1x3} & 0_{1x3} & 1 \end{bmatrix} \quad 3.46$$

$$H = \begin{bmatrix} H_{nx3} T_{3x3} & 0_{nx3} & 0_{nx9} & -1_{nx1} & 0_{nx1} \\ 0_{nx3} & H_{nx3} R_l^e & 0_{nx9} & 0_{nx1} & -1_{nx1} \end{bmatrix} \quad 3.47$$

where:

T_{3x3} is the transformation matrix to transform the position errors from the l-frame to the e-frame (3.48 - 3.49)

H_{nx3} the design matrix derived from the INS derived pseudorange and pseudorange rates (3.50 - 3.51)

The following equation defines the relationship between the l -frame and e -frame.

$$\begin{bmatrix} x^e \\ y^e \\ z^e \end{bmatrix} = \begin{bmatrix} (R_N + h) \cos(\varphi) \cos(\lambda) \\ (R_N + h) \cos(\varphi) \sin(\lambda) \\ (R_N(1 - e^2) + h) \sin(\varphi) \end{bmatrix} \quad 3.48$$

where:

R_N is the Earth's prime vertical radius of curvature

e is the Earth's eccentricity

By linearizing (3.31), the transformation matrix is found:

$$T_{3x3} = \begin{bmatrix} -(R_N + h) \sin(\varphi) \cos(\lambda) & -(R_N + h) \cos(\varphi) \sin(\lambda) & \cos(\varphi) \cos(\lambda) \\ -(R_N + h) \sin(\varphi) \sin(\lambda) & -(R_N + h) \cos(\varphi) \cos(\lambda) & \cos(\varphi) \sin(\lambda) \\ (R_N(1 - e^2) + h) \cos(\varphi) & 0 & \sin(\varphi) \end{bmatrix} \quad 3.49$$

Finally, the line-of-sight unit vectors from the satellites to the receiver for the INS are defined as:

$$H_{nx3} = [h_{x,INS_{nx1}} \quad h_{y,INS_{nx1}} \quad h_{z,INS_{nx1}}] \quad 3.50$$

$$\begin{aligned} h_{x,INS_{nx1}} &= \frac{x_{INS} - x_n}{\sqrt{(x_{INS} - x_n)^2 + (y_{INS} - y_n)^2 + (z_{INS} - z_n)^2}} \\ h_{y,INS_{nx1}} &= \frac{y_{INS} - y_n}{\sqrt{(x_{INS} - x_n)^2 + (y_{INS} - y_n)^2 + (z_{INS} - z_n)^2}} \\ h_{z,INS_{nx1}} &= \frac{z_{INS} - z_n}{\sqrt{(x_{INS} - x_n)^2 + (y_{INS} - y_n)^2 + (z_{INS} - z_n)^2}} \end{aligned} \quad 3.51$$

The methods of estimation that are described in this chapter will be evaluated with real-world kayak data. The data collection and processing procedures, and corresponding results are presented in the next chapter.

Chapter 4: Data Collection and Results

To validate the performance of the GPS and GPS/INS solutions described in the previous chapter, real-world data was collected, processed, and analyzed. This chapter details the conducted experiments including hardware setup, data collection and selection, and software development. Then the navigation solution of GPS-only and loosely and tightly coupled GPS/INS results are presented.

4.1 Equipment Setup and Data Collection

The hardware used for data collection consists of two main components: a smartphone data collector and a reference solution. The smartphone used in this project is a Google Pixel 4 and was attached to the bow of the kayak in a waterproof case. The reference solution consisted of three commercial grade GNSS receivers; two of the receivers were mounted to the bow and the stern of the kayak respectively, and the third receiver was used as a base receiver on shore. Custom stands were constructed to mount the smartphone and reference solution receivers to the bow and stern kayak handles rigidly.

This hardware setup used on a kayak is shown in Figure 4.1. The type of kayak chosen for this project is a freestyle kayak. A freestyle kayak is a short kayak (~1-2 meters length) that is optimized for quick maneuverability and control. The short kayak will amplify a kayaker's paddle stroke and motions as they traverse through the water; this motion is captured by the INS attitude angles. In comparison a sea kayak (~4-5 metres) will not move side-to-side with each paddle stroke as much as a freestyle kayak does due to the characteristics of the kayak model.



Figure 4.1: Equipment setup

The Google Pixel 4 smartphone contains a 3-axis accelerometer, 3-axis gyroscope, and a GNSS receiver. Raw GPS and sensor measurements were logged to the phone using Google application GNSSLogger (van Diggelen & Khider, 2016/2018). This application records all raw data with time stamps from the sensors which allows data from different sensors to be synchronized with respect to a time tag for implementing various GPS/INS algorithms. GNSSLogger records the data from the Google Pixel 4 at a fixed rate of 1 Hz and 100 Hz for the raw GPS and IMU measurements respectively. A full description of the measurements recorded by GNSSLogger are presented in Appendix A. The recorded observations were then processed using developed software which is detailed in section 4.3.

To assess and validate the results from the smartphone GPS/INS solution, a GNSS reference trajectory was also collected using a series of Topcon HiPer SR site receivers. Two receivers, referred to as rovers, were mounted on the bow and stern of the kayak as shown in Figure 4.1. Though these receivers were selected because they are waterproof, they were raised slightly higher than the kayak to protect the hardware from water damage and preserve a reasonably good satellite signal strength by evading signal outages caused by water pouring over the receivers. The lever arm offsets of the receivers were noted, and corrections applied in post-processing to account for the offset. The purpose of using dual receivers on the kayak was to capture the azimuth variation of each paddle stroke and provide additional redundancy in data verification. A third Topcon

receiver was set up as a base station on shore to apply a double-differencing kinematic solution for the reference trajectory. The collected reference trajectory measurements were processed with an open source programming package called RTKLIB (*RTKLIB: An Open Source Program Package for GNSS Positioning*, n.d.). The sampling rate for these receivers was set to 10 Hz so that the reference trajectory had a time resolution an order of magnitude higher than the paddling motion that was being captured.

The data collection procedure for each run is split into two main parts: static and dynamic data. Static data is used to complete the misalignment correction as detailed in section 2.9 for every run completed. To recap here, the axis of the smartphone device frame with respect to the kayak/body frame could vary slightly with each data collection run due to the attachment and detachment of the phone from the kayak. This will result in a misalignment error between the device frame and the body frame. To complete the misalignment correction, stationary IMU data was collected by sitting in the kayak on flat, calm water. Theoretically, any movement of the paddler or wind or water would contribute to an error in the stationary alignment, the longer the duration of stationary data the better.

Dynamic data was then collected immediately following the static alignment process on each separate run. The data for this project was collected on two rivers: the North Saskatchewan River and the ‘Racecourse’ section on the Kananaskis River. These river sections contain flat water and continuous rapids respectively. The North Saskatchewan River provides the most optimal open-sky GPS satellite visibility conditions paired with calm water that enabled the IMU to capture primarily paddler and kayak movement with minimal water or rapid noise. Conversely, the Kananaskis River Racecourse consists of multiple, continuous rapids and drops, and provides a more GPS-challenging environment with canyon walls and trees as well as cables crossing over the river. These two river environments are illustrated in Figure 4.2.



Figure 4.2: North Saskatchewan and Kananaskis Rivers

4.2 Reference Trajectory Results and Data Selection

Prior to the experimental analysis of the GPS/INS solution performance, an investigation of the reference solution was completed to obtain a reliable ‘truth’ with which to compare the smartphone solution with. Therefore, the quality of the solution obtained by the Topcon HiPer SR receivers is assessed, and data was selected within the periods of times where this solution is deemed reliable. The relevant specifications for Topcon HiPer SR site receivers are shown in Table 2 (*Topcon TotalCare :: Specifications*, n.d.).

Table 2: Topcon HiPer SR specifications

	Positioning Accuracy	
	Horizontal	Vertical
RTK	10 mm + 1.0 ppm	15 mm + 1.0 ppm
Fast Static (L1)	3 mm + 0.8 ppm	4 mm + 1.0 ppm
Fast Static (L1 + L2)	3 mm + 0.5 ppm	5 mm + 0.5 ppm
Differential GPS	0.4 m	0.6 m
Tracking		
Signals	GPS L1, L2, L2C GLONASS L1, L2, L2C SBAS QZSS L1, L2C	

The selection of data used in this project is dependant on the reliability of the reference solution for that period of time. A RTK positioning mode was used for the reference solution with dual-frequency signals and GPS+GLONASS constellations. A kinematic position produces an absolute position of the rover by differential positioning between the base and rover receiver (Parajuli, 2020). Figure 4.3 displays the fixed and float solutions of the bow-mounted reference trajectory collected from a run on the North Saskatchewan River. This solution shows a float solution happening most notably in the first quarter of the run; this occurred because the kayak and receivers passed underneath a bridge over the river thereby briefly obstructing the continuous satellite signals.

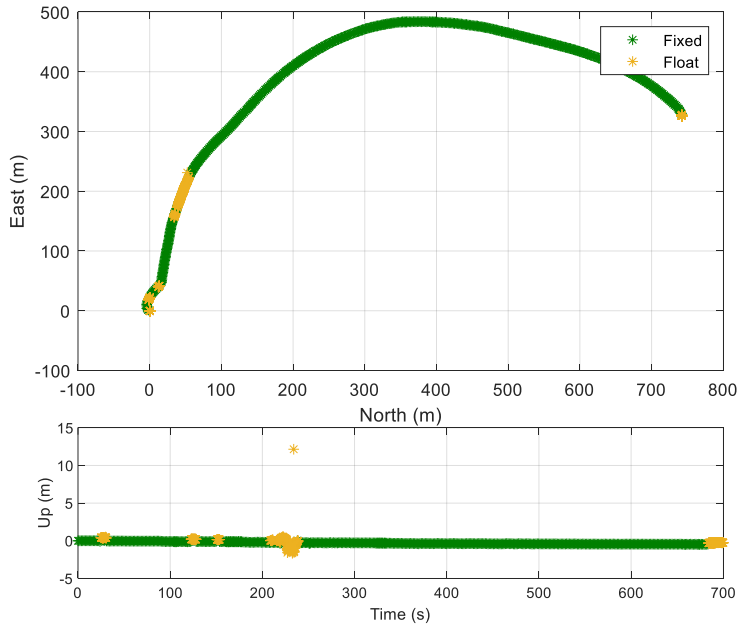


Figure 4.3: Reference trajectory fixed and float solutions

The dual receivers mounted on the bow and stern also provide outlier and blunder detection by evaluating the baseline length between the dual receivers. As shown in Figure 4.4, the baseline length between the receivers is ~ 1.29 metres and a large deviation from this length will indicate an outlier or blunder in the reference data.

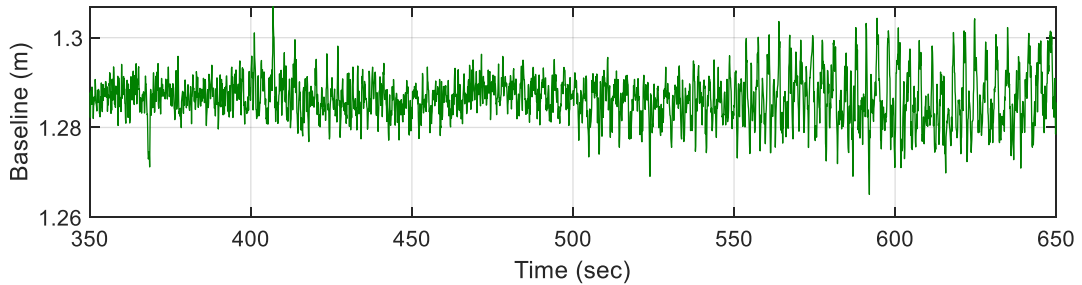


Figure 4.4: Reference trajectory baseline length

Therefore, periods of time with a float reference solution and a baseline length outlier are deemed unreliable due to the degradation of the precision. Consequently, these areas of data were not selected for use in the final datasets.

Figure 4.5 and Figure 4.6 illustrates the standard deviations of the fixed reference solution and by extension the expected precision for the same dataset shown in Figure 4.3. As can be seen here, the precision of the reference solution for this dataset is ~3 mm, 5 mm, and 8 mm for the east, north and up directions respectively.

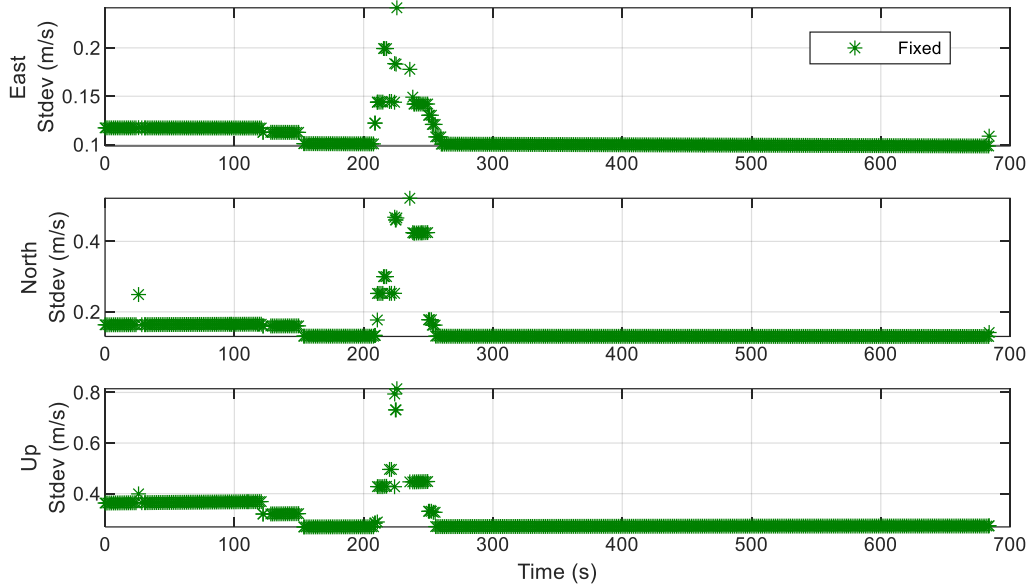


Figure 4.5: Reference trajectory velocity standard deviations

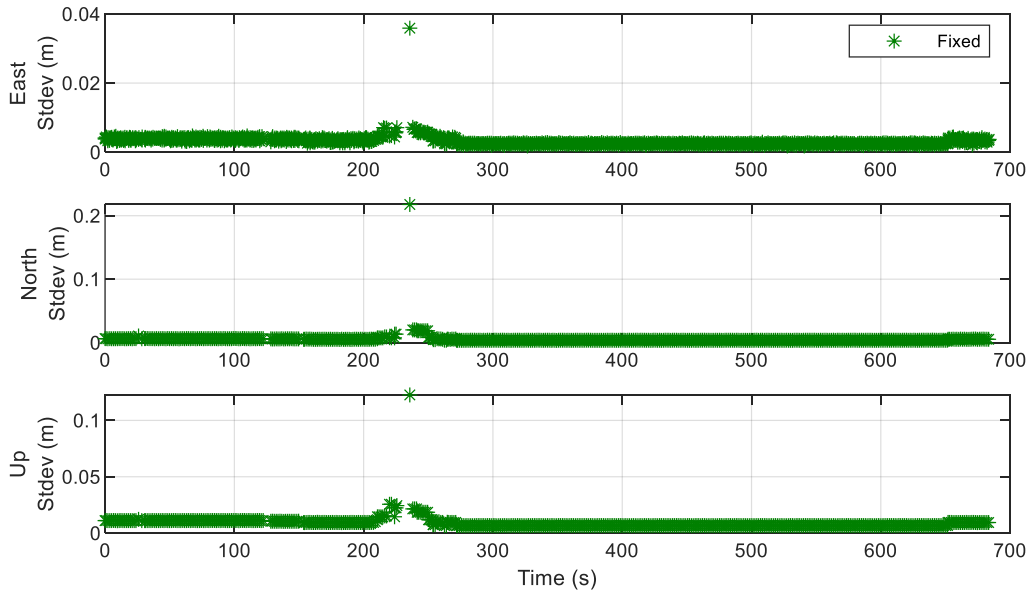


Figure 4.6: Reference trajectory position standard deviations

The bow- and stern-mounted receivers were used in conjunction to provide a reference position, velocity, and azimuth solution. By acquiring positions for both the bow and stern of the kayak at the same time, an azimuth can be calculated to illustrate the variation in each paddle stroke in calm waters. An example of the azimuth solution collected in calm waters is shown in Figure 4.7, this is a subset of the data presented above. Each peak in the azimuth represents the beginning and end of a paddle stroke forming a sinusoidal or cyclic pattern.

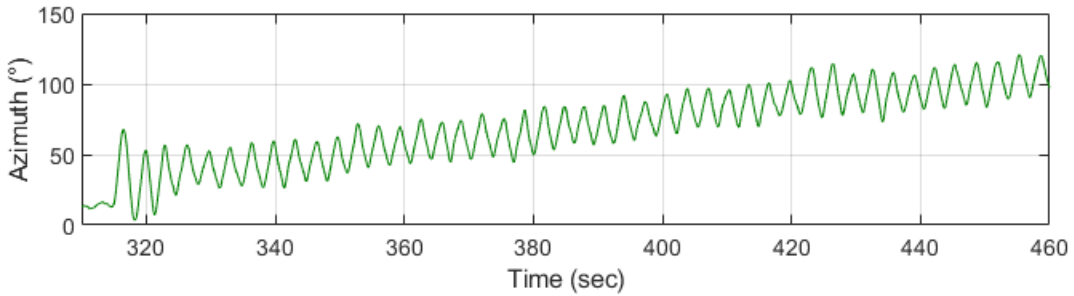


Figure 4.7: Reference trajectory azimuth

The precision of the azimuth solution is calculated in (4.1) as a function of the bow and stern variances.

$$\sigma_{\Psi_A}(\text{reference}) = \tan^{-1} \left(\frac{\sqrt{\sigma_{bow}^2 + \sigma_{stern}^2}}{\text{baseline length}} \right) \quad 4.1$$

The precision of the reference azimuth solution is found to be $\sim 0.1^\circ$. From these results, it is concluded that a dual antenna RTK solution from Topcon receivers provides a precise enough solution for a reference trajectory.

Meeting this criteria, four total datasets with a duration of 150 seconds from 4 different runs were selected to be used in this project; 3 were collected on the flat waters of the North Saskatchewan River and 1 was collected on the Kananaskis River. These are summarized in Table 3 with the overall trajectories shown in Figure 4.8 where datasets 1, 2, and 3 are referenced to the same initial coordinate and dataset 4 begins at a different coordinate.

Table 3: Datasets and descriptions

Dataset	River	Water Conditions	Conditions
1 – 2	North Saskatchewan	Flat, calm	Open skies, continuous paddling
3	North Saskatchewan	Flat, calm	Open skies, intermittent paddling
4	Kananaskis	Continuous rapids, drops	Tall canyons, wires overhead, tree cover

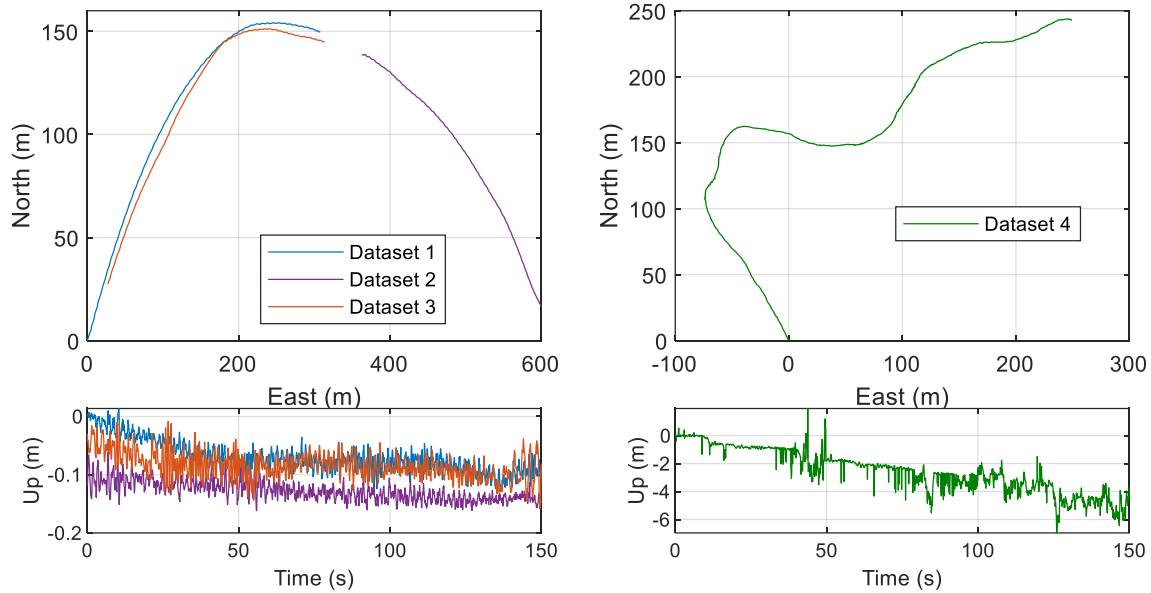


Figure 4.8: Trajectory of each dataset

Figure 4.9 demonstrates the difference in the number of satellites tracked between the 4 datasets from the reference trajectory. It is shown that in the optimal environment with clear line of sight to satellites, 11 satellites are continually tracked in dataset 1-3, whereas dataset 4 has discontinuous tracking of only a few satellites.

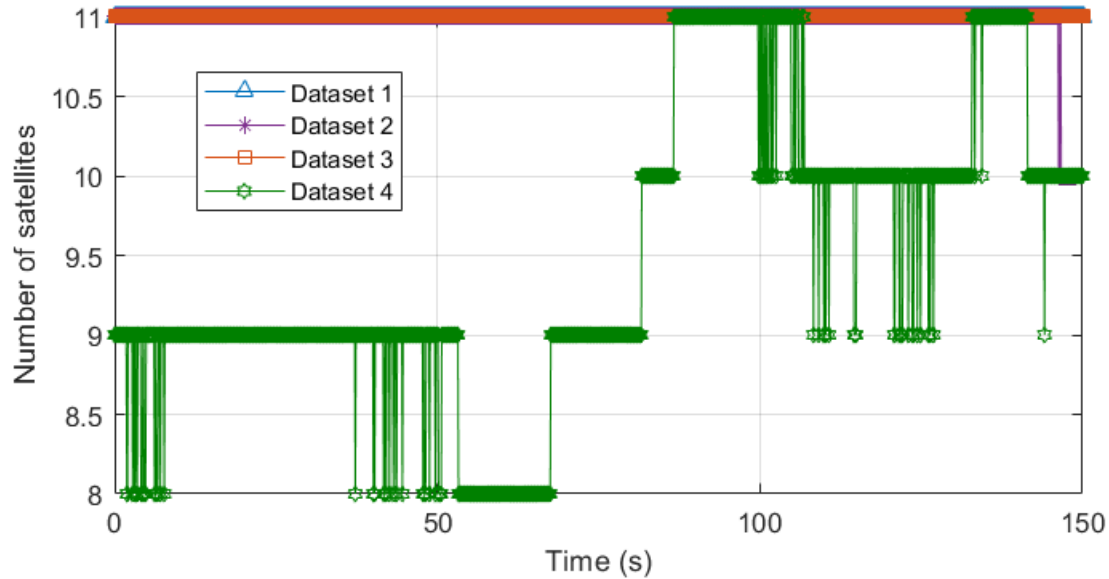


Figure 4.9: Reference solution number of satellites for each dataset

The standard deviations of the velocity and position reference solutions for datasets 1-3 are illustrated in Figure 4.10 and Figure 4.11 respectively. Dataset 4 was excluded from these plots because the precision of this solution is significantly lower than the other 3 datasets. Table 4 summarizes the overall standard deviations of all datasets.

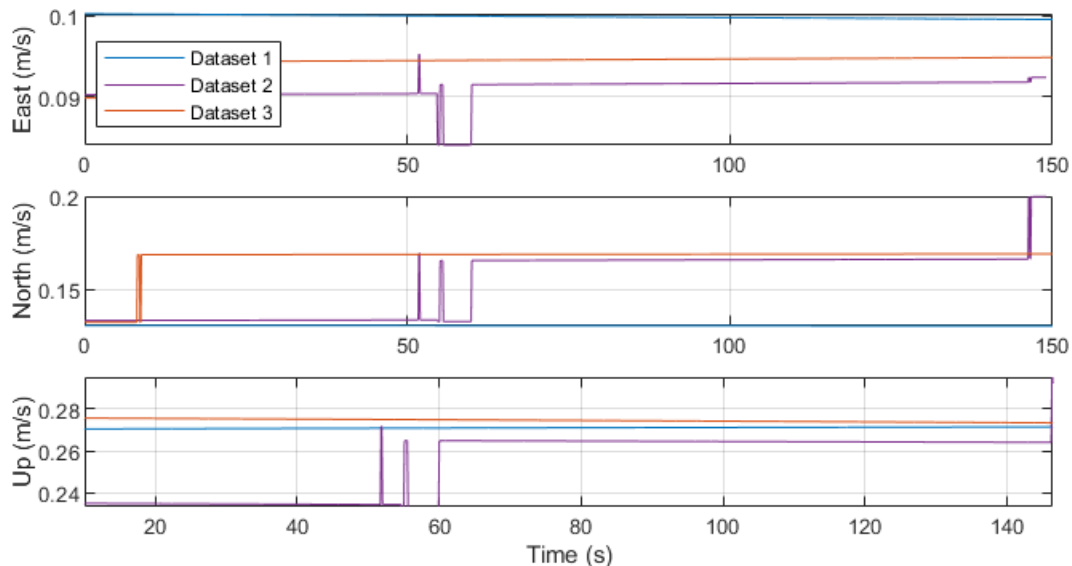


Figure 4.10: Reference velocity standard deviations of datasets 1-3

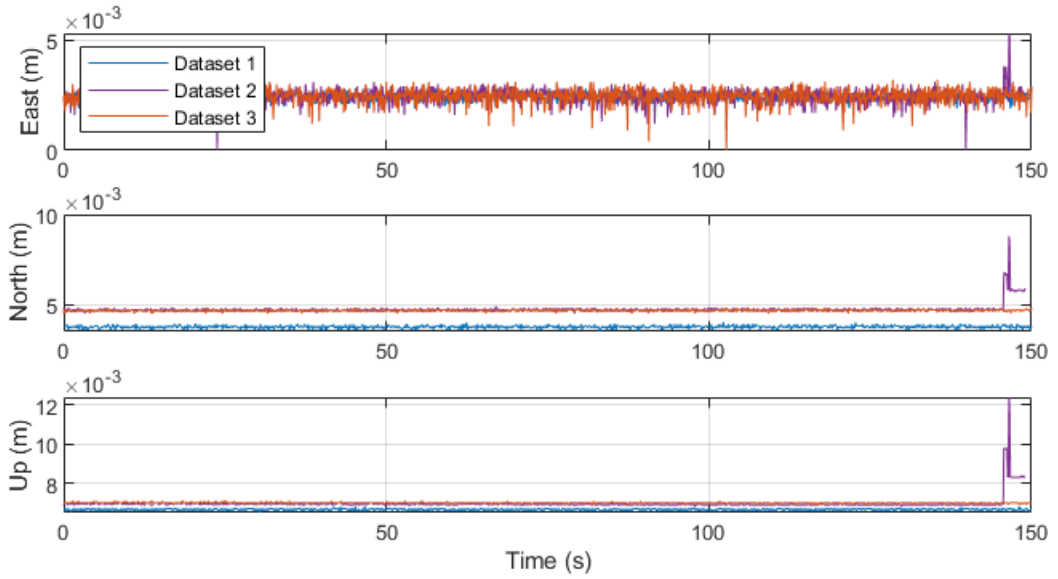


Figure 4.11: Reference velocity standard deviations of datasets 1-3

Table 4: Average standard deviations of reference trajectory for each dataset

Dataset	Position Standard Deviation (m)			Velocity Standard Deviation (m/s)		
	East	North	Up	East	North	Up
1	0.002	0.004	0.007	0.100	0.131	0.271
2	0.002	0.005	0.007	0.091	0.153	0.253
3	0.002	0.005	0.007	0.094	0.167	0.272
4	0.132	0.164	0.596	0.130	0.149	0.500

The position standard deviations for datasets 1-3 is millimeter-level for both horizontal and vertical directions, and dataset 4 is decimeter-level precisions. The poorer solution for dataset 4 is expected due to the dynamic nature of the water and receivers on the kayak in addition to a more GNSS-challenged environment than datasets 1-3 as shown but the number of satellites tracked during the run.

4.3 Software Development

The software developed for data processing in this project was developed in a MATLAB environment. It consists of 4 main units: a data-reader module, a GPS processing module, an INS module, and a GPS/INS integration module.

The raw sensor data collected with GNSSLogger was processed with an open-source software developed by Google, GPS Measurement Tools (van Diggelen & Khider, 2016/2018). This software package reads GNSS data from GNSSLogger, computes and visualizes pseudoranges, and views and analyzes carrier phase data if available from the smartphone. It was further modified and extended in this project to read IMU data as well.

The GPS module is responsible for processing the raw GPS measurements and computing a single point positioning solution with both the LS and KF algorithms. Satellite ephemeris data for this module was retrieved from NASA's archive of Space Geodesy (International GNSS Service (IGS), 1992).

The INS processing module implements the mechanization procedure as outlined in section 2.8. Finally, the GPS/INS integration module was designed to implement a LC and TC algorithm in a closed-loop architecture. This software has the ability to simulate GPS outages and implement different filter configurations to effectively compare the results from each instance. The results of the GPS-only, LC, and TC configurations are discussed in the following sections.

4.4 GPS-only Solution

The single point positioning GPS results from an EKF are presented in this section to demonstrate the accuracy of the GPS-only solution throughout the datasets. The results are compared to the reference solution which is of higher accuracy than the smartphone solution. Only periods of data where the reference solution was deemed reliable were used in this thesis, therefore, the difference of results is most likely attributed to errors in the smartphone solution. The absolute accuracy of the reference solution presented here is only as good as the results described in section 4.2.

Figure 4.12 shows the position and velocity errors of dataset 1 in the across, along, and up direction respectively. The position errors in the across and along are within 5 metres of error from the

reference and the up-direction errors drift significantly to a total of a 10-meter error from initialization. The horizontal and vertical standard deviations are 1.441 and 4.419 metres respectively for position, and 0.208 and 0.253 m/s for velocity. The difference between the horizontal and vertical errors can be contributed to the satellite geometry because the intersection angles for a horizontal solution are more optimal than those for the vertical solution.

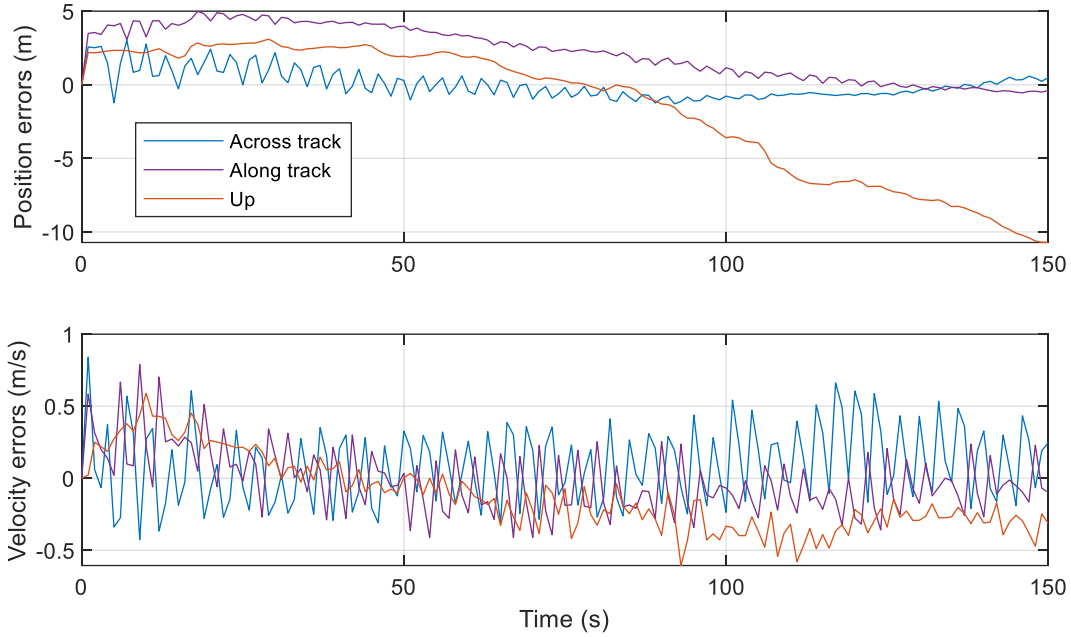


Figure 4.12: Dataset 1 GPS position and velocity errors

The number of satellites tracked, and the root mean square error (RMSE) of the solutions for all datasets are summarized in Figure 4.13 and Table 5 respectively. Datasets 1, 2, and 3 consistently track 7 or 8 satellites throughout the duration of the run, while dataset 4 discontinuously tracks a few satellites.

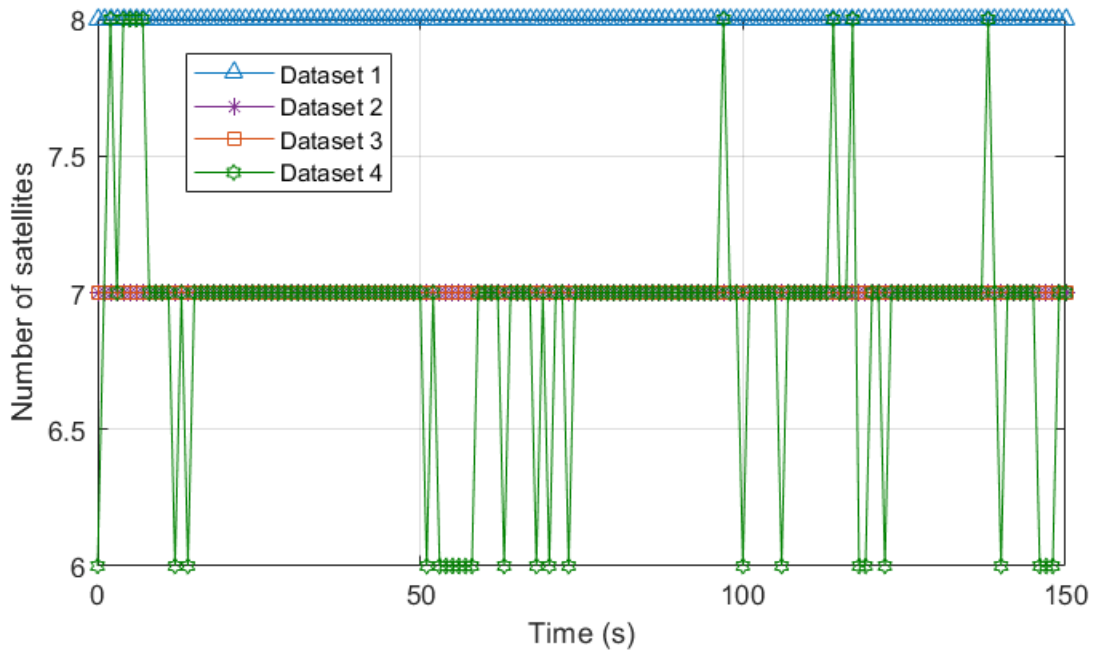


Figure 4.13: Number of satellites for each dataset

Table 5: RMSE of GPS-only EKF solution errors

	RMSE	Dataset 1	Dataset 2	Dataset 3	Dataset 4
Position (m)	Across	0.956	1.031	0.719	2.376
	Along	2.844	0.780	0.953	2.419
	Up	4.682	1.726	6.618	21.477
	3D	5.561	2.156	6.725	21.743
Velocity (m/s)	Across	0.277	0.270	0.153	0.969
	Along	0.225	0.222	0.211	1.192
	Up	0.279	0.246	0.127	1.675
	3D	0.453	0.427	0.290	2.273

The overall solution accuracies of datasets 1-3 resulted in meter-level accuracy with the horizontal components more accurate than the vertical components. The accuracy of dataset 4 is significantly worse than the other three datasets because of the challenging environment. Dataset 4 was collected in a turbulent river with high cliffs and vegetation alongside the riverbank. These factors

contribute to a loss of satellite signals which is reflected in Figure 4.13 and will degrade the accuracy of the GPS solution.

4.5 Comparison of Loose and Tight GPS/INS Coupling

In contrast to the GPS only solutions presented above, a GPS/INS integrated system provides a continuous solution between GPS updates and in the occurrence of partial or full GPS outages. In this section, dataset 1 is used to compute the results of both loosely and tightly coupled implementations. Five main GPS/INS configurations are compared and presented in this section to assess and illustrate the different integration approaches. These are:

- LC integration with complete satellite coverage,
- LC integration with two GPS satellite outages,
- TC integration with complete satellite coverage,
- TC integration with two GPS satellite outages, and
- TC integration with two partial GPS satellite outages.

Firstly, the results of the LC and TC integrations in ideal circumstances with complete GPS satellite coverage are compared to demonstrate their differences. The RMSE and standard deviations of both are shown in Table 6. The difference between the two solutions is at a centimeter level and the standard deviations indicate that the TC integration results in a more optimistic estimate. The difference between the LC and TC results could be attributed to the LC extra addition of process noise by using two separate filters for the GPS and GPS/INS solution, and the TC integration ability to smooth the GPS measurement error.

Table 6: RMSE and standard deviations of GPS/INS LC and TC with complete GPS satellites

		LC		TC	
		RMSE	Standard Deviations	RMSE	Standard Deviations
Position (m)	Across	1.070	0.730	1.181	0.763
	Along	1.872	1.871	1.825	1.816
	Up	4.800	4.515	4.714	4.443
	3D	5.262	2.853	5.191	2.806
Velocity (m/s)	Across	0.359	0.356	0.460	0.459
	Along	0.298	0.297	0.451	0.362
	Up	0.295	0.266	0.417	0.411
	3D	0.552	0.308	0.767	0.412

The azimuth of both solutions and the reference trajectory is illustrated in Figure 4.14. As shown here, the LC and TC accumulates drift from the reference trajectory as time progresses. This drift is a result of the inertial sensor errors accumulating and a heading correction could be used to mitigate this drift and re-initialize the azimuth periodically.

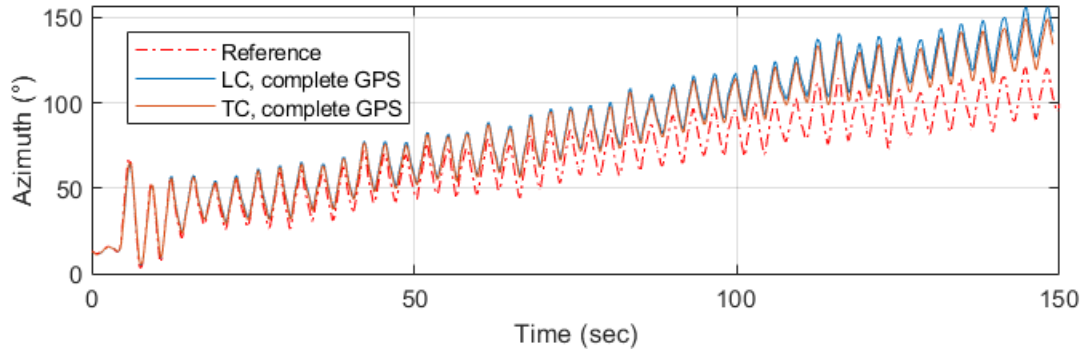


Figure 4.14: Dataset 1 LC, TC, and reference azimuth

With complete GPS satellite availability, both GPS/INS integration techniques are comparable to one-another. However, satellite GPS data outages can frequently occur on a river due to canyon walls or bridges; satellite data outages are simulated here to mimic these situations. To assess the position and velocity performance of both the LC and TC solutions in these scenarios, both partial and complete satellite outages with a duration of 20 seconds each are implemented on dataset 1.

A partial satellite outage occurs when there are less than 4 satellites available for the GPS solution and a complete satellite outage occurs when there are no GPS satellites available. The partial data outages were simulated by raising the elevation mask during the selected time periods. The trajectory of dataset 1 along with the locations of the simulated data outages are shown in Figure 4.15. The locations of the data outages were selected to allow the system to converge and recover both before and after each outage. This allows the GPS to update the inertial sensors errors and correct for any drift in the position and velocity solutions.

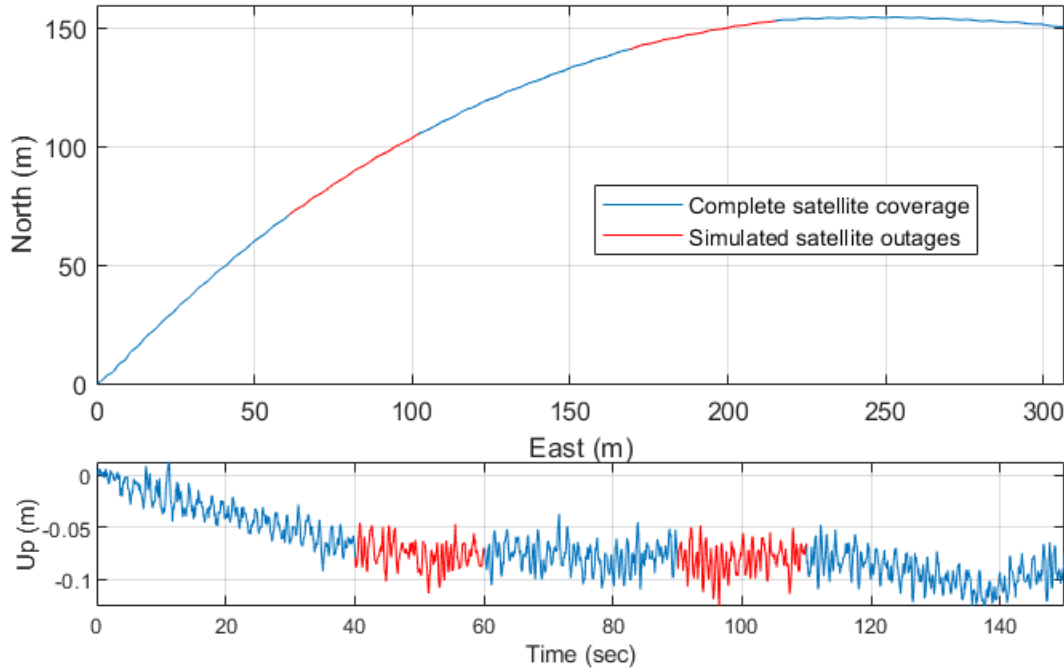


Figure 4.15: Dataset 1 reference trajectory and simulated satellite data outages

The position and velocity errors of the first simulated outage are shown in Figure 4.16. As illustrated here, the solution degrades rapidly in the INS-only solutions where complete GPS outages occur. During these outages, the system relies solely on the inertial solution and the errors due to the estimated INS parameters introduce linear and quadratic errors in the velocity and position solutions. The TC solution with partial GPS availability shows significant improvement in both the position and velocity errors over the complete GPS outage scenarios. In this instance, the system relies on both the inertial solution and errors, and the quality of the available GPS information. Given the magnitude of accumulating errors of the low-grade inertial system, the

periodic corrections from a few satellites in GPS-challenged environments provides a more accurate solution.

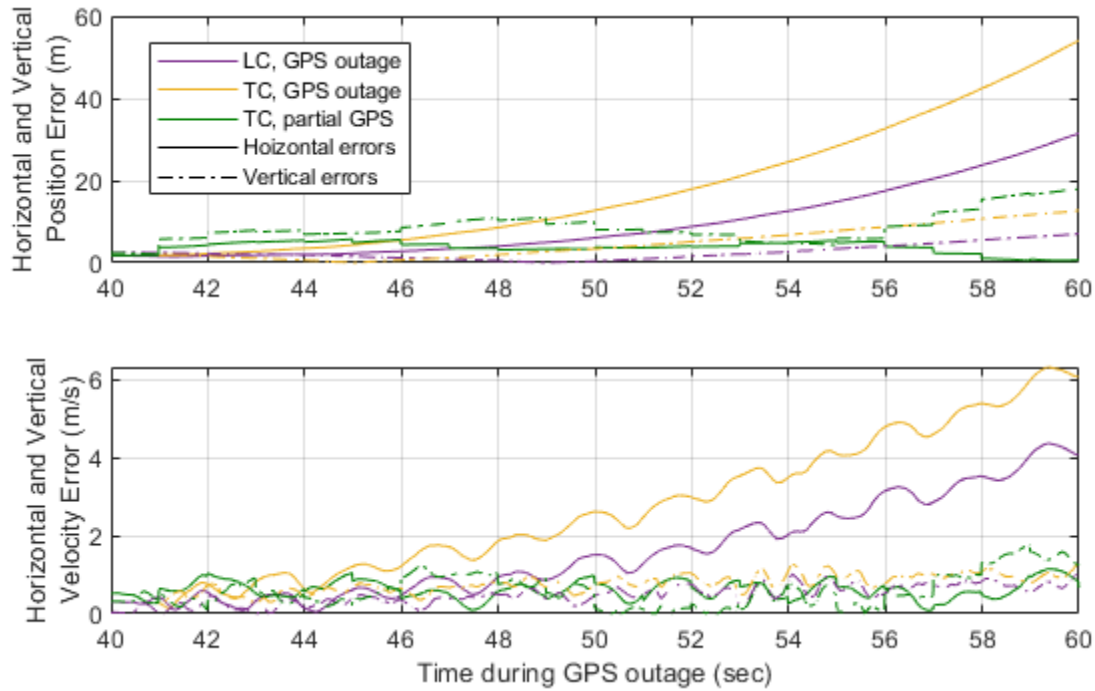


Figure 4.16: Position and velocity errors of dataset 1 during GPS partial and complete outages

The RMSE and corresponding standard deviations of both GPS outages combined from dataset 1 are shown in Figure 4.17 and Figure 4.18 respectively. As illustrated here, the 3D position degrades to an error of approximately 19 and 36 metres for the LC and TC solutions respectively during a complete GPS outage of 20 seconds. The TC solution degrades more rapidly than the LC during a complete GPS outage, this is due to the observations estimating the clock drift. The position error grows quadratically and the velocity error grows linearly. A TC partial satellite outage results in a 3D position error of 10 metres, increasing the reliability of the solution over the systems with no GPS satellites. The standard deviations displayed in Figure 4.18 during a partial or complete outage increases as time progresses, this is due to the accumulation of inertial sensor errors which increasing the uncertainty of the solution.

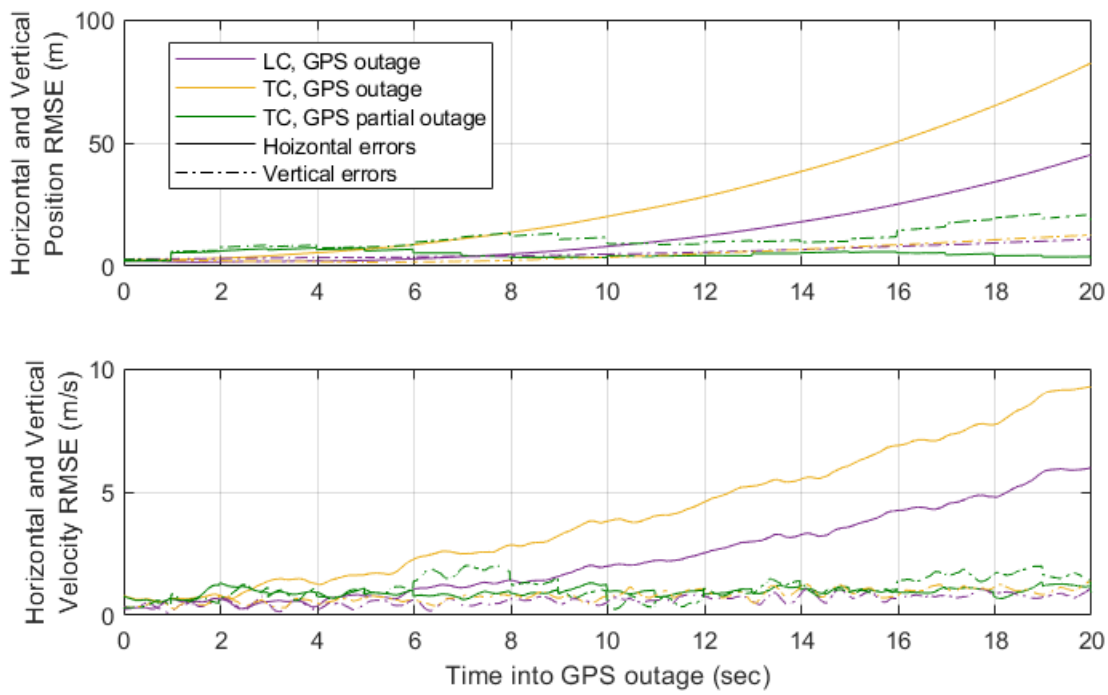


Figure 4.17: RMS position and velocity errors during all partial or complete GPS data outages

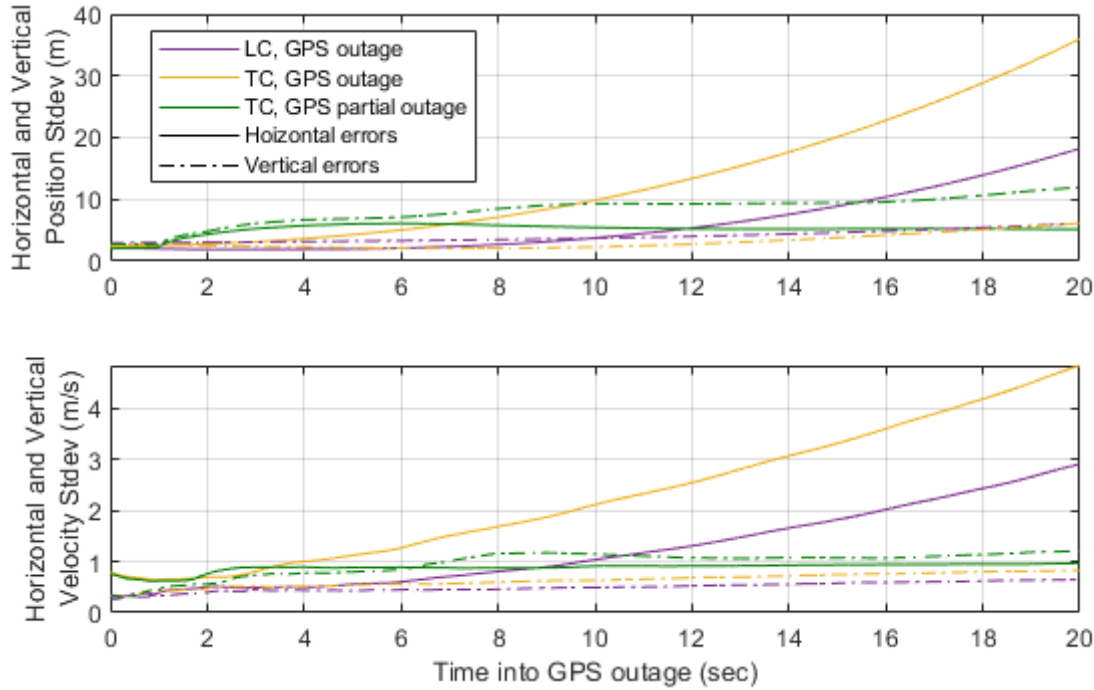


Figure 4.18: Estimated LC and TC standard deviations during all GPS data outages

A summary of both LC and TC configurations with and without complete or partial satellite outages is provided in Table 7. Both integration schemes are comparable with complete GPS

coverage providing RMSE of 1-2 metres and both solutions degrade rapidly during complete satellite outages with RMSE's exceeding 10 metres. The advantage of a TC filter is that it is more accurate in a GPS-challenge environments where only partial satellites are available while the LC filter relies wholly on the INS solution in these situations. However, even partial satellite availability results in a poorer solution than complete satellite coverage. With a lower number of satellites available, the geometry for GPS error mitigation and number of redundancies for blunder and outlier detection is diminished.

Table 7: RMSE of GPS/INS LC and TC position of dataset 1

	RMSE	LC		TC		
		Complete GPS	GPS outages	Complete GPS	GPS outages	Partial GPS
Position (m)	Across	1.070	2.792	1.181	10.095	2.588
	Along	1.872	7.316	1.825	18.688	2.049
	Up	4.800	5.019	4.714	5.000	6.405
	3D	5.262	9.301	5.191	21.821	7.206
Velocity (m/s)	Across	0.359	0.819	0.460	1.075	0.574
	Along	0.298	1.509	0.451	2.580	0.544
	Up	0.295	0.353	0.417	0.508	0.624
	3D	0.552	1.753	0.767	2.841	1.007

The analysis here concludes that the horizontal solution from a GPS/INS system with complete satellite coverage is accurate to 1 to 2 metres, while the vertical solution produces 5 metres accuracy. Both the LC and TC solutions degrade rapidly in the event of complete satellite outages due to the INS performance. Therefore, the navigation solution in GPS-challenged environments such as canyons or under vegetation is of poor performance. Expanding beyond the position and velocity states in the 15-state GPS/INS filter, the system alignment can also be analyzed and used as an indicator for the inertial systems alignment. Figure 4.19 illustrates the pitch and roll (tilt) angles of the LC and TC solutions with full satellite coverage.

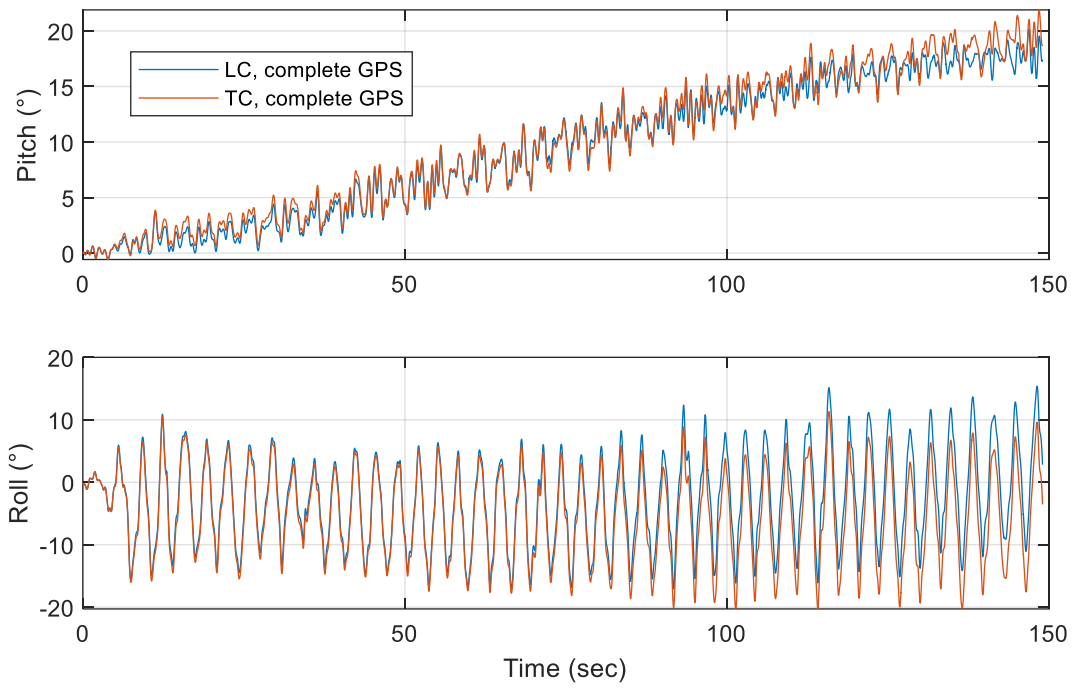


Figure 4.19: Estimated LC and TC standard deviations

As can be seen here, the tilt angles deviate and drift away from a centroid of zero. This implies that the kayak itself is tipping up on its stern and rolling over, however, this is not indicative of the actual kayak motion. Therefore, a possible approach to improve the INS solution during GPS outages would be to correct these attitude angles to match the expected motion, and by extension correct the alignments of the gyroscope and accelerometer sensors. The next chapter will explore this hypothesis as a method of solving the limitations of a LC GPS/INS solution in GPS-challenged environments.

Chapter 5: GPS/INS Motion Constraints and Results

The results of the previous chapter show that the error growth of the solution during a GPS outage rapidly accumulates without corrections from the GPS. It is known that the performance of a low grade INS degrades rapidly, and is incapable of providing accurate solutions over long periods of time because of the accumulation of errors that occur over short time intervals (X. Niu et al., 2007). Additional external sensors or the implementation of motion constraints can be utilized to mitigate these errors. In the case of a consumer grade smartphone, additional sensors make the system more complex, bulky, expensive, and may not be readily available to a consumer. However, motion constraints are a viable option to reduce sensor errors and improve the navigation solution.

As mentioned in Chapter 1, several different methods of motion constraints have been previously used to reduce INS drift in a system. Most notably included are: ZUPT (Foxlin, 2005; Grejner-Brzezinska et al., 2001), NHCs (X. Niu et al., 2007), ZARUs (Rajagopal, 2008)., and height constraints (Godha & Cannon, 2007). ZUPT (or ZVU) and ZARUs are used in applications when the host vehicle/body has periods of time that are stationary. They exploit the knowledge of a stationary system to reset any residual measurements in the gyroscope or accelerometer or velocity directions. Unfortunately, zero updates are not a feasible solution for kayaking because the kayak is always in motion and the measurements cannot be assumed to be zero at any given point in time. NHCs such as those used in vehicle navigation assume that the vehicle is only moving in the along track direction and not in the across or up directions. Because a kayak's velocity in water is moving in all directions with each paddle stroke, NHCs constraining the body frame velocities cannot be used.

To overcome the INS error growth identified during GPS outages, constraints unique to the motion of a kayak are utilized. In this chapter, details pertaining to each constraint are presented along with their associated system models. Results of these proposed motion constraints are then presented with an emphasis on the navigation solution accuracy performance GPS outages.

5.1 Motion Constraints

With the knowledge of the environment and motion¹ for a kayak on a river, a few separate motion constraints can be applied to improve the INS drift and navigation solution. The first constraint relies on the assumption that the height does not change significantly over a short time interval or that there are no abrupt changes. The second constraint estimates the gyroscope bias. It is based upon the knowledge that the motion of a kayak in calm water is cyclic in nature, and the roll and pitch of the kayak will return to the same orientation at regular time intervals. The third constraint is constructed from the knowledge that the mean values of the roll and pitch angles are zero; this is because the kayak is not inverting or standing on end. The final constraint estimates the accelerometer bias and is based upon the previous gyroscope bias and tilt constraints. A diagram illustrating how these four constraints would be added to the GPS/INS filter is shown in Figure 5.1. Further details regarding the implementation of each constraint are provided in the following sections.

¹ Refer to Chapter 1 for more information regarding kayak motion through water.

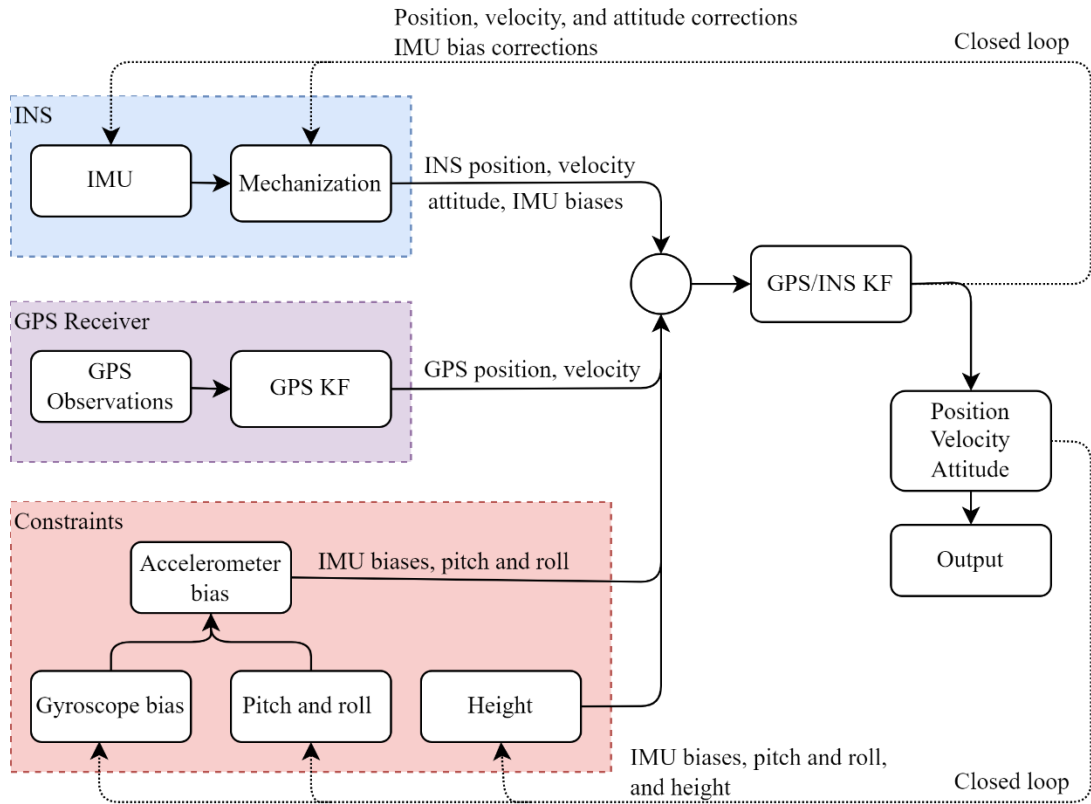


Figure 5.1: Motion constraint schematic

5.1.1 Height Constraints

When a kayak travels down a calm river or across a lake, the kayak stays on the water and the height fluctuation can be assumed to vary minimally over a small interval of time. A constant value derived from a prior GPS measurement can be used as a measurement update in the instance between GPS updates or during GPS outages. The dilution of precision (DOP) is evaluated to ensure that the last GPS height estimation was obtained in good measurement conditions (Groves, 2007). Constraining the height during inertial navigation will prevent the kayak from moving vertically and improve the horizontal component accuracies (Godha & Cannon, 2007).

The measurement vector for a height constraint is defined as:

$$\delta z = [h_{INS} - h_{ref}] \quad 5.1$$

where:

h_{INS} is the height derived from the INS

h_{ref} is the reference GPS height value defined for the outage interval

The corresponding measurement noise is set according to the measurement uncertainty from the GPS derived height. The height constraint row in the design matrix is:

$$H = [0 \quad 0 \quad 1 \quad 0_{1 \times 9}] \quad 5.2$$

5.1.2 Gyroscope Bias Constraints

In an INS, gyroscope errors have the most significant effect on the solution because these errors directly compound into the attitude and orientation of the system. Recall that the GPS/INS EKF relies on previous knowledge of the IMUs alignment and dynamics to determine the current position, velocity, and attitude solution. In this process, the Earth's gravity is removed from the accelerometer measurements. Typically, the accelerations measured from the device are smaller than the Earth's gravitational acceleration. If there is a slight misalignment of the accelerometer axis which is derived from the gyroscope data, gravitational acceleration may be removed from the wrong component. Therefore, a misaligned gyroscope will contribute to more errors in the derived velocity and position solutions that are derived from the accelerometer measurements. Gyroscope errors in an INS can be a product of a low-grade sensor noise (such as that found in a Google Pixel 4) and a misaligned gyroscope in the strapdown configuration. A misalignment of the IMU can easily occur if the static data used for the misalignment procedure (section 2.9) is biased by a small amount which can happen due to choppy water or a slight tilt during the static data collection period.

The integration of gyroscope data accumulates noise and bias over time resulting in drift of the tilt (roll and pitch) angles. The angles will be less noisy than the raw gyroscope measurements due to integration over time, however there is more drift present. Figure 5.2 depicts the tilt angles of a kayak from the integration of gyroscope output by time. The two scenarios shown in this figure illustrate the expected tilt angles produced from the gyroscope data which is shown in green, and the resulting angles in a system with errors present shown in purple. The motion of a kayak is cyclic in nature, meaning the body frame of the kayak returns to the same tilt at regular time

intervals. It is assumed that a kayak traversing down a river will not roll over or pitch up and down severely, these values are expected to oscillate around a centroid of zero. The accumulation of errors and drift leads to a misalignment of the orientation of the IMU sensors resulting in a wrong velocity and position trajectory. By correcting the tilt angles to those that accurately reflect the motion of a kayak, the alignment of the accelerometer is adjusted to improve the estimated navigation solution.

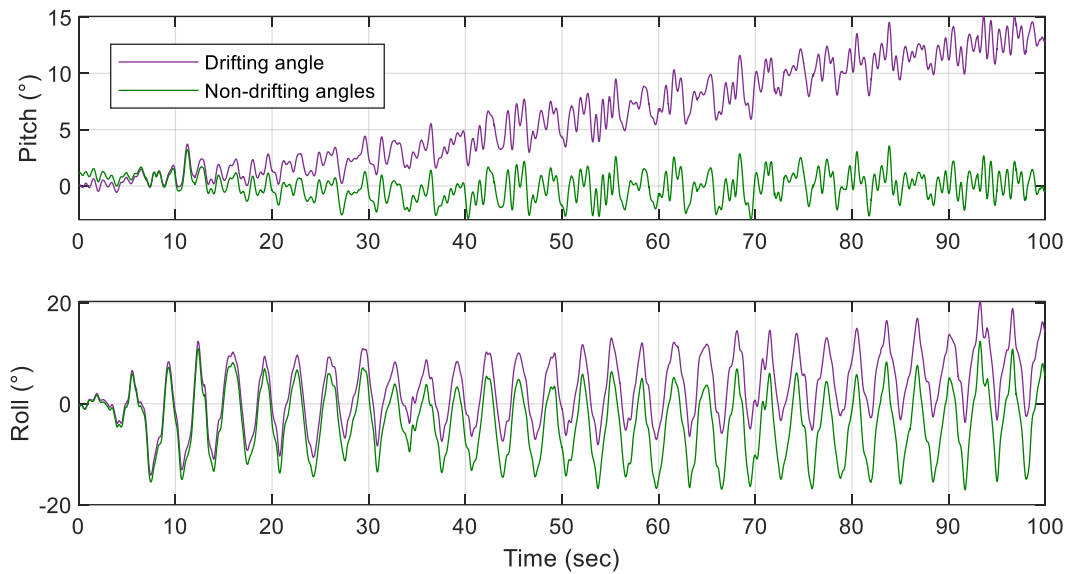


Figure 5.2: Drifting and non-drifting angles calculated from gyroscope measurement integration

Due to the constant motion of the tilt angles, applying an update or constraint to these angles themselves proves to be difficult because of irregularities that can occur in the kayak motion. An assumption that the oscillation of the roll and movement of the pitch is periodically uniform is not an adequate hypothesis for many instances of kayaking. For example, various water conditions may include choppy waters or waves, and a paddler with an irregular stroke rate or movement would contribute to irregularities in the tilt angles. Therefore, updating the gyroscope bias is a more feasible solution.

Because gyroscope bias is a constant error and not oscillating, it can be applied at each epoch of measurement (Kirkko-Jaakkola et al., 2012). The relationship between the raw gyroscope output and tilt angles is used to estimate the expected gyroscope error which can then be used to correct the gyroscope bias in the GPS/INS system. This approach is similar to that used in ZARUs where

an additional redundancy is added when the host body is stationary. However, in this case the gyroscope bias is estimated based upon the assumption that the derivative of both roll and pitch should be zero. Therefore, the expected bias, $\delta\omega_{estimated}^b$, of the gyroscope can be calculate as shown in (5.3).

$$\delta\omega_{estimated}^b = \frac{d}{dt}\theta \quad 5.3$$

The corresponding measurement model and design matrix of this bias update are defined in (5.4) and (5.5) respectively.

$$\delta z = [\delta\omega_{INS}^b - \delta\omega_{estimated}^b] \quad 5.4$$

$$H = [0_{1x9} \quad 1_{1x3} \quad 0_{1x3}] \quad 5.5$$

where:

$\delta\omega_{INS}^b$ is the gyroscope sensor biases estimated from the INS in the b-frame

$\delta\omega_{estimated}^b$ is the estimated reference gyroscope sensor bias in the b-frame

The roll of a kayak is determined by each paddle stroke from the kayaker creating a cyclic periodic motion, whereas the pitch contains more noise which may be caused by other factors including water choppiness. Due to the irregularities in both tilt angles, estimating the gyroscope bias at each epoch of observation could result in more system noise and further errors because of an incorrect estimated bias. Therefore, gyroscope bias estimation can only be completed by utilizing a window of observations for a duration of time prior to the current epoch. In this thesis, the window size is based upon the selection of a sufficient number of full, completed cycles of the roll. Selecting full periodic waves ensures the estimated gyroscope bias is not skewed by half of a cycle in the paddle stroke. Figure 5.3 illustrates an example of a window of time used to estimate the gyroscope bias. The green dots signify the start and end of the selected window, and the grey area highlights the full extent of observations used. In this example, eight full cycles are used for a duration of 25 seconds. A sufficient length of time should be included in the window of observations to mitigate

any irregular noise or outliers in the tilt angles that could also contribute to an incorrect bias estimation.

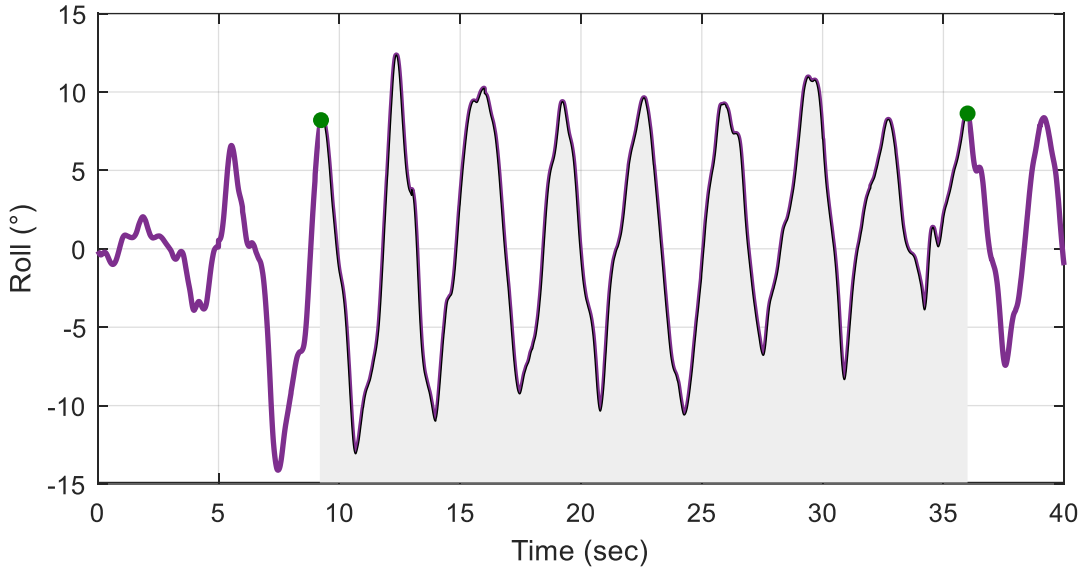


Figure 5.3: Cycle selection

Due to the predictable nature of the roll, a periodic EKF can be applied to minimize extraneous roll measurements caused by irregular paddle strokes or sensor noise and improve the gyroscope bias estimate described above. The next section details a periodic EKF of a signal that can be applied to the roll.

5.1.2.1 Periodic Extended Kalman Filter

A periodic EKF can be used to predict and estimate a periodic waveform and minimize irregularities in the signal. A paddle stroke in the roll creates a periodic waveform that could contain varying frequency, amplitudes, and offsets. By decreasing the irregularities and noise in the signal, and identifying complete paddle stroke cycles, the estimate of the gyroscope bias improves. The periodic EKF models are described in this section and further details can be found in Mendoza & O'Keefe (2021) and Saboury (2019)

A waveform (system output) is represented as a function of time in (5.6) with the state transition in (5.7). This dynamics model was selected as a constant model because it is expected that each cycle will remain constant from one paddle stroke to the next.

$$y(t) = A_0 + A_1 \cos(\omega_r t + \phi_1) \quad 5.6$$

$$\Phi_{k,k+1} = [I_{4x4}] \quad 5.7$$

where:

A_0 is the DC offset

A_1 is the magnitude of the fundamental harmonic

ω_r is the rotation velocity

ϕ_1 is the rotation angle offset of the fundamental

The state vector is as illustrated:

$$\delta x_k = [A_0 \quad A_1 \quad \omega \quad \phi_1] \quad 5.8$$

The observation equation (5.6) is used to construct the design matrix (5.9) as a function of the state vector.

$$H_{k,6} = [1 \quad \cos(\omega_r t_k + \phi_1) \quad -A_1 \sin(\omega_r t_k + \phi_1) \quad -A_1 t_k \sin(\omega_r t_k + \phi_1)] \quad 5.9$$

Figure 5.4 shows the results from the periodic EKF applied to the roll of the system. The original signal is shown in purple, and the results from the periodic EKF are shown in green. The filtered signal mitigates anomalies (spikes) in the observed signal. The anomalies in the original signal can apply a weight to the gyroscope bias estimate that does not reflect the true motion of the kayak. Therefore, by using the smoothed signal, these anomalies are reduced and a more accurate gyroscope bias can be estimated.

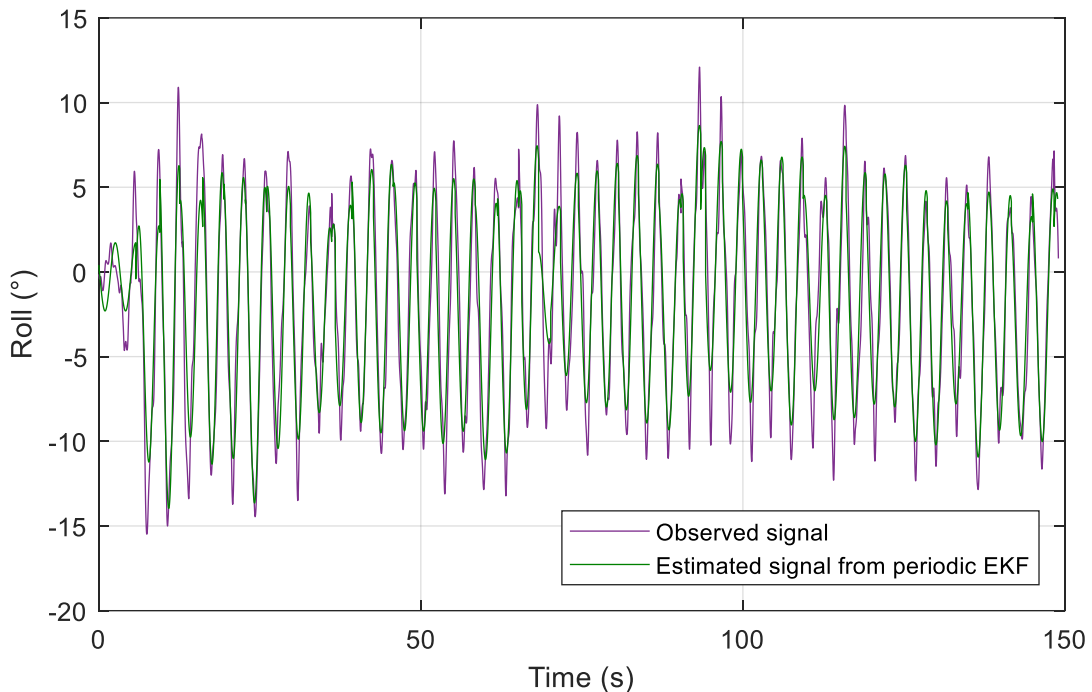


Figure 5.4: Observed roll and estimated roll from periodic EKF

These motion constraints applied to the gyroscope bias assume that the tilt angles of the kayak are centered around zero. The gyroscope bias constraint detailed in this section estimates the error in the bias and mitigates the drift of the tilt angles, however, there may still be an offset from zero in the pitch and roll following the application of this constraint that must be corrected for.

5.1.3 Tilt Angle Offset Constraints

A tilt angle offset occurs when the entirety of the angle is not centered around zero, as is expected in kayaking. An example of this offset for the roll is displayed in Figure 5.5 where the roll with an offset is shown in purple, and the correct roll is shown in green.

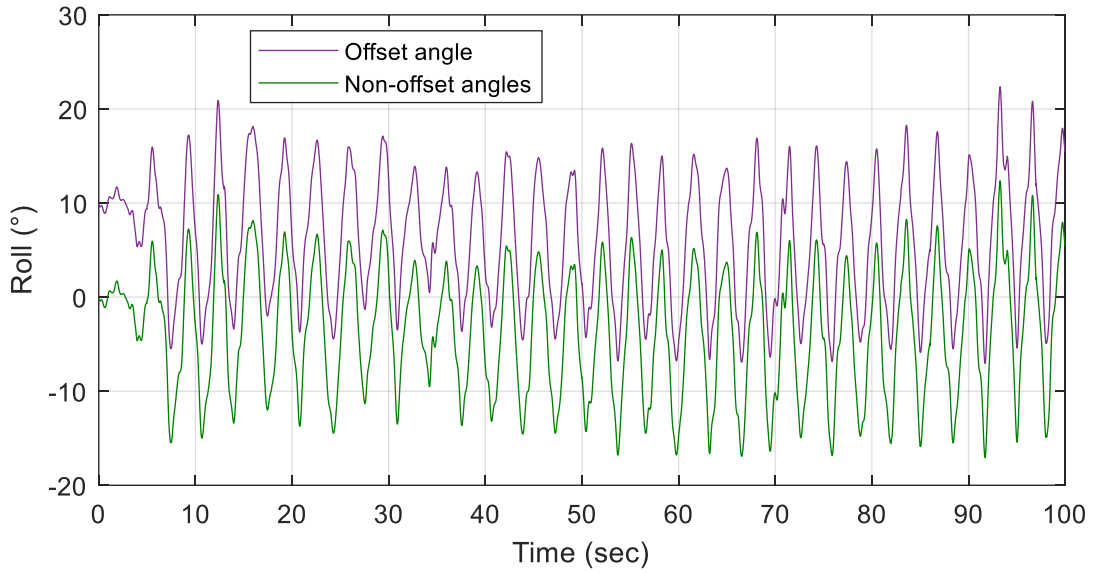


Figure 5.5: Offset and non-offset roll calculated from gyroscope measurement integration

To correct for this offset, a constraint similar to external heading aiding can be used (Godha & Cannon, 2007). An error dynamics equation is used to relate the measurements to the system error states. Recall equation (3.43) that is repeated here (5.10) which relates the attitude errors of pitch, roll, and yaw to the frame rotation matrix. This error equation is used to derive roll and pitch constraints in the sub-sections below.

$$\begin{aligned}\hat{R}_b^l &= (I - \Omega_{\varepsilon^l}) R_b^l \\ \hat{R}_b^l &= \left(I - \begin{bmatrix} 0 & -\varepsilon_{\psi_y} & \varepsilon_r \\ \varepsilon_{\psi_y} & 0 & -\varepsilon_p \\ \varepsilon_r & \varepsilon_p & 0 \end{bmatrix} \right) R_b^l\end{aligned}\quad 5.10$$

5.1.3.1 Pitch Constraint

The pitch angle is derived from the rotation matrix as:

$$\hat{p} = \sin^{-1}(\hat{R}_b^l(3,2)) \quad 5.11$$

Combining the error equation (5.10) and pitch derivation (5.11) becomes:

$$\hat{p} = \sin^{-1} \left(\varepsilon_p R_b^l(2,2) - \varepsilon_r R_b^l(1,2) + R_b^l(3,2) \right) \quad 5.12$$

The pitch error equation (5.13) is then estimation as a function of the errors in pitch, roll, and yaw ($\varepsilon_p, \varepsilon_r, \varepsilon_{\psi_y}$) with the full derivations defined in (5.14).

$$\delta \hat{p} = \frac{\partial p}{\partial \varepsilon_p} \varepsilon_p + \frac{\partial p}{\partial \varepsilon_r} \varepsilon_r + \frac{\partial p}{\partial \varepsilon_{\psi_y}} \varepsilon_{\psi_y} \quad 5.13$$

$$\frac{\partial p}{\partial \varepsilon_p} = \frac{R_b^l(2,2)}{\sqrt{1 - (R_b^l(3,2))^2}}$$

$$\frac{\partial p}{\partial \varepsilon_r} = \frac{R_b^l(1,2)}{\sqrt{1 - (R_b^l(3,2))^2}} \quad 5.14$$

$$\frac{\partial p}{\partial \varepsilon_{\psi_y}} = 0$$

The measurement model and corresponding row in the design matrix are shown in (5.15) and (5.16) respectively. The

$$\delta z = [p_{INS} - p_{estimated}] \quad 5.15$$

$$H = \begin{bmatrix} 0_{1 \times 6} & \frac{\partial p}{\partial \varepsilon_p} & \frac{\partial p}{\partial \varepsilon_r} & \frac{\partial p}{\partial \varepsilon_{\psi_y}} & 0_{1 \times 6} \end{bmatrix} \quad 5.16$$

5.1.3.2 Roll Constraint

The roll constraint is formed similarly to the pitch. Roll is computed as shown in (5.17) and is further expanded based on the error equation to (5.18).

$$\hat{r} = -\tan^{-1} \left(\frac{\hat{R}_b^l(3,1)}{\hat{R}_b^l(3,3)} \right) \quad 5.17$$

$$\hat{r} = -\tan^{-1} \left(\frac{\varepsilon_p R_b^l(2,1) - \varepsilon_r R_b^l(1,1) + R_b^l(3,1)}{\varepsilon_p R_b^l(2,3) - \varepsilon_r R_b^l(1,3) + R_b^l(3,3)} \right) \quad 5.18$$

The error of roll is then calculated in (5.19) with its corresponding derivatives in (5.20).

$$\delta \hat{r} = \frac{\partial r}{\partial \varepsilon_p} \varepsilon_p + \frac{\partial r}{\partial \varepsilon_r} \varepsilon_r + \frac{\partial r}{\partial \varepsilon_{\psi_y}} \varepsilon_{\psi_y} \quad 5.19$$

$$\begin{aligned} \frac{\partial r}{\partial \varepsilon_p} &= \frac{R_b^l(3,1)R_b^l(2,3) - R_b^l(2,1)R_b^l(3,3)}{R_b^l(3,1)^2 + R_b^l(3,3)^2} \\ \frac{\partial r}{\partial \varepsilon_r} &= \frac{R_b^l(1,1)R_b^l(3,3) - R_b^l(1,3)R_b^l(3,1)}{R_b^l(3,1)^2 + R_b^l(3,3)^2} \\ \frac{\partial r}{\partial \varepsilon_{\psi_y}} &= 0 \end{aligned} \quad 5.20$$

The corresponding measurement vector (5.21) and row in the design matrix (5.22) are:

$$\delta z = [r_{INS} - r_{estimated}] \quad 5.21$$

$$H = \left[\begin{matrix} 0_{1 \times 6} & \frac{\partial r}{\partial \varepsilon_p} & \frac{\partial r}{\partial \varepsilon_r} & \frac{\partial r}{\partial \varepsilon_{\psi_y}} & 0_{1 \times 6} \end{matrix} \right] \quad 5.22$$

5.1.4 Accelerometer Bias Constraints

In an INS, the angular rates from the gyroscope are integrated to determine the orientation of the IMU in the strapdown system. This orientation is determined by the gyroscope measurements and corresponding bias. With the gyroscope bias corrected using the previous constraints, the accelerometer bias must also be adjusted to incorporate the changes in the IMUs orientation. Therefore, the proposed solution utilizes the newly computed tilt angles to estimate the accelerometer biases as shown in (5.23). In this equation, the local-level frame specific force measurements (f_{INS}^l) are extracted from the mechanization process; the rotation matrix from the l -frame to the b -frame ($R_{l_{estimated}}^b$) is calculated using the new tilt angles; and (f^b) represent the current accelerometer measurements of the system.

$$\delta f_{estimated}^b = f^b - R_{l_{estimated}}^b f_{INS}^l \quad 5.23$$

where $R_{l_{estimated}}^b$ is the rotation matrix from the l -frame to the b -frame with adjusted attitude angles

The measurement model and design matrix corresponding to this constraint are shown in (5.24) and (5.25) respectively

$$\delta z = [\delta f_{INS}^b - \delta f_{estimated}^b] \quad 5.24$$

$$H = [0_{1 \times 12} \quad 1_{1 \times 3}] \quad 5.25$$

The next section presents the performance of the navigation solution with the height, gyroscope bias, tilt angle offset, and accelerometer constraints applied.

5.2 Dataset 1 Results

An analysis of the results from dataset 1 is discussed in detail in this section and the results of datasets 2-4 are presented following this section to further validate the proposed motion constraints. The attitude, gyroscope bias, velocity errors, accelerometer bias, and final position results are presented here.

In order to assess the performance of the updates and constraints presented in this chapter on dataset 1; four different configurations were selected to be applied using loosely coupled GPS/INS integration. These are:

1. Full GPS availability throughout the entire dataset with no constraints or updates applied.
2. A simulated GPS outage from 90 – 110 seconds with no constraints or updates applied.
3. A simulated GPS outage from 90 – 110 seconds with height, gyroscope bias, and tilt offset constraints applied.
4. A simulated GPS outage from 90 – 110 seconds with height, gyroscope bias, tilt offset, and accelerometer bias constraints applied.

These configurations will be referred to as configuration 1-4 respectively in addition to the reference trajectory that was defined in Chapter 4.

The frequency of the updates applied for this dataset is based off the number of cycles occurring in the roll. The attitude, gyroscope, and accelerometer constraints are applied with every 10 cycles while the height constraints are used between every GPS update and during the GPS outages. 10

cycles were chosen for this dataset as it encapsulates enough data for reasonable bias estimates and corrections.

Figure 5.6 illustrates the attitude results of the four scenarios described above. The uncertainties of each predicted state are represented with transparent lines of the same colours of each configuration. As evident with the tilt angle uncertainties, a tilt offset update is applied for every 10 cycles of roll at times 36, 65, 91, 115, and 148 seconds. The uncertainty of these tilt states increases between each update time and decreases at the constraint update times because the certainty of the estimate increases with an applied constraint.

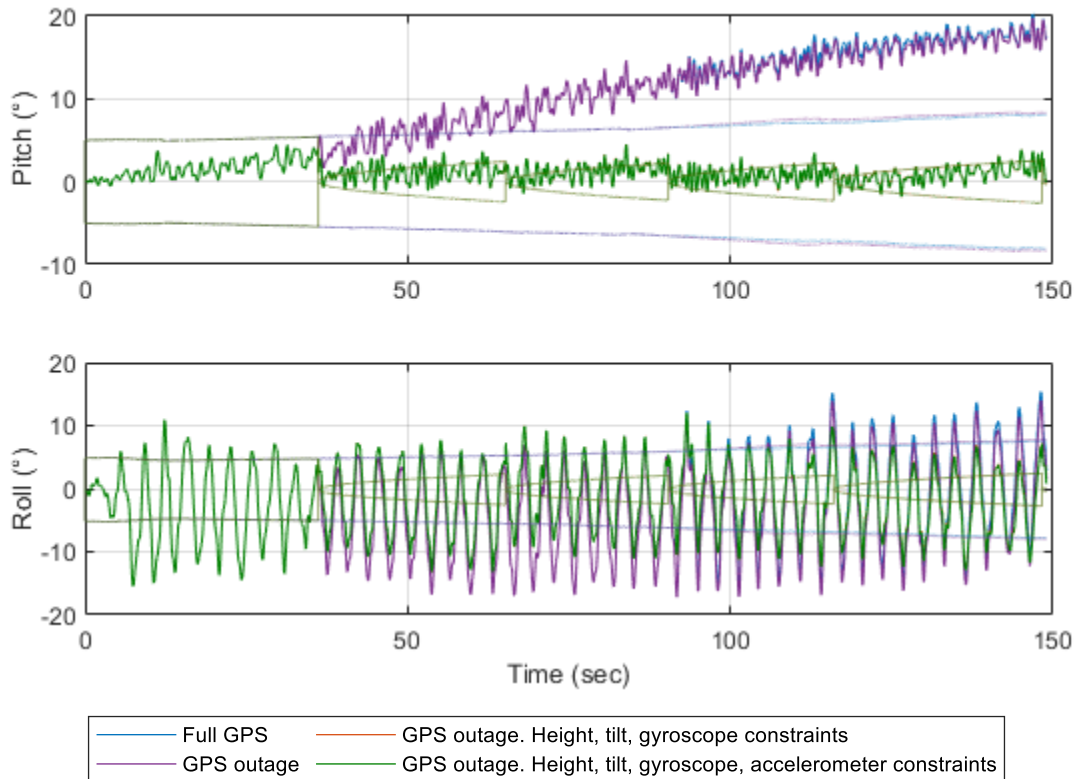


Figure 5.6: Tilt angles of dataset 1 with and without motion constraints

The tilt angles in the full GPS (blue) and GPS outage (purple) scenario drift from the centroid around zero indicating that the kayak is tilting up and rolling. These tilt angles misrepresent the actual motion of the kayak for the data collected, the kayak was not rolling and remained flat on the water. Whereas the configurations with constraints applied (orange and green overlaying) show the expected and correct tilt angles of the kayak. Therefore, the application of a gyroscope bias,

and tilt offset constraints on this dataset is proven to correct the tilt angles to reflect the real-world scenario of a kayak travelling on water.

The attitude results presented in Figure 5.6 are a product of both the tilt offset, and gyroscope bias constraints. Figure 5.7 compares the difference in gyroscope biases between those estimated from the GPS/INS filter with no constraints (blue and purple) and those with constraints applied (orange and green). The largest updates occur in the x -direction of gyroscope which corresponds to the pitch of the kayak, whereas the smaller adjustments on the y -direction are for the smaller drift in the roll angles.

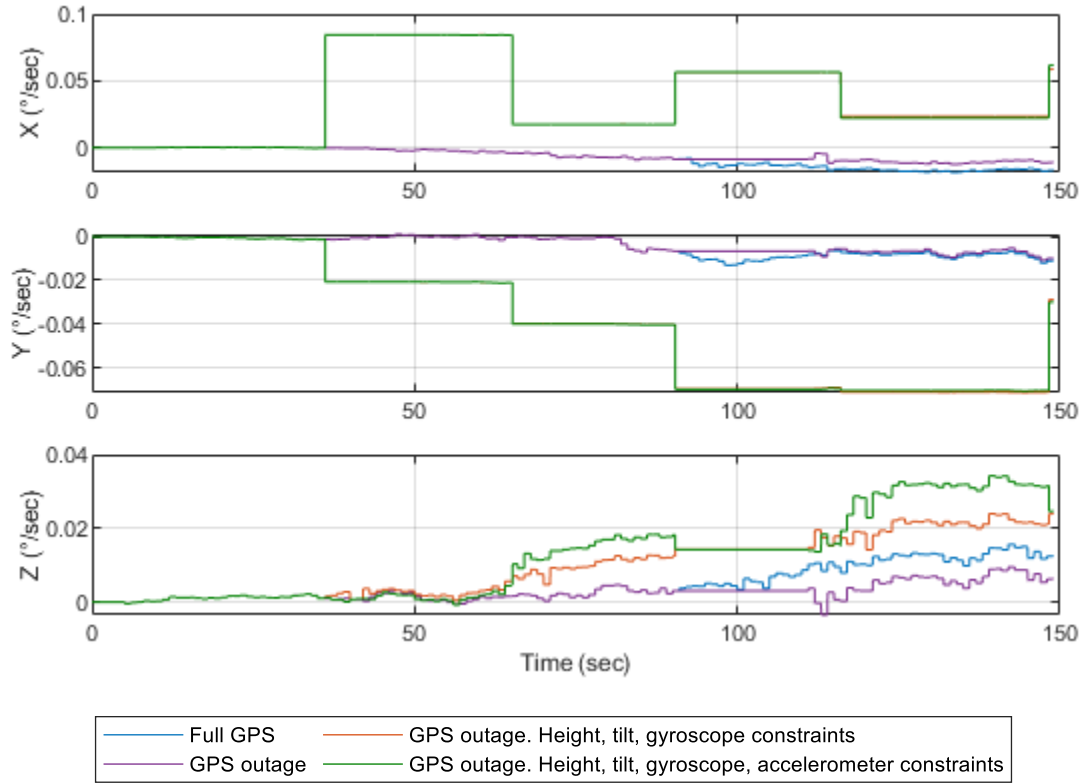


Figure 5.7: Gyroscope bias of dataset 1 with and without motion constraints

Figure 5.8 compares the velocity results of each configuration. The optimal trajectory represented by the blue line is the scenario with full GPS availability and no motion constraints or updates were used. As shown in configuration 2, the velocity accuracy during the GPS outage from 90 – 110 seconds degrades rapidly with no constraints applied. This is expected because any uncompensated errors in the gyroscope or accelerometer will propagate into the INS velocity and

position solutions. Immediately following the GPS outage, the integrated GPS/INS solution will initialize the velocity back to the correct trajectory calculated by the GPS.

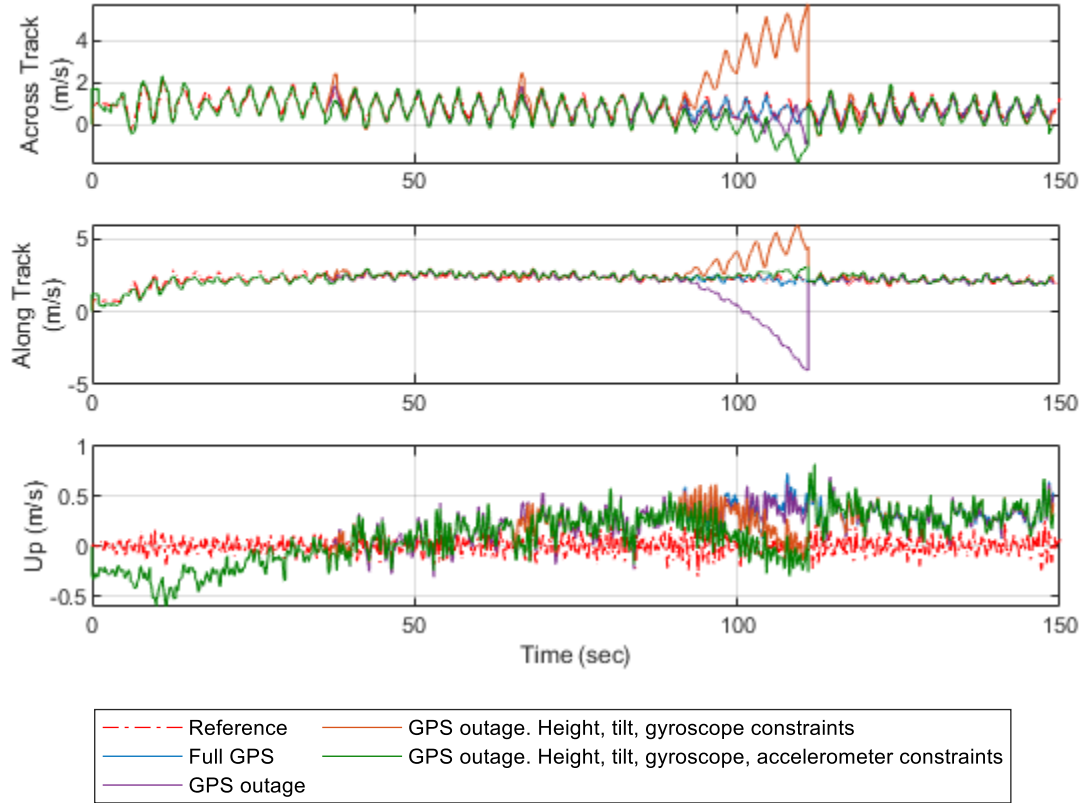


Figure 5.8: Velocity of dataset 1 with and without motion constraints in the body frame

Although configuration 3 resulted in an attitude solution (Figure 5.6) that accurately captured the movement of the kayak, the velocity drift error in the across track direction during the GPS outage is larger than the solution with no constraints applied. This drift is caused by an incorrect estimate of the accelerometer bias following the correction of IMU orientation from the gyroscope bias constraint. Recall the dynamic coefficient matrix for a loosely coupled GPS/INS system from equation (3.39), repeated here in (5.26).

$$\Phi_{k,k+1} = \begin{bmatrix} I_{3x3} & F_r & 0_{3x3} & 0_{3x3} & 0_{3x3} \\ 0_{3x3} & I_{3x3} & F_v & 0_{3x3} & R_b^l \Delta t \\ 0_{3x3} & F_\varepsilon & I_{3x3} & R_b^l \Delta t & 0_{3x3} \\ 0_{3x3} & 0_{3x3} & 0_{3x3} & I_{3x3} + D_\omega \Delta t & 0_{3x3} \\ 0_{3x3} & 0_{3x3} & 0_{3x3} & 0_{3x3} & I_{3x3} + D_f \Delta t \end{bmatrix} \quad 5.26$$

This model shows how the system states are correlated to each other with each update in GPS/INS integration. In the EKF, the weighting factor (gain matrix) used to estimate the states is dependent on both the estimated covariance and measurement noise of each state; and the covariance matrix is a function of the dynamic coefficient matrix. Therefore, each GPS position and velocity update in the filter will correlate to and adjust the accelerometer bias. The orientation of an IMU is calculated from the gyroscope measurements and any error in these measurements will propagate into the velocity and position results that are calculated from the accelerometer measurements. This is because the accelerometer is orientated using the gyroscope. This results in INS velocity and position errors that can propagate in incorrect directions at incorrect rates. GPS position and velocity updates in the EKF will mitigate the IMU alignment error by adjusting the accelerometer biases. An overcorrection of accelerometer biases may occur to compensate for the incorrect estimation of gyroscope errors.

This is evident in the accelerometer bias results shown in Figure 5.9. Configuration 1, 2, and 3 (blue, purple, and green) do not have an accelerometer bias constraint applied and are estimating these biases based solely on GPS updates. The GPS-estimated accelerometer bias in the configuration 1 and 2 with no constraints are compensating for a misalignment error from incorrect gyroscope biases. Whereas configuration 3 and 4 (orange and green) with constraints used to correct the estimated gyroscope biases and corresponding attitude solution, show updated accelerometer biases to account for less misalignment error. Configuration 3 requires a few epochs of GPS observations to readjust the accelerometer biases to account for the change in gyroscope alignment. Configuration 4 updates the accelerometer bias estimates when the gyroscope bias constraints are applied. This is exemplified best at ~88 seconds before the GPS outage occurs. Here, the gyroscope bias has been adjusted to reflect the true motion the kayak, however, there has not been enough GPS/INS epochs before the outage to adjust the accelerometer bias to reflect the change in the IMU orientation. The difference between configurations 3 and 4 in Figure 5.9 lead to a difference in the errors in both the velocity and position solutions during the GPS outages.

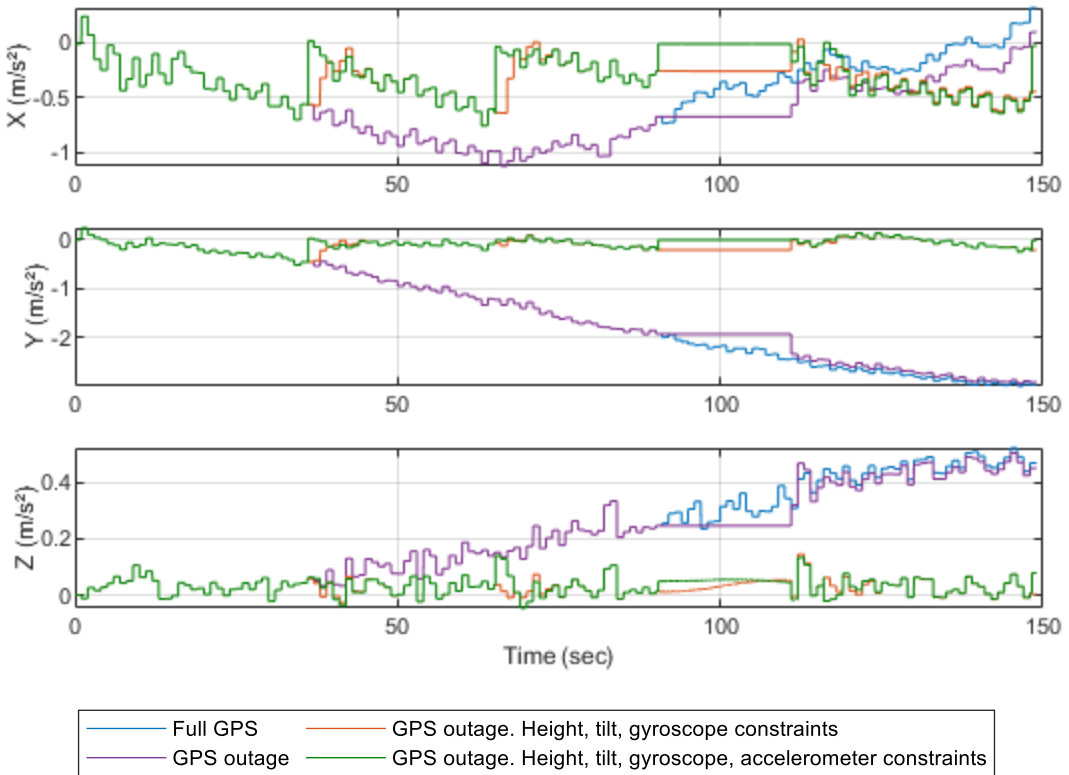


Figure 5.9: Accelerometer bias of dataset 1 with and without motion constraints

The spikes that occur in the velocity in Figure 5.8 in configuration 3 but not in configuration 4 demonstrate the effect that incorrect accelerometer biases have on the solution. These spikes happen because the accelerometer bias has not been corrected for the re-alignment of the system from the gyroscope bias update. Therefore, the accelerometer measurements are skewed to the prior alignment causing a spike in the velocity before the next GPS update corrects the solution.

Figure 5.10 and Figure 5.11 display the velocity and position errors calculated from the reference trajectory during the GPS outage from 90 – 110 seconds. The trajectory of all configurations and the reference solution is shown in Figure 5.12 in the local-level frame. The drift of these solutions in configuration 3 most predominately illustrates the effect of these unadjusted accelerometer biases. Although the application of the accelerometer bias constraints reduced this error identified in configuration 3, it did not fully account for the error in the across track direction. Configuration 4 (green) shows that the error in the across direction results in the same magnitude of the error without constraints (purple). However, configuration 4 maintains the overall amplitude and variation of the velocity from cycle to cycle whereas configuration 2 increases the amplitude of

these cycles. The results from configuration 4 exhibit an improvement to the solution and reduces the errors during the GPS outage.

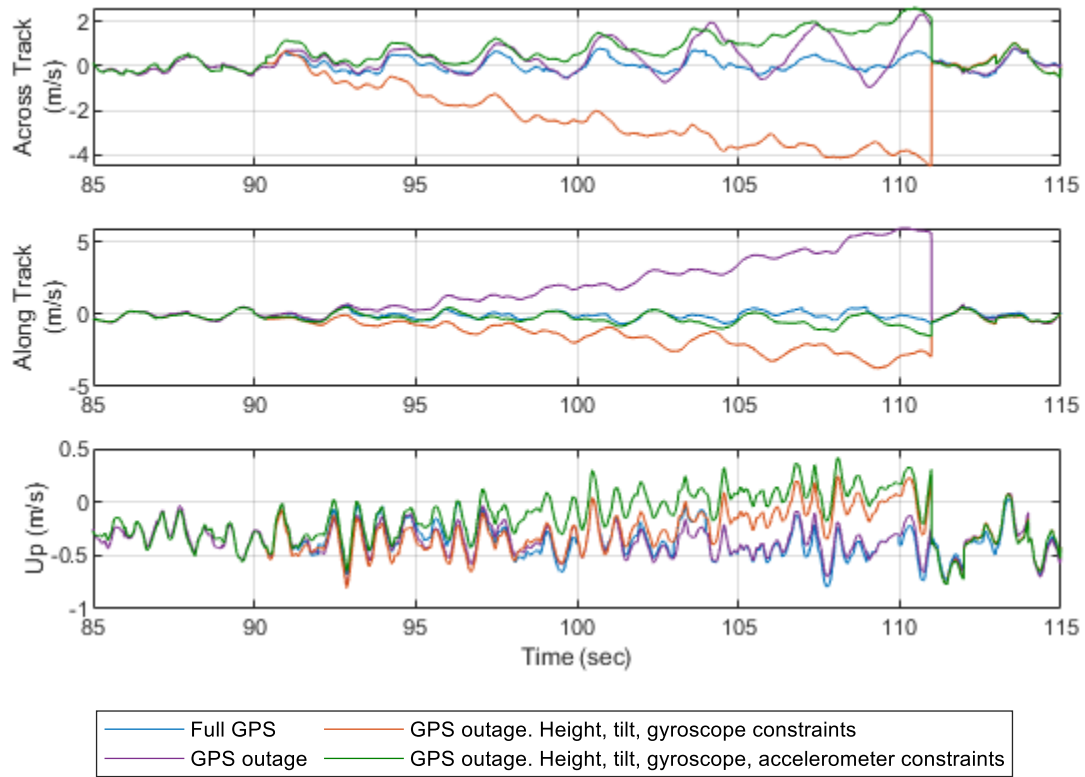


Figure 5.10: Velocity errors of dataset 1 during a GPS outage with and without motion constraints

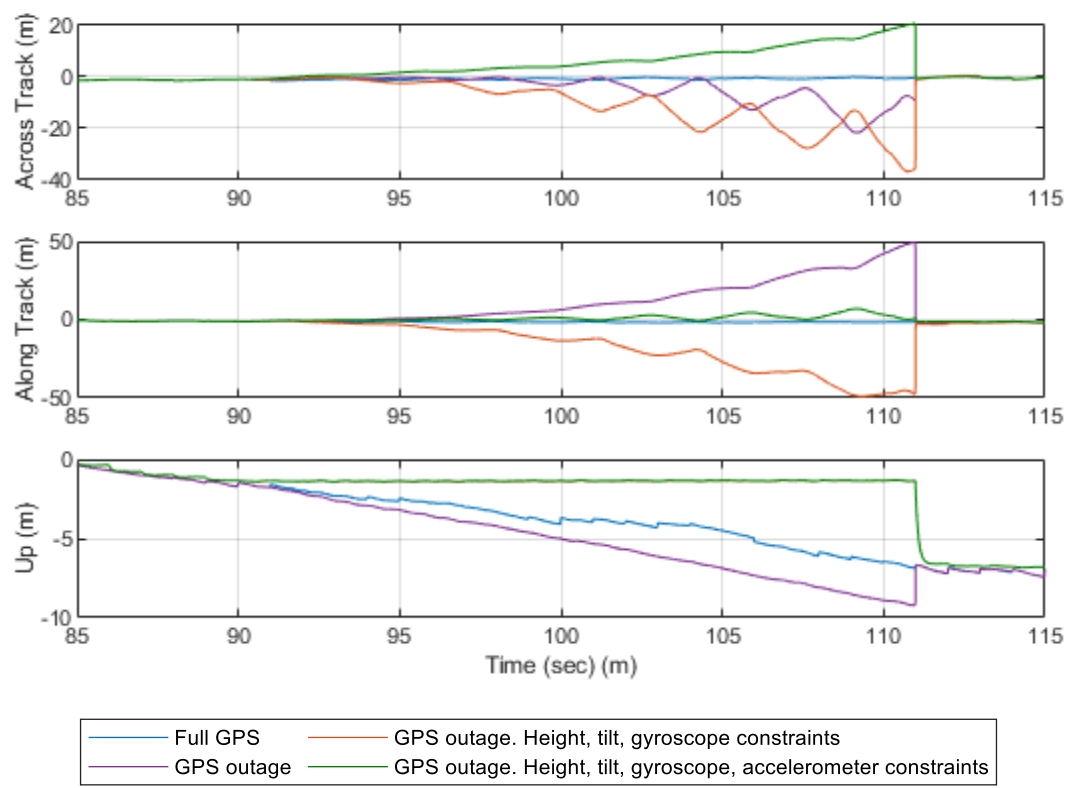


Figure 5.11: Position errors of dataset 1 during a GPS outage with and without motion constraints

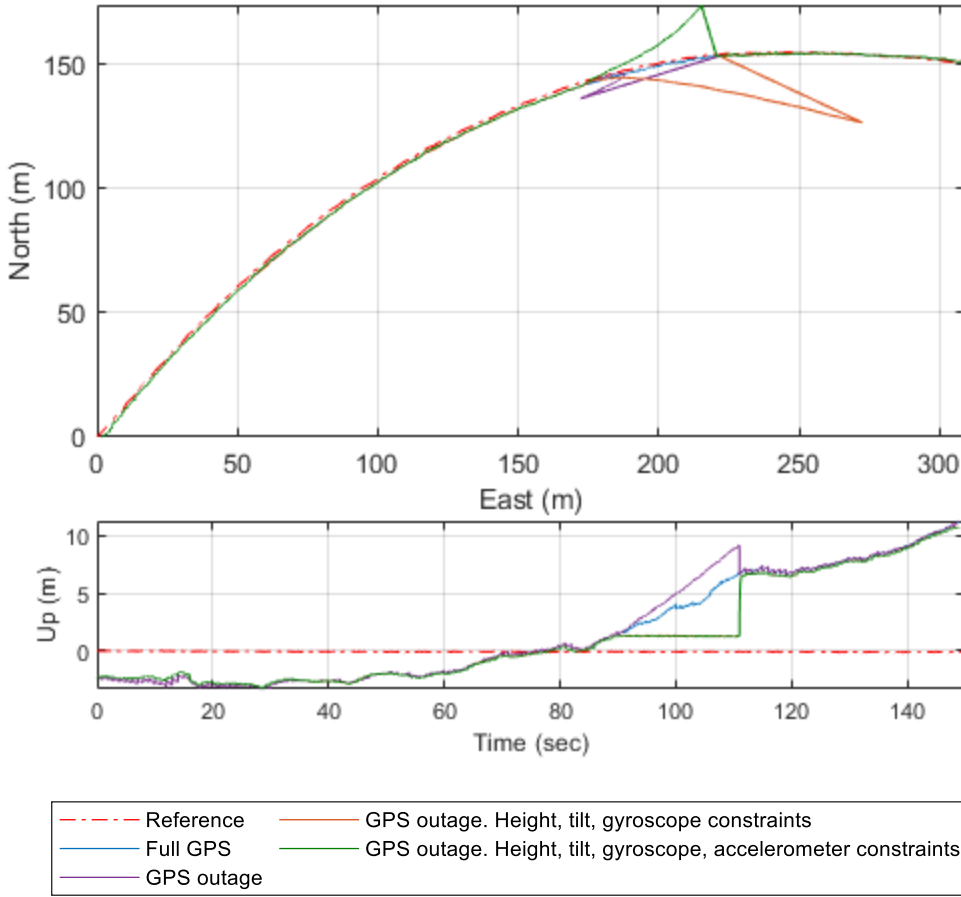


Figure 5.12: Trajectory of dataset 1 and reference solution with and without motion constraints

The final estimated state from the GPS/INS integrated solution is the azimuth which is presented in Figure 5.13. No constraints were applied to the azimuth directly in the GPS/INS configurations, therefore, the error here is similar to those from the solutions presented in Chapter 4. The RMSE of the azimuth for configurations 1, 2, 3, and 4 is 19.630° , 19.031° , 20.286° , and 21.013° respectively. To improve the heading solution, an external heading correction from the GPS solution can be applied. However, the GPS update rate in this project is slower than the IMU update rate, as a result the GPS derived heading does not accurately capture each paddle stroke in the azimuth and a mean GPS azimuth correction would need to be applied to the mean INS solution. The external heading correction is out of scope for this project but can be applied in future work. Therefore, the difference between configurations 1 and 2 with configurations 3 and 4 are a result of the proposed motion constraints on the gyroscope and accelerometer biases.

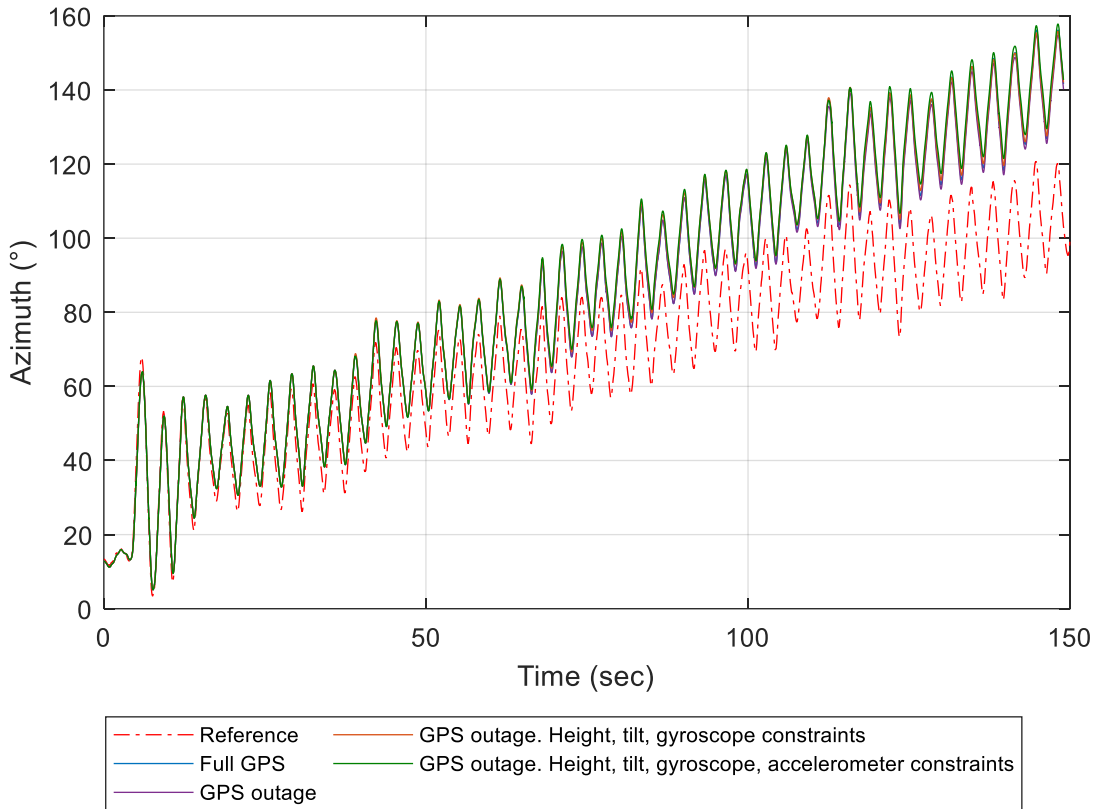


Figure 5.13: Azimuth of dataset 1 and reference trajectory with and without motion constraints

The system performance is a function of both GPS and inertial errors and can be shown using estimated standard deviations. Figure 5.14 shows the estimated position standard deviations computed using the GPS/INS filter during the GPS outage. The horizontal standard deviation during a GPS outage for configuration 4 is better than those for configurations 2 and 3. The vertical standard deviation in the configurations 3 and 4 is small because the height in the solution is constrained. As can be seen with configuration 1, the horizontal and vertical standard deviations are small because every GPS update corrects and improves the uncertainty of the INS solution.

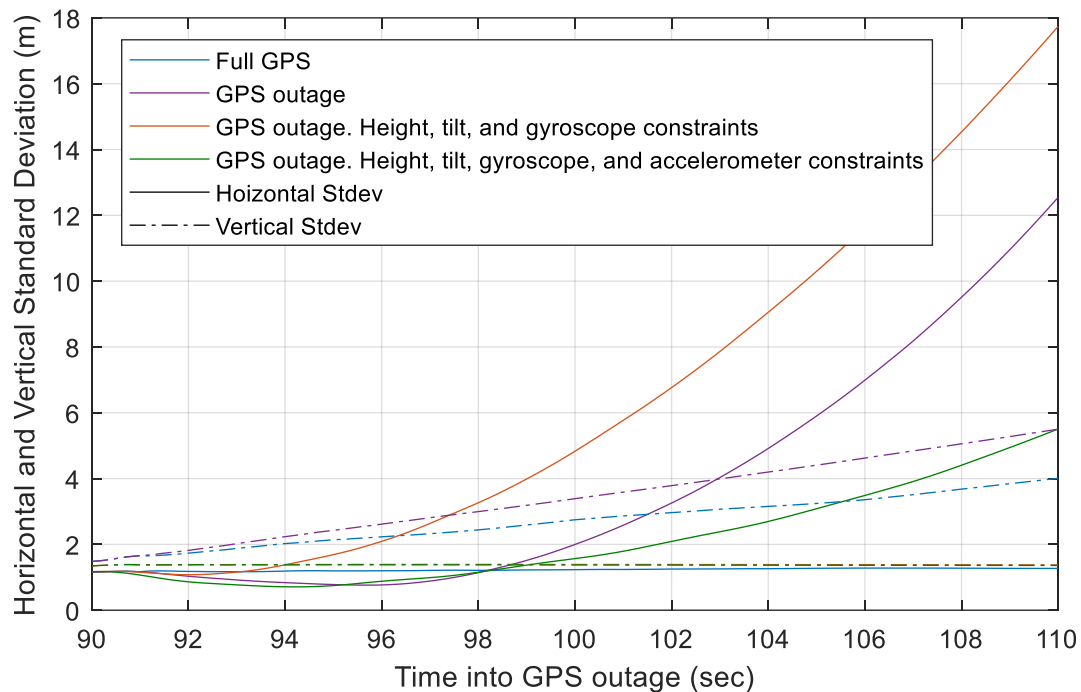


Figure 5.14: Estimated standard deviations of horizontal and vertical positions of dataset 1 during a GPS outage with and without motion constraints

In summary, the use of the proposed motion constraints specific to a strapdown kayak system will reduce the INS drift and improve the amount the amount of time the solution is reliable into a GPS outage. Figure 5.15 displays the overall horizontal and vertical position errors during a GPS outage on dataset 1.

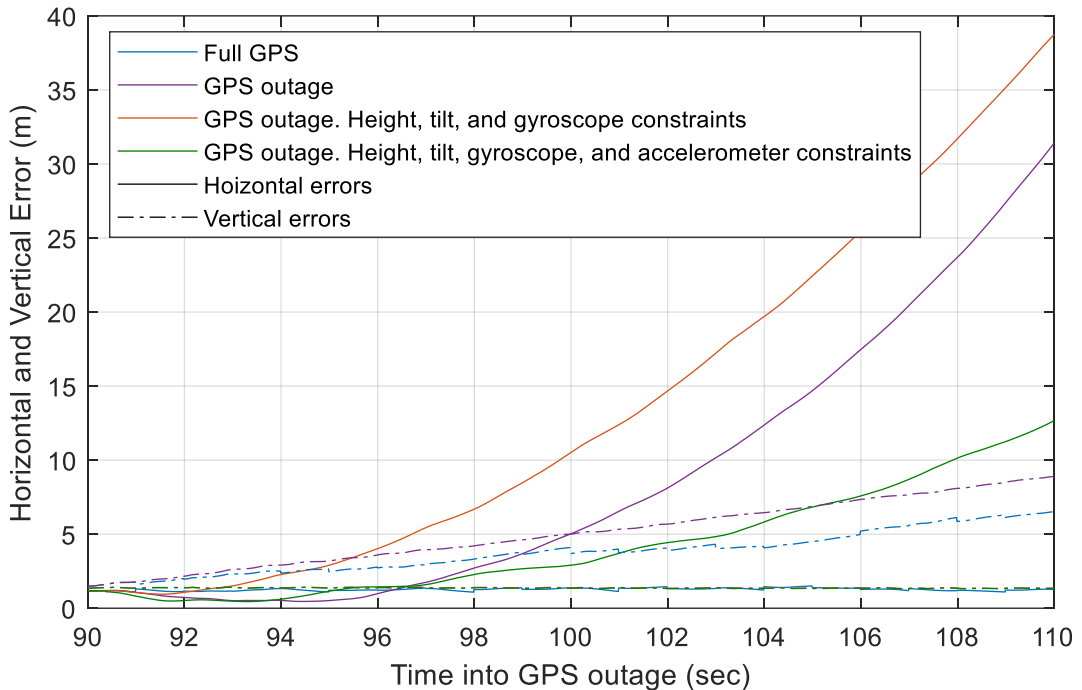


Figure 5.15: Horizontal and vertical position errors of dataset 1 during a GPS outage with and without motion constraints

The results presented here illustrate that utilizing the motion of the kayak to constrain the height, gyroscope bias, tilt angle offsets, and accelerometer bias increases the accuracy of the INS and improves the navigation solution.

5.3 Summary of Results

The analysis of the previous section demonstrated the improvement that the application of motion constraints has on the navigation solution in the event of a GPS outage. These motion constraints were also tested on datasets 2-4 to confirm the validity of the proposed kayak motion constraints for different runs and environments. Selected results from these datasets are presented here and full results can be found in Appendix C. To provide a fair comparison across all datasets, each run has a simulated 20 second GPS outage occur from 90 – 110 seconds in a 150 second total run.

Dataset 2 is most similar to dataset 1 presented above. The differences between these two datasets occur because the smartphone was detached and reattached between the two runs. The cyclic,

mostly uniform roll in Figure 5.6 indicate flat water and continuous paddling through most of the run. As with dataset 1, dataset 2 displays a misaligned or gyroscope error in the unconstrained tilt angles that has been mitigated in the constrained angles. However, these motion constraints have contributed to more errors in the heading of the solution. The horizontal and vertical position errors of this dataset are shown in Figure 5.17 with an improved navigation solution in the GPS outage with motion constraints.

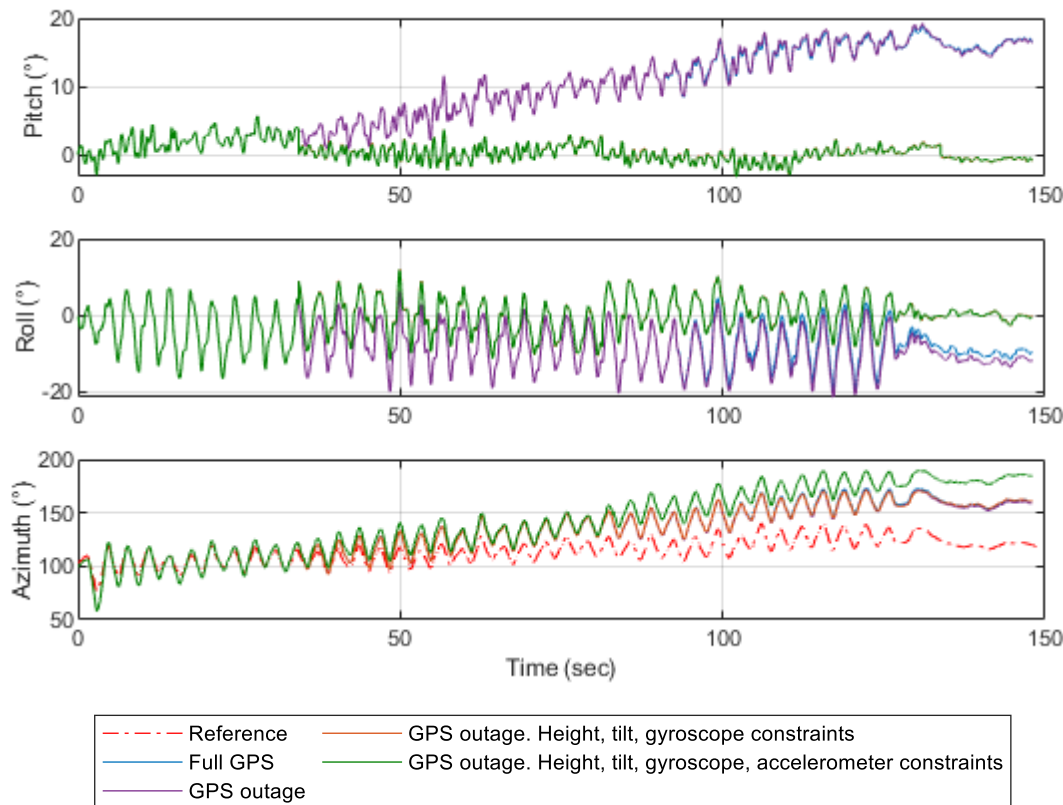


Figure 5.16: Attitude of dataset 2 with and without motion constraints

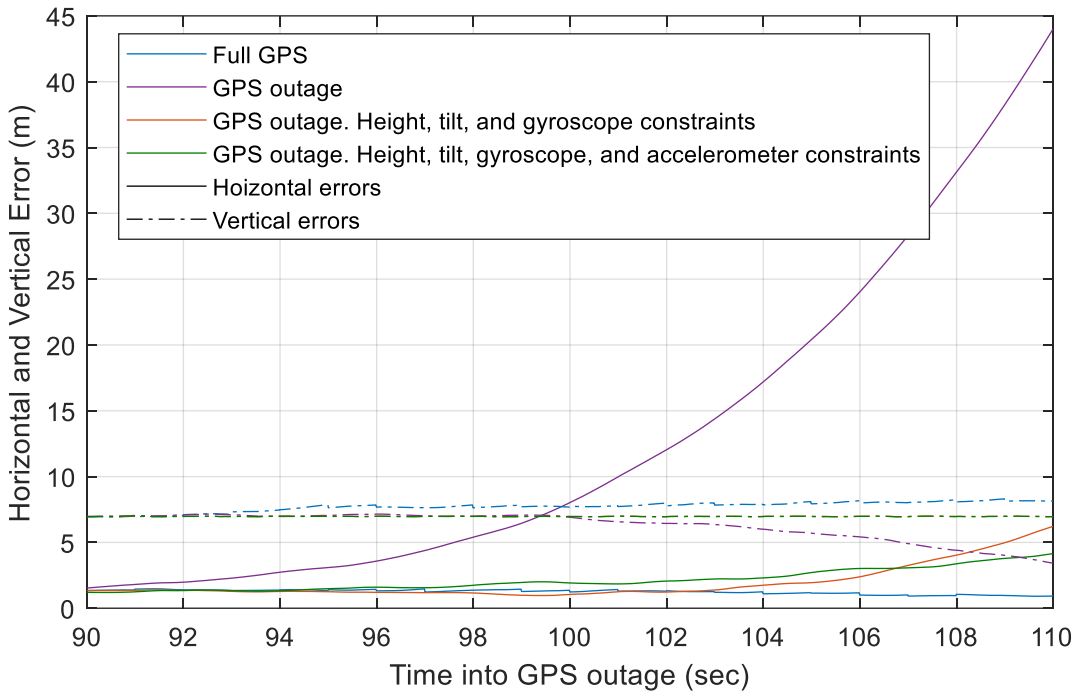


Figure 5.17: Horizontal and vertical position errors of dataset 2 during a GPS outage with and without motion constraints

Dataset 3 provides a little variation in the uniformity of paddling throughout the entirety of the run. In this dataset, the kayaker stopped paddling in the middle of the run than resumed after 40 seconds; this is shown in Figure 5.18. The motion constraint assumption that the tilt angles should not deviate from a centroid around zero still holds true in this case. As with the previous datasets, the errors displayed in Figure 5.19 show an improvement in the navigation solution during a GPS outage with motion constraints.

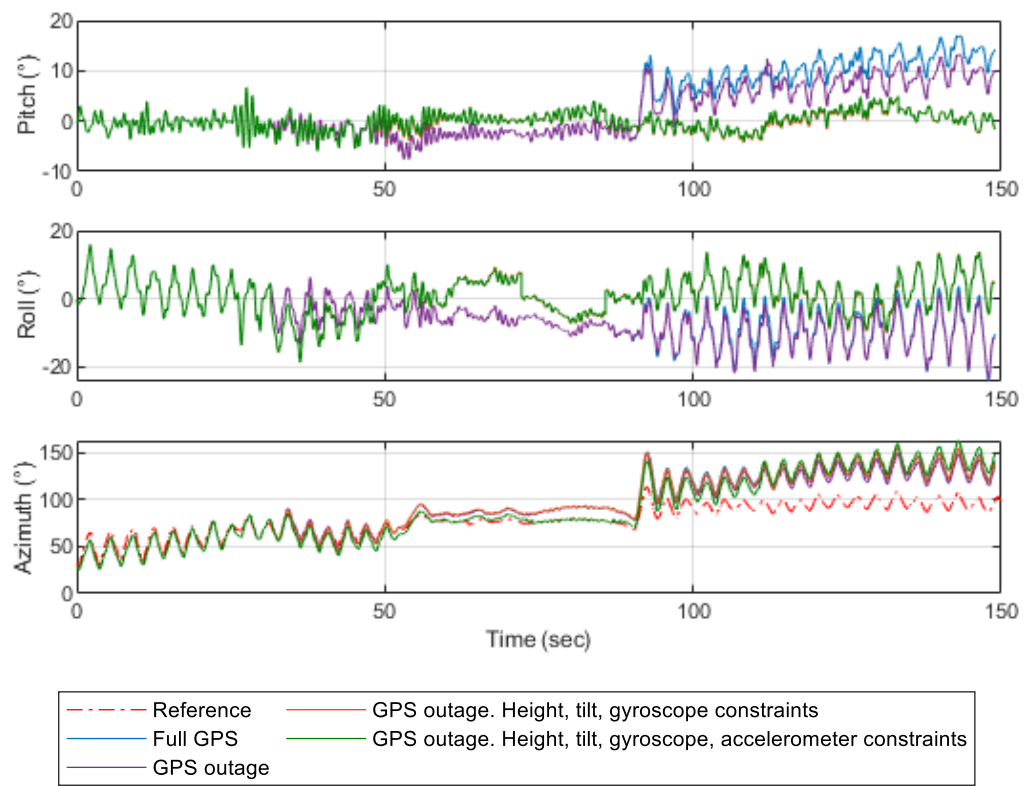


Figure 5.18: Attitude of dataset 3 with and without motion constraints

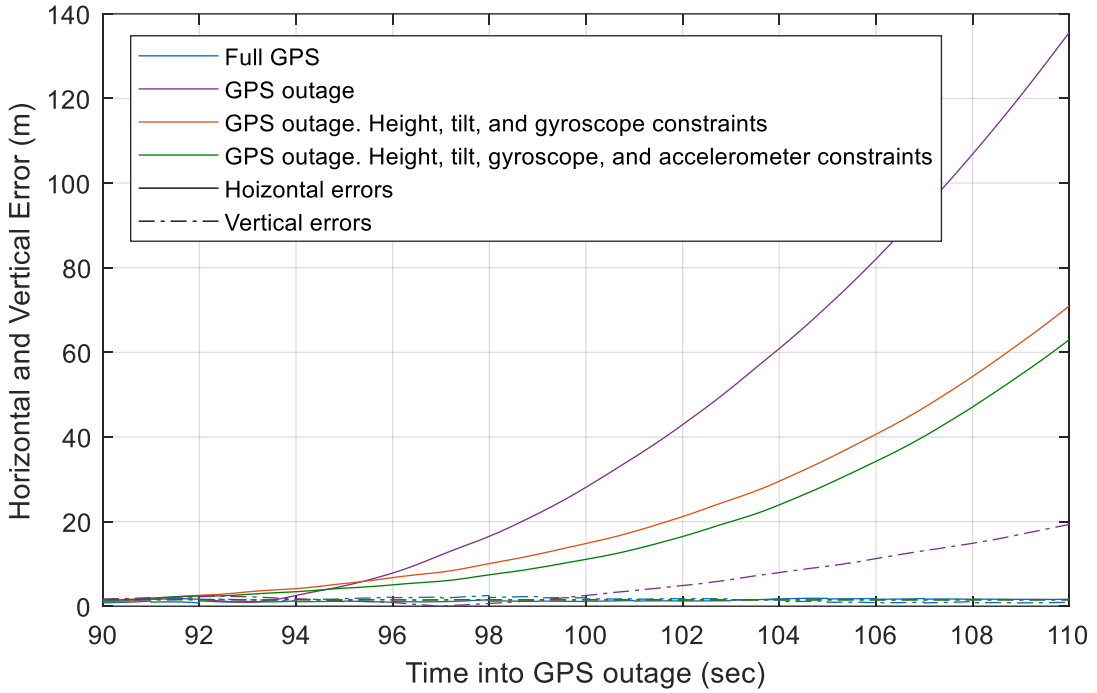


Figure 5.19: Horizontal and vertical position errors of dataset 3 during a GPS outage with and without motion constraints

The final dataset tests the motion constraints on a rough, unpredictable, turbulent river. Figure 5.20 displays the attitude angles of the kayak throughout dataset 4. As seen here, the first 20 seconds of this data is on calm water which is shown by the similar data trends of the roll and azimuth angles displaying a periodic waveform that was also demonstrated in the prior 3 datasets. Following the first 20 seconds, the attitude angles become random due the river rapids causing the kayak to move erratically. The proposed motion constraints for kayaking that the tilt angles are centered around zero are still valid for this dataset. However, more noise is present in these angles which can skew the IMU measurement bias estimates as opposed an easily tracked trend as illustrated by the previous datasets. The tilt angles in configurations 3 and 4 in shown Figure 5.20, although are closer to the true orientation of the kayak, still contain an alignment error because they are not a smooth linear path. Unlike datasets 1-3, the proposed motion constraints improved the heading of the solution and corrected the divergence shown at ~125 seconds.

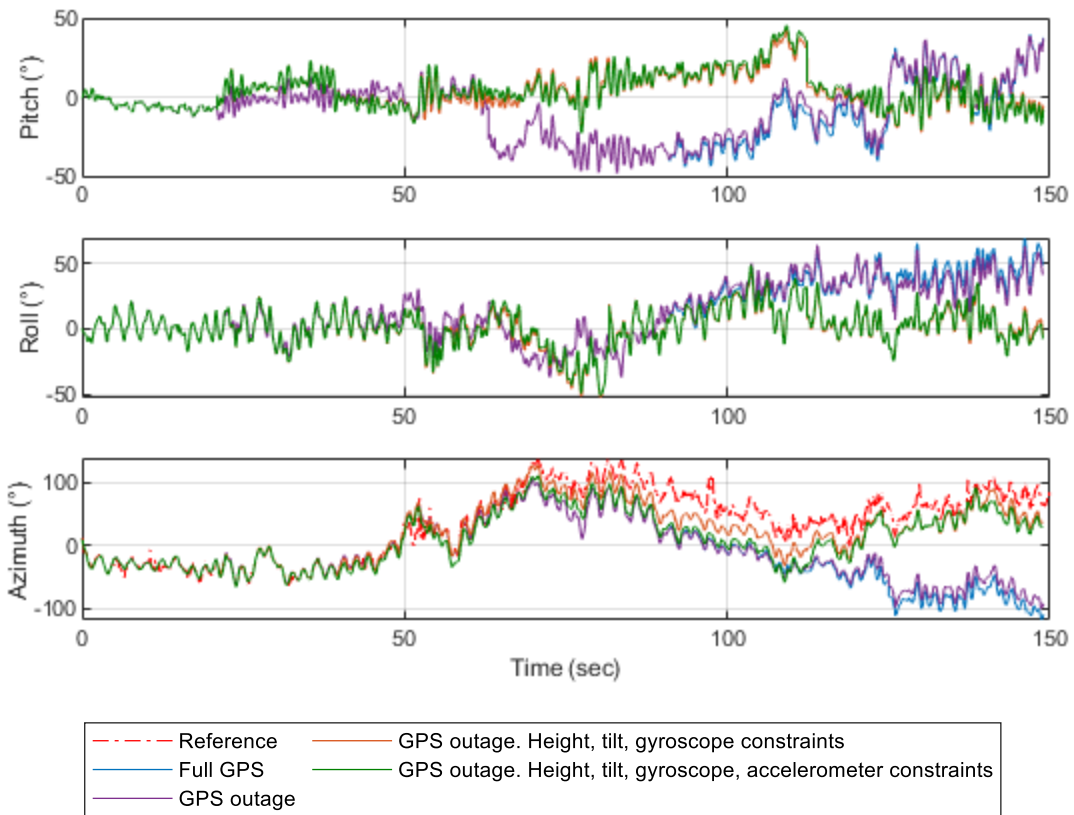


Figure 5.20: Attitude of dataset 4 with and without motion constraints

However, even with these constraints significant position error still exists in the horizontal direction during a GPS outage. Figure 5.21 shows the results of these errors and configuration 2 reaches an error of over 500 metres and configurations 3 and 4 with constraints applied reduce these errors to ~250 metres.

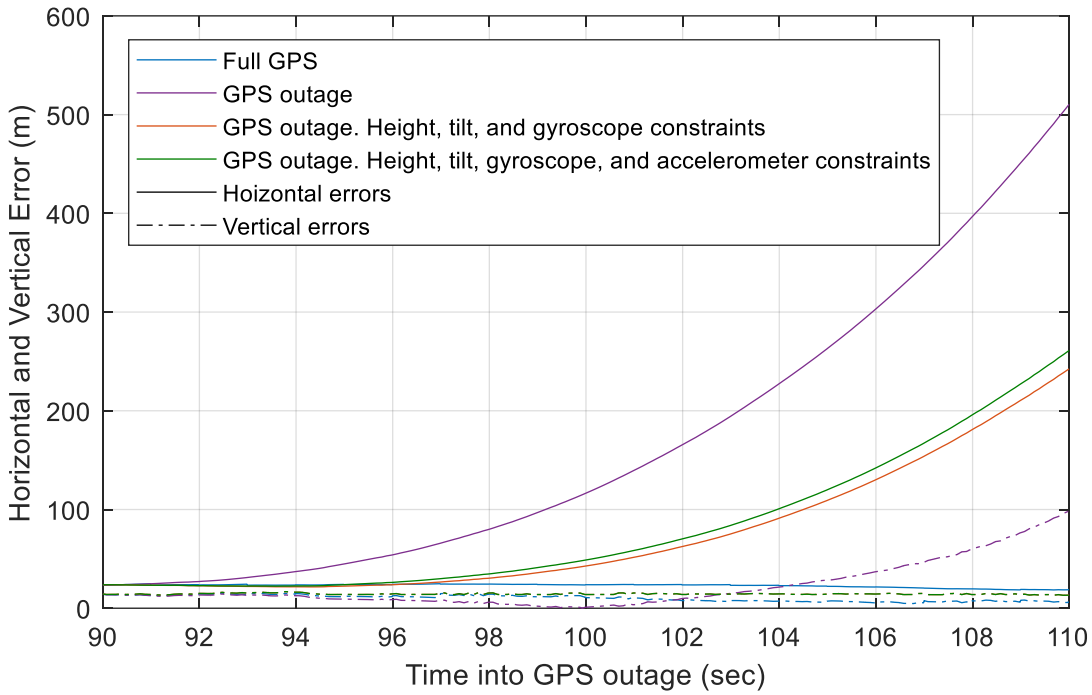


Figure 5.21: Horizontal and vertical position errors of dataset 4 during a GPS outage with and without motion constraints

A summary of the position errors after 20 seconds of a GPS outage for all datasets is provided in Table 8. The proposed motion constraints of height, gyroscope bias, tilt angle offset, and accelerometer bias improved the navigation solution in all datasets.

Table 8: Summary of GPS/INS navigation errors 20 seconds into GPS outage

Dataset	Constraints	Across	Along	Up	3D
1	None	-14.127	-42.103	-8.903	26.150
	All	17.654	3.087	-1.343	10.376
2	None	-7.330	-34.505	-11.674	35.967
	All	25.794	11.691	-6.889	5.255
3	None	-48.640	185.447	19.337	111.251
	All	-34.466	-82.155	-1.507	51.444
4	None	-687.400	-219.773	98.568	420.529
	All	-347.428	-124.878	-13.240	213.288

The same conclusions are reflected in Table 9 which present the root mean square errors (RMSE) of the full datasets which includes a 20 second GPS outage. The along, up, and 3D RMSE benefitted from the motion constraints showing less error. However, the across track direction from dataset 1 resulted in a larger error than the configuration with no constraints applied. This could be due to the abrupt change in the IMU alignment causing sudden spikes in the velocity and position solutions.

Table 9: Summary of GPS/INS navigation position RMSE of full datasets with 20 second GPS outage (metres)

Dataset	Constraints	Across	Along	Up	3D
1	None	2.792	7.316	5.019	9.301
	All	3.315	1.948	4.428	5.864
2	None	1.998	10.671	6.442	12.624
	All	1.514	1.761	6.331	6.932
3	None	10.959	32.459	3.753	34.464
	All	4.670	14.522	1.740	15.353
4	None	113.263	68.198	25.434	134.634
	All	55.982	41.260	21.382	72.757

Table 10 shows the results of the heading solutions with and without constraints applied to datasets containing a GPS outage. Errors still exists in all solutions because the heading itself was not updated or constrained with additional measurements or motion updates. Dataset 1-3 did not improve attitude, however, significant improvement was noted in dataset 4.

Table 10: Summary of GPS/INS navigation azimuth RMSE of full datasets with 20 second GPS outage

Dataset	Constraints	Azimuth RMSE (degrees)
1	None	19.031
	All	21.013
2	None	22.099
	All	33.994
3	None	19.787
	All	23.030
4	None	68.598
	All	32.513

In terms of velocity and position errors, the use of height, gyroscope bias, and tilt angle offset constraints improved the solution. However, these constraints were not reliable for all datasets due to the GPS-estimated accelerometer biases accounting for gyroscope errors. The accelerometer biases were then unfitting of the IMU alignment once the gyroscope errors were updated. Therefore, the proposed updates to the accelerometer biases in conjunction with the gyroscope bias and tilt angle constraints improved the reliability of these motion constraints. Overall, the INS drift during a GPS outage was reduced with the proposed kayak motion constraints thereby improving the navigation solution.

Chapter 6: Conclusions and Recommendations

The recent accessibility of raw GPS measurements from an Android device coupled with the rising demand for handheld navigation and tracking for consumer applications has created an opportunity to test the capabilities of a smartphone tracking system for kayaking. Therefore, the objective of this thesis was to develop a system to continuously track a kayak through a river using a low-cost, smartphone GPS/INS based positioning system.

To evaluate the solution, smartphone and reference data was collected on four different runs. Three of these datasets were collected on calm waters with good satellite visibility and the fourth dataset was on turbulent waters with poorer satellite visibility. A Google Pixel 4 smartphone was mounted rigidly to the deck of a kayak and contains a 3-axis accelerometer, 3-axis gyroscope, and a GPS receiver. The reference solution used in this work consisted of three commercial grade GNSS receivers. Two of these receivers were mounted to the bow and stern respectively to provide an azimuth solution and additional redundancy, the third was used as a base station for a double-difference solution.

Using the smartphone data and reference trajectory, a comparison of different navigation strategies was performed to assess the performance, reliability, and feasibility for of a smartphone solution for kayaking. An assessment of the GPS-only navigation solution using an extended Kalman filter was conducted. However, GPS-only navigation can be intermittent or unreliable due to satellite signal outages in environments such as river canyons, therefore an inertial system was integrated to provide a continuous solution during these outages. In particular, closed loop loosely coupled and tightly coupled GPS/INS algorithms were evaluated and compared. It was found that low-cost inertial sensors, such as those found in a Google Pixel 4, were incapable of providing an accurate solution for a long period of time during GPS outages due to the accumulation of sensor errors. Therefore, in the event of a GPS outage, the traditional LC and TC strategies became unreliable. To overcome this, kayak-specific motion constraints were proposed, implemented, and evaluated in a LC GPS/INS filter with the objective of improving the accuracy of the navigation solution during GPS outages. The following sections present the major conclusions of these different navigation configurations followed by recommendations for future work on this project.

6.1 Conclusions

The results presented here are compared to the reference solution which is of higher accuracy than the solution derived from the smartphone. The following summarize the results collected from the actual data:

- A total of four datasets were collected in this project, dataset 1-3 was in a river with calm water and open-sky conditions, and dataset 4 was in a river with turbulent waters and tall canyons. Datasets 1-3 continually tracked 7-8 satellites while dataset 4 discontinuously tracked a few satellites.
- The GPS-only EKF solution resulted in meter-level accuracy for dataset 1-3 and dataset 4 resulted in significantly worse accuracy due to the turbulent environment and loss of satellite signals. The 3D RMSE was 5.561, 2.156, 6.725, and 21.743 metres for datasets 1, 2, 3, and 4 respectively.
- The GPS/INS integrated solution using both LC and TC filters were compared using dataset 1. In ideal circumstances with complete satellite coverage, both solutions performed similar with a 3D RMSE of 5.262 and 5.191 metres for the LC and TC systems respectively. The TC filter provided a more optimistic solution with a smaller standard deviation because of the ability to smooth GPS measurement error in one filter.
- During complete simulated data outages, the LC implementation outperformed the TC filter in terms of positioning errors. However, both INS solutions drifted significantly with a horizontal RMSE of 44 and 82 metres for the LC and TC respectively after 20 seconds of no GPS updates.
- Positioning accuracy of the TC filter was better than the LC filter in simulated GPS-challenged environments where only a few satellites were available. The horizontal RMSE was 4 metres in the TC filter after 20 seconds with partial satellite coverage. This is because a TC filter can utilize a few satellites (as few as two) to provide a GPS update whereas the LC filter requires a minimum number of 4 satellites.

Both LC and TC solutions degrade rapidly in the event of a complete GPS outage due to the poor performance of the inertial solution. Motion constraints that have been used in other applications to improve the inertial solution require the host vehicle to have stationary periods of time to apply zero updates or non-holonomic constraints. However, the movement of a kayak is a non-stationary.

Therefore, new kayak-specific motion constraints were proposed to mitigate the INS error growth and improve the overall solution. These constraints are listed below.

- A height constraint was applied based on the assumption that the height fluctuation of the kayak on the water varies minimally over a small interval of time. A constant value of height was derived from a prior, reliable GPS measurement and used as a measurement update between GPS updates and during GPS outages.
- A gyroscope bias constraint was used based on the assumption that a kayak does not roll over or pitch up and down severely. This bias constraint was derived from the drift of the tilt angles of the kayak. The paddle stroke of a kayaker creates a cyclic periodic motion in the roll; therefore, the gyroscope bias constraint was applied after a period of time that encompassed full, completed cycles of the roll so as not to skew the gyroscope bias estimate with half a paddle stroke cycle.
- A tilt angle constraint was applied based on the assumption that the pitch and roll of a kayak are centered around zero. A tilt angle offset can occur if the entirety of the signal contains an offset. This update was applied at the same time as the gyroscope bias.
- Finally, an accelerometer bias constraint was used in conjunction with the gyroscope bias constraint. The orientation of the IMU is determined by the gyroscope measurements and corresponding gyroscope bias. Overtime, the GPS/INS system estimates an accelerometer bias erroneously to compensate for a misaligned gyroscope. Therefore, the accelerometer bias must be adjusted to incorporate the changes in the IMUs orientation with a gyroscope bias update. The accelerometer bias is estimated from the newly computed tilt angles and applied as an additional motion constraint on the system.

These proposed motion constraints were applied to the GPS/INS LC filter. Overall, the integrated system with these constraints applied showed better performance than the solution without motion constraints. Details of the main conclusions are:

- The gyroscope bias and tilt angle constraint corrected the roll and pitch angles (orientation) of the kayak to the expected values oscillating around zero.
- The application of height, gyroscope bias, and tilt angle constraints resulted in a greater error in the across track direction in the position and velocity during a GPS outage than in the traditional filter without these constraints applied. This growth in error is a result of an

incorrectly GPS-estimated accelerometer bias that was overcompensating for a misaligned gyroscope. The along track position and velocity drift during a GPS outage was comparable with and without these constraints applied, there was no improvement in the solution.

- No constraints in this project were applied directly to the azimuth itself, therefore, there were very minimal differences in the azimuth solution when comparing the traditional LC filter with the motion constrained LC filter.
- The use of all four kayak-specific motion constraints significantly improved the inertial solution during a GPS outage. The horizontal errors improved from 31.077 to 12.538 metres and the vertical errors improved from 8.874 to 1.342 metres from the traditional LC filter after a 20 second GPS outage during dataset 1. The horizontal and vertical uncertainties also improved in the solution with motion constraints applied.
- The motion constraints were applied to datasets 1-4 with a simulated 20 second GPS outage in each to further validate the proposed kayak-specific motion constraints. The 3D RMSE improved the traditional filter from ~9 to 6 metres, 13 to 7 metres, 34 to 15 metres, and 134 to 73 metres for dataset 1, 2, 3, and 4 respectively.

The results indicate that the velocity and position errors during a GPS outage in a LC filter were improved with the application of the proposed kayak-specific motion constraints. It was found that an accelerometer bias constraint is necessary in conjunction with the gyroscope bias constraint to account for the change in the IMUs alignment. The proposed kayak-specific motion constraints significantly improved the LC GPS/INS navigation solution, particularly during a GPS outage.

This project explores the potential of using a smartphone to track a kayak through a river. The positional accuracy during complete satellite coverage and GPS outages with motion constraints applied was of metre-level accuracy on a flat, calm river. Therefore, the current navigation solution is suitable for recreational kayakers navigating on calm waters with frequent open sky conditions for GPS updates.

6.2 Recommendations for Future Work

The following recommendations for future work can be made based on the conclusions of this research:

- This work only utilized measurements from the GPS L1 frequency because it is the most commonly available on the majority of Android devices. Further work can be explored using multi-constellations and multi-frequencies to investigate the impact of these additional measurements on the navigation solution.
- Carrier phase measurements could also be incorporated into the solution for additional measurements. This project only used pseudorange and Doppler measurements due to the rate that cycle slips occur in low-cost receivers. Further advances in low-cost receivers and ambiguity resolution solutions could make the use of phase measurements feasible in dynamic applications.
- Additional inertial sensor error states like scale factors or non-orthogonality errors can be added into the GPS/INS filter to examine the impact these errors would have on the proposed motion constraints and solution.
- External heading aiding can be implemented to further improve the solution. Heading aiding can be derived from a GPS, magnetometer, or additional sensor. Due to the cadence of a kayak in the heading, careful consideration should be given when applying a heading update from a sensor with a slower update rate than the IMU. Each paddle stroke causes the kayak to oscillate from side-to-side and a mean heading constraint would need to be applied at times when the kayak is parallel to the forward direction.
- The proposed motion constraints can be applied in a sliding window scheme. This project only applies the constraints after a set length of time determined by the number of paddle strokes completed. However, the application of a sliding window would allow the constraints to be applied more frequently and to past measurements to analyze whether this would provide any impact to the solution.
- This project only applied the proposed motion constraints to the LC configuration, these motions constraints can be applied and analyzed with the TC model as well.
- Additional sources of updates such as map matching or coordinate update techniques can be investigated to determine the impact it would have on the solution.

- The cadence of the kayak and paddle stroke can be used in a pedestrian dead reckoning solution. Analysis can be conducted on displacement and velocity based upon each paddle stroke and integrated into the GPS/INS filter. However, factors such as river water speed, efficiency of the kayak, gradient change of the river, and power of each paddle stroke will influence the dead reckoning algorithm and would need to be considered and analyzed.

References

- Aggarwal, P., Syed, Z., & El-Sheimy, N. (2010). *MEMS-Based Integrated Navigation*. Artech House. <http://ebookcentral.proquest.com/lib/ucalgary-ebooks/detail.action?docID=587845>
- Aggrey, J., Bisnath, S., Naciri, N., Shinghal, G., & Yang, S. (2020). Multi-GNSS precise point positioning with next-generation smartphone measurements. *Journal of Spatial Science*, 65(1), 79–98. <https://doi.org/10.1080/14498596.2019.1664944>
- Aitken, D. A., & Neal, R. J. (1992). An On-Water Analysis System for Quantifying Stroke Force Characteristics during Kayak Events. *International Journal of Sport Biomechanics*, 8(2), 165–173. <https://doi.org/10.1123/ijsb.8.2.165>
- Avrutow, V. V., Buhaiov, D. V., & Meleshko, V. V. (2017). Gyrocompassing mode of the attitude and heading reference system. *2017 IEEE 4th International Conference Actual Problems of Unmanned Aerial Vehicles Developments (APUAVD)*, 134–138. <https://doi.org/10.1109/APUAVD.2017.8308793>
- Babu, S. R., & Wang, J. (2004). *Improving the Quality of IMU-Derived Doppler Estimates for Ultra-Tight GPS/INS Integration*.
- Bahadur, B. (2022). A study on the real-time code-based GNSS positioning with Android smartphones. *Measurement*, 194, 111078. <https://doi.org/10.1016/j.measurement.2022.111078>
- Bakuła, M., Uradziński, M., & Krasuski, K. (2022). Performance of DGPS Smartphone Positioning with the Use of P(L1) vs. P(L5) Pseudorange Measurements. *Remote Sensing*, 14(4), 929. <https://doi.org/10.3390/rs14040929>

- Bao, Z., Lu, G., Wang, Y., & Tian, D. (2013). A Calibration Method for Misalignment Angle of Vehicle-mounted IMU. *Procedia - Social and Behavioral Sciences*, 96, 1853–1860.
<https://doi.org/10.1016/j.sbspro.2013.08.210>
- Bjerkefors, A., Tarassova, O., Rosén, J. S., Zakaria, P., & Arndt, A. (2018). Three-dimensional kinematic analysis and power output of elite flat-water kayakers. *Sports Biomechanics*, 17(3), 414–427. <https://doi.org/10.1080/14763141.2017.1359330>
- BMI263*. (n.d.). Bosch Sensortec. Retrieved November 22, 2021, from <https://www.bosch-sensortec.com/products/motion-sensors/imus/bmi263/>
- Bochkati, M., Sharma, H., Lichtenberger, C. A., & Pany, T. (2020). Demonstration of Fused RTK (Fixed) + Inertial Positioning Using Android Smartphone Sensors Only. *2020 IEEE/ION Position, Location and Navigation Symposium (PLANS)*, 1140–1154.
<https://doi.org/10.1109/PLANS46316.2020.9109865>
- Brodie, M., Walmsley, A., & Page, W. (2008). Fusion motion capture: A prototype system using inertial measurement units and GPS for the biomechanical analysis of ski racing. *Sports Technology*, 1(1), 17–28. <https://doi.org/10.1002/jst.6>
- Brown, R. G. (2012). *Introduction to random signals and applied Kalman filtering: With MATLAB exercises*. John Wiley.
- Chandra, T. (2019). *Integration of Multiple Low-Cost Wearable Inertial/Magnetic Sensors and Kinematics of Lower Limbs for Improving Pedestrian Navigation Systems* [Unpublished doctoral thesis, University of Calgary]. <http://hdl.handle.net/1880/110877>
- Chang, H.-W., Georgy, J., & El-Sheimy, N. (2015). Cycling dead reckoning for enhanced portable device navigation on multi-gear bicycles. *GPS Solut*, 19(4), 611–621.
<https://doi.org/10.1007/s10291-014-0417-1>

- Chen, B., Gao, C., Liu, Y., & Sun, P. (2019). Real-time Precise Point Positioning with a Xiaomi MI 8 Android Smartphone. *Sensors*, 19(12), 2835. <https://doi.org/10.3390/s19122835>
- Chiang, K.-W., Le, D. T., Duong, T. T., & Sun, R. (2020). The Performance Analysis of INS/GNSS/V-SLAM Integration Scheme Using Smartphone Sensors for Land Vehicle Navigation Applications in GNSS-Challenging Environments. *Remote Sensing*, 12(11), 1732. <https://doi.org/10.3390/rs12111732>
- Cloud, B., Tarien, B., Liu, A., Shedd, T., Lin, X., Hubbard, M., Crawford, R. P., & Moore, J. K. (2019). Adaptive smartphone-based sensor fusion for estimating competitive rowing kinematic metrics. *PLOS ONE*, 14(12), e0225690. <https://doi.org/10.1371/journal.pone.0225690>
- Croft, H., & Ribeiro, D. C. (2013). *Developing and Applying a Tri-axial Accelerometer Sensor for Measuring Real Time Kayak Cadence*. 60. <https://doi.org/10.1016/j.proeng.2013.07.038>
- Daboo, P., & Di Pietra, V. (2019). Single-Baseline RTK Positioning Using Dual-Frequency GNSS Receivers Inside Smartphones. *Sensors*, 19(19), 4302. <https://doi.org/10.3390/s19194302>
- Daboo, P., Di Pietra, V., & Piras, M. (2020). GNSS Positioning Using Mobile Devices with the Android Operating System. *ISPRS International Journal of Geo-Information*, 9(4), 220. <https://doi.org/10.3390/ijgi9040220>
- Dissanayake, G., Sukkarieh, S., Nebot, E., & Durrant-Whyte, H. (2001). The aiding of a low-cost strapdown inertial measurement unit using vehicle model constraints for land vehicle applications. *IEEE Transactions on Robotics and Automation*, 17(5), 731–747. <https://doi.org/10.1109/70.964672>

- Dual-frequency GNSS on Android.* (n.d.). Google Docs. Retrieved May 19, 2022, from
https://docs.google.com/spreadsheets/d/1z6Yt9c4cyev1PB6VWEkbZtJGfoxAQ5UJnHyP24sFwlk/edit?usp=embed_facebook
- Elmezayen, A., & El-Rabbany, A. (2019). Precise Point Positioning Using World's First Dual-Frequency GPS/GALILEO Smartphone. *Sensors*, 19(11), 2593.
<https://doi.org/10.3390/s19112593>
- EU Agency for the Space Programme. (2022). *EUSPA EO and GNSS Market Report* (ISSUE 1). Publications Office of the European Union.
https://www.euspa.europa.eu/sites/default/files/uploads/euspa_market_report_2022.pdf
- European GNSS Supervisory Authority. (2017). *Using GNSS raw measurements on Android devices: White paper*. Publications Office. <https://data.europa.eu/doi/10.2878/449581>
- Falco, G., Einicke, G. A., Malos, J. T., & Dovis, F. (2012). Performance Analysis of Constrained Loosely Coupled GPS/INS Integration Solutions. *Sensors*, 12(11), 15983–16007.
<https://doi.org/10.3390/s121115983>
- Fan, B., Li, Q., & Liu, T. (2018). How Magnetic Disturbance Influences the Attitude and Heading in Magnetic and Inertial Sensor-Based Orientation Estimation. *Sensors*, 18(1), 76. <https://doi.org/10.3390/s18010076>
- Fleming, N., Donne, B., & Fletcher, D. (2012). Effect of Kayak Ergometer Elastic Tension on Upper Limb EMG Activity and 3D Kinematics. *Journal of Sports Science & Medicine*, 11(3), 430–437.
- Fong, W., Ong, S. K., & Nee, A. (2008). Methods for in-field user calibration of an inertial measurement unit without external equipment. *Measurement Science & Technology - MEAS SCI TECHNOL*, 19. <https://doi.org/10.1088/0957-0233/19/8/085202>

- Fortunato, M., Critchley-Marrows, J., Siutkowska, M., Ivanovici, M. L., Benedetti, E., & Roberts, W. (2019). Enabling High Accuracy Dynamic Applications in Urban Environments Using PPP and RTK on Android Multi-Frequency and Multi-GNSS Smartphones. *2019 European Navigation Conference (ENC)*, 1–9.
<https://doi.org/10.1109/EURONAV.2019.8714140>
- Foxlin, E. (2005). Pedestrian tracking with shoe-mounted inertial sensors. *IEEE Computer Graphics and Applications*, 25(6), 38–46. <https://doi.org/10.1109/MCG.2005.140>
- Fu, G. (Michael), Khider, M., & van Diggelen, F. (2020). *Android Raw GNSS Measurement Datasets for Precise Positioning*. 1925–1937. <https://doi.org/10.33012/2020.17628>
- Gao, G., & Lachapelle, G. (2008). A Novel Architecture for Ultra-Tight HSGPS-INS Integration. *J. of GPS*, 7(1), 46–61. <https://doi.org/10.5081/jgps.7.1.46>
- Gelb, A. (1974). *Applied Optimal Estimation*. MIT Press.
- Geng, J., & Li, G. (2019). On the feasibility of resolving Android GNSS carrier-phase ambiguities. *Journal of Geodesy*, 93(12), 2621–2635. <https://doi.org/10.1007/s00190-019-01323-0>
- Godha, S., & Cannon, M. E. (2007). GPS/MEMS INS integrated system for navigation in urban areas. *GPS Solutions*, 11(3), 193–203. <https://doi.org/10.1007/s10291-006-0050-8>
- Grejner-Brzezinska, D. A., Yi, Y., & Toth, C. K. (2001). Bridging GPS Gaps in Urban Canyons: The Benefits of ZUPTs. *NAVIGATION*, 48(4), 216–226. <https://doi.org/10.1002/j.2161-4296.2001.tb00246.x>
- Grewal, M. S. (2001). *Kalman filtering: Theory and practice using MATLAB*. Wiley.
- Grewal, M. S., Weill, L. R., & Andrews, A. P. (2007). *Global positioning systems, inertial navigation, and integration, second edition* (2nd ed.). Wiley.

- Grip, H. F., Fossen, T. I., Johansen, T. A., & Saberi, A. (2015). Globally exponentially stable attitude and gyro bias estimation with application to GNSS/INS integration. *Automatica*, 51, 158–166. <https://doi.org/10.1016/j.automatica.2014.10.076>
- Grochowski, M., Schweigler, M., Alrifae, B., & Kowalewski, S. (2018). A GPS-aided Inertial Navigation System for Vehicular Navigation using a Smartphone. *IFAC-PapersOnLine*, 51(10), 121–126. <https://doi.org/10.1016/j.ifacol.2018.06.247>
- Groves, P. D. (2007). *Principles of GNSS, Inertial, and Multi-sensor Integrated Navigation Systems*. Artech House. <http://ebookcentral.proquest.com/lib/ucalgary-ebooks/detail.action?docID=338782>
- Halvorsen, K., & Olsson, F. (2016). Pose estimation of cyclic movement using inertial sensor data. *2016 IEEE Statistical Signal Processing Workshop (SSP)*, 1–5. <https://doi.org/10.1109/SSP.2016.7551830>
- Hermsen, H. (2013). *Using GPS and Accelerometer Data for Rowing Race Tracking*. /paper/Using-GPS-and-Accelerometer-Data-for-Rowing-Race-Hermsen/d5dc2bc169305028883188f010179234086ed698
- Humphreys, T. E., Murrian, M., Diggelen, F. van, Podshivalov, S., & Pesyna, K. M. (2016). On the feasibility of cm-accurate positioning via a smartphone's antenna and GNSS chip. *2016 IEEE/ION Position, Location and Navigation Symposium (PLANS)*, 232–242. <https://doi.org/10.1109/PLANS.2016.7479707>
- Hunter, A. (2009). Canoe slalom boat trajectory while negotiating an upstream gate. *Sports Biomechanics*, 8(2), 105–113. <https://doi.org/10.1080/14763140902934837>

- International GNSS Service (IGS). (1992). *Daily 30-Second GPS broadcast ephemeris data* [Data set]. Greenbelt, MD, USA: NASA Crustal Dynamics Data Information System (CDDIS). https://doi.org/10.5067/GNSS/GNSS_DAILY_N_001
- Janssen, I., & Sachlikidis, A. (2010). Validity and reliability of intra-stroke kayak velocity and acceleration using a GPS-based accelerometer. *Sports Biomechanics*, 9(1), 47–56. <https://doi.org/10.1080/14763141003690229>
- Kaplan, E. D., & Hegarty, C. J. (2006). *Understanding GPS : principles and applications*. Artech House.
- Kirkko-Jaakkola, M., Collin, J., & Takala, J. (2012). Bias Prediction for MEMS Gyroscopes. *IEEE Sensors Journal*, 12(6), 2157–2163. <https://doi.org/10.1109/JSEN.2012.2185692>
- Kraft, M., & Lewis, C. (1997). *A Generic Approach to Closed Loop, Digital Transducers. 1*.
- Lachapelle, G., & Gratton, P. (2019). GNSS Precise Point Positioning with Android Smartphones and Comparison with High Performance Receivers. *2019 IEEE International Conference on Signal, Information and Data Processing (ICSIDP)*, 1–9. <https://doi.org/10.1109/ICSIDP47821.2019.9173062>
- Lachapelle, G., Gratton, P., Horrelt, J., Lemieux, E., & Broumandan, A. (2018). Evaluation of a Low Cost Hand Held Unit with GNSS Raw Data Capability and Comparison with an Android Smartphone. *Sensors*, 18, 4185. <https://doi.org/10.3390/s18124185>
- Lashley, M., & Bevly, D. M. (2013). Performance Comparison of Deep Integration and Tight Coupling. *Navigation*, 60(3), 159–178. <https://doi.org/10.1002/navi.43>
- Leung, K. T., Whidborne, J. F., Purdy, D., & Barber, P. (2011). Road vehicle state estimation using low-cost GPS/INS. *Mechanical Systems and Signal Processing*, 25(6), 1988–2004. <https://doi.org/10.1016/j.ymssp.2010.08.003>

Li, G., & Geng, J. (2019). Characteristics of raw multi-GNSS measurement error from Google Android smart devices. *GPS Solutions*, 23(3), 90. <https://doi.org/10.1007/s10291-019-0885-4>

Li, M. (2017). The Progress of Biomechanical Researches in Kayaking. *Yangtze Medicine*, 01(01), 30. <https://doi.org/10.4236/ym.2017.11004>

Li, Y., Niu, X., Zhang, Q., Zhang, H., & Shi, C. (2012). An in situ hand calibration method using a pseudo-observation scheme for low-end inertial measurement units. *Measurement Science & Technology - MEAS SCI TECHNOL*, 23. <https://doi.org/10.1088/0957-0233/23/10/105104>

Li, Z., Wang, R., Gao, J., & Wang, J. (2018). An Approach to Improve the Positioning Performance of GPS/INS/UWB Integrated System with Two-Step Filter. *Remote Sensing*, 10(1), 19. <https://doi.org/10.3390/rs10010019>

Loschner, C., Smith, R., & Galloway, M. (2000). INTRA-STROKE BOAT ORIENTATION DURING SINGLE SCULLING. *ISBS - Conference Proceedings Archive*. <https://ojs.ub.uni-konstanz.de/cpa/article/view/2415>

Luo, Y., Yu, C., Xu, B., Li, J., Tsai, G.-J., Li, Y., & El-Sheimy, N. (2019). Assessment of Ultra-Tightly Coupled GNSS/INS Integration System towards Autonomous Ground Vehicle Navigation Using Smartphone IMU. *2019 IEEE International Conference on Signal, Information and Data Processing (ICSIDP)*, 1–6.

<https://doi.org/10.1109/ICSIDP47821.2019.9173292>

Mansoor, S., Bhatti, U. I., Bhatti, A. I., & Ali, S. M. D. (2019). Improved attitude determination by compensation of gyroscopic drift by use of accelerometers and magnetometers. *Measurement*, 131, 582–589. <https://doi.org/10.1016/j.measurement.2018.08.067>

- Massarweh, L., Fortunato, M., & Gioia, C. (2020). Assessment of Real-time Multipath Detection with Android Raw GNSS Measurements by Using a Xiaomi Mi 8 Smartphone. *2020 IEEE/ION Position, Location and Navigation Symposium (PLANS)*, 1111–1122.
<https://doi.org/10.1109/PLANS46316.2020.9110169>
- Mendoza, L. R., & O'Keefe, K. (2021). Periodic Extended Kalman Filter to Estimate Rowing Motion Indoors Using a Wearable Ultra-Wideband Ranging Positioning System. *2021 International Conference on Indoor Positioning and Indoor Navigation (IPIN)*, 1–8.
<https://doi.org/10.1109/IPIN51156.2021.9662564>
- Mertens, J. C., Boschmann, A., Schmidt, M., & Plessl, C. (2018). Sprint diagnostic with GPS and inertial sensor fusion. *Sports Engineering*, 21(4), 441–451.
<https://doi.org/10.1007/s12283-018-0291-0>
- Misra, P., & Enge, P. (2011). *Global positioning system: Signals, measurements, and performance* (2nd ed.). Ganga-Jamuna Press.
- Nakashima, M., Kitazawa, A., Nakagaki, K., & Onoto, N. (2017). Simulation to clarify the effect of paddling motion on the hull behavior of a single kayak in a sprint race. *Sports Engineering*, 20(2), 133–139. <https://doi.org/10.1007/s12283-016-0222-x>
- NGOC, T. T., KHENCHAF, A., & COMBLET, F. (2019). Evaluating Process and Measurement Noise in Extended Kalman Filter for GNSS Position Accuracy. *2019 13th European Conference on Antennas and Propagation (EuCAP)*, 1–5.
- Nieminan, T., Kangas, J., Suuriniemi, S., & Kettunen, L. (2010). An enhanced multi-position calibration method for consumer-grade inertial measurement units applied and tested. *Measurement Science and Technology*, 21, 105204. <https://doi.org/10.1088/0957-0233/21/10/105204>

- Nilsson, J. E., & Rosdahl, H. G. (2016). Contribution of Leg-Muscle Forces to Paddle Force and Kayak Speed During Maximal-Effort Flat-Water Paddling. *International Journal of Sports Physiology & Performance*, 11(1), 22–27.
- Niu, X., Nassar, S., & El-Sheimy, N. (2007). An Accurate Land-Vehicle MEMS IMU/GPS Navigation System Using 3D Auxiliary Velocity Updates. *NAVIGATION*, 54(3), 177–188. <https://doi.org/10.1002/j.2161-4296.2007.tb00403.x>
- Niu, Z., Nie, P., Tao, L., Sun, J., & Zhu, B. (2019). RTK with the Assistance of an IMU-Based Pedestrian Navigation Algorithm for Smartphones. *Sensors*, 19(14), 3228. <https://doi.org/10.3390/s19143228>
- Noureldin, A., Karamat, T. B., & Georgy, J. (2013). *Fundamentals of Inertial Navigation, Satellite-based Positioning and their Integration*. Springer Berlin Heidelberg. <https://doi.org/10.1007/978-3-642-30466-8>
- Parajuli, B. (2020). Performance analysis of different positioning modes in RTKLIB Software. <https://doi.org/10.13140/RG.2.2.20111.61608>
- Park, S., Gil, M.-S., Im, H., & Moon, Y.-S. (2019). Measurement Noise Recommendation for Efficient Kalman Filtering over a Large Amount of Sensor Data. *Sensors (Basel, Switzerland)*, 19(5). <https://doi.org/10.3390/s19051168>
- Petovello, M. G. (2003). Real-time integration of a tactical-grade IMU and GPS for high-accuracy positioning and navigation. PRISM. <https://doi.org/10.11575/PRISM/10182>
- Pixel phone hardware tech specs—Pixel Phone Help*. (n.d.). Retrieved November 22, 2021, from https://support.google.com/pixelphone/answer/7158570?hl=en&ref_topic=7530176#zippy=%2Cpixel
- Rajagopal, S. (2008). Personal dead reckoning system with shoe mounted inertial sensors.

- Rehman, A., Shahid, H., Afzal, M. A., & Bhatti, H. M. A. (2020). Accurate and Direct GNSS/PDR Integration Using Extended Kalman Filter for Pedestrian Smartphone Navigation. *Gyroscopy and Navigation*, 11(2), 124–137.
<https://doi.org/10.1134/S2075108720020054>
- Renkoski, B. M. (2008). *The effect of carouseling on MEMS IMU performance for gyrocompassing applications* [Thesis, Massachusetts Institute of Technology].
<https://dspace.mit.edu/handle/1721.1/51645>
- Robinson, M. G. (2011). *Accelerometry measurements of sprint kayaks: The coaches' new tool.*
- Robustelli, U., Baiocchi, V., Marconi, L., Radicioni, F., & Pugliano, G. (2020). *Precise Point Positioning with single and dual-frequency multi-GNSS Android smartphones*. 10.
- RTKLIB: An Open Source Program Package for GNSS Positioning*. (n.d.). Retrieved June 26, 2021, from <http://gpspp.sakura.ne.jp/rtklib/rtklib.htm>
- Saboury, J. (2019). *Multi-Tap Extended Kalman Filter for a Periodic Waveform with Uncertain Frequency and Waveform Shape, and Data Dropouts* [Doctoral dissertation]. The University of Wisconsin-Milwaukee.
- Sheta, A., Mohsen, A., Sheta, B., & Hassan, M. (2018). Improved Localization for Android Smartphones Based on Integration of Raw GNSS Measurements and IMU Sensors. *2018 International Conference on Computer and Applications (ICCA)*, 297–302.
<https://doi.org/10.1109/COMAPP.2018.8460352>
- Siddakatte, R., Broumandan, A., & Lachapelle, G. (2017). *PERFORMANCE EVALUATION OF SMARTPHONE GNSS MEASUREMENTS WITH DIFFERENT ANTENNA CONFIGURATIONS*. 17.

Skog, I., & Handel, P. (2009). In-Car Positioning and Navigation Technologies—A Survey.

IEEE Transactions on Intelligent Transportation Systems, 10(1), 4–21.

<https://doi.org/10.1109/TITS.2008.2011712>

Snapdragon 855 Mobile Platform. (2018, November 7). Qualcomm.

<https://www.qualcomm.com/products/snapdragon-855-mobile-platform>

Sorenson, H. W. (1970). Least-squares estimation: From Gauss to Kalman. *IEEE Spectrum*, 7(7), 63–68. <https://doi.org/10.1109/MSPEC.1970.5213471>

Spilker Jr., J. J., Axelrad, P., Parkinson, B. W., & Enge, P. (1996). *Global Positioning System: Theory and Applications, Volume I* (P. Axelrad, B. W. Parkinson, P. Enge, & J. J. S. Jr, Eds.). American Institute of Aeronautics and Astronautics.

<https://doi.org/10.2514/4.866388>

Syed, Z. F., Aggarwal, P., Niu, X., & El-Sheimy, N. (2008). Civilian Vehicle Navigation: Required Alignment of the Inertial Sensors for Acceptable Navigation Accuracies. *IEEE Transactions on Vehicular Technology*, 57(6), 3402–3412.

<https://doi.org/10.1109/TVT.2008.921616>

Tan, H., Wilson, A. M., & Lowe, J. (2008). Measurement of stride parameters using a wearable GPS and inertial measurement unit. *Journal of Biomechanics*, 41(7), 1398–1406.

<https://doi.org/10.1016/j.jbiomech.2008.02.021>

Teunissen, P. (1989). *A recursive slippage test for use in state-space*.

<https://espace.curtin.edu.au/handle/20.500.11937/40884>

Teunissen, P. J. G., Khodabandeh, A., & Psychas, D. (2021). A generalized Kalman filter with its precision in recursive form when the stochastic model is misspecified. *Journal of Geodesy*, 95(9), 108. <https://doi.org/10.1007/s00190-021-01562-0>

Titterton, D. H., & Weston, J. L. (2004). *Strapdown Inertial Navigation Technology* (2nd ed.).

Institution of Engineering and Technology.

Topcon TotalCare: Specifications. (n.d.). Retrieved July 21, 2021, from

<http://www.topconcare.com/en/hardware/gnss-receivers/hiper-sr/specifications/>

Vadai, G., Gingl, Z., Mingesz, R., & Makan, G. (2013). Performance estimation of kayak paddlers based on fluctuation analysis of movement signals. *2013 22nd International Conference on Noise and Fluctuations (ICNF)*, 1–4.

<https://doi.org/10.1109/ICNF.2013.6579010>

Vadai, G., Makan, G., Gingl, Z., Mingesz, R., Mellár, J., Szépe, T., & Csamangó, A. (2013). On-water measurement and analysis system for estimating kayak paddlers' performance. *2013 36th International Convention on Information and Communication Technology, Electronics and Microelectronics (MIPRO)*, 131–136.

van Diggelen, F., & Khider, M. (2018). *GPS Measurement Tools* [Java]. Google.

<https://github.com/google/gps-measurement-tools> (Original work published 2016)

Waegli, A., & Skaloud, J. (2009). Optimization of two GPS/MEMS-IMU integration strategies with application to sports. *GPS Solutions*, 13(4), 315–326.

<https://doi.org/10.1007/s10291-009-0124-5>

Wang, G., Bo, Y., Yu, Q., Li, M., Yin, Z., & Chen, Y. (2020). Ionosphere-Constrained Single-Frequency PPP with an Android Smartphone and Assessment of GNSS Observations. *Sensors*, 20(20), 5917. <https://doi.org/10.3390/s20205917>

Wang, W., & Wang, D. (2008). Land vehicle navigation using odometry/INS/vision integrated system. *2008 IEEE Conference on Cybernetics and Intelligent Systems*, 754–759.

<https://doi.org/10.1109/ICCIS.2008.4670839>

- Wang, Z., Zhao, H., Qiu, S., & Gao, Q. (2015). Stance-Phase Detection for ZUPT-Aided Foot-Mounted Pedestrian Navigation System. *IEEE/ASME Transactions on Mechatronics*, 20(6), 3170–3181. <https://doi.org/10.1109/TMECH.2015.2430357>
- Wanninger, L., & Heßelbarth, A. (2020). GNSS code and carrier phase observations of a Huawei P30 smartphone: Quality assessment and centimeter-accurate positioning. *GPS Solutions*, 24(2), 64. <https://doi.org/10.1007/s10291-020-00978-z>
- Welch, G., & Bishop, G. (1995). *An introduction to the Kalman filter*.
- Wells, D., Beck, N., Kleusberg, A., Krakiwsky, E. J., Lachapelle, G., Langley, R. B., Schwarz, K., Tranquilla, J. M., Vanicek, P., Wells, D., Delikaraoglu, D., Kleusberg, A., Krakiwsky, E. J., Lachapelle, G., Langley, R. B., Schwarz, K., Tranquilla, J. M., & Vanicek, P. (1987). Guide to GPS Positioning. *Canadian GPS Assoc.*
- Wen, Q., Geng, J., Li, G., & Guo, J. (2020). Precise point positioning with ambiguity resolution using an external survey-grade antenna enhanced dual-frequency android GNSS data. *Measurement*, 157, 107634. <https://doi.org/10.1016/j.measurement.2020.107634>
- Wu, Q., Sun, M., Zhou, C., & Zhang, P. (2019). Precise Point Positioning Using Dual-Frequency GNSS Observations on Smartphone. *Sensors*, 19(9), 2189. <https://doi.org/10.3390/s19092189>
- Xie, H., & Fedder, G. K. (2003). Integrated Microelectromechanical Gyroscopes. *J. Aerosp. Eng.*, 16(2), 65–75. [https://doi.org/10.1061/\(ASCE\)0893-1321\(2003\)16:2\(65\)](https://doi.org/10.1061/(ASCE)0893-1321(2003)16:2(65))
- Xu, H., Chua, J., Burton, M., Zhang, K., Fuss, F., & Subic, A. (2010). Development of low cost on-board velocity and position measurement system for wheelchair sports. *Procedia Engineering*, 2, 3121–3126. <https://doi.org/10.1016/j.proeng.2010.04.121>

- Xu, K., Li, L., Chen, R., Li, Y., & Huang, Q. (2021). Application of Smartphone based Land Vehicle Navigation. *2021 5th CAA International Conference on Vehicular Control and Intelligence (CVCI)*, 1–5. <https://doi.org/10.1109/CVCI54083.2021.9661130>
- Yan, W., Bastos, L., & Magalhães, A. (2019). Performance Assessment of the Android Smartphone's IMU in a GNSS/INS Coupled Navigation Model. *IEEE Access*, 7, 171073–171083. <https://doi.org/10.1109/ACCESS.2019.2956239>
- Yan, W., Zhang, Q., Wang, L., Mao, Y., Wang, A., & Zhao, C. (2020). A Modified Kalman Filter for Integrating the Different Rate Data of Gyros and Accelerometers Retrieved from Android Smartphones in the GNSS/IMU Coupled Navigation. *Sensors*, 20(18), 5208. <https://doi.org/10.3390/s20185208>
- Yang, C., Guo, J., Geng, T., Zhao, Q., Jiang, K., Xie, X., & Lv, Y. (2020). Assessment and Comparison of Broadcast Ionospheric Models: NTCM-BC, BDGIM, and Klobuchar. *Remote Sensing*, 12(7), 1215. <https://doi.org/10.3390/rs12071215>
- Yazdi, N., Ayazi, F., & Najafi, K. (1998). Micromachined Inertial Sensors. *PROCEEDINGS OF THE IEEE*, 86(8), 20.
- Yong, C. Z., Odolinski, R., Zaminpardaz, S., Moore, M., Rubinov, E., Er, J., & Denham, M. (2021). Instantaneous, Dual-Frequency, Multi-GNSS Precise RTK Positioning Using Google Pixel 4 and Samsung Galaxy S20 Smartphones for Zero and Short Baselines. *Sensors*, 21(24), 8318. <https://doi.org/10.3390/s21248318>
- Zangenehnejad, F., & Gao, Y. (2021). GNSS smartphones positioning: Advances, challenges, opportunities, and future perspectives. *Satellite Navigation*, 2(1), 24. <https://doi.org/10.1186/s43020-021-00054-y>

Zhang, K., Jiao, W., Wang, L., Li, Z., Li, J., & Zhou, K. (2019). Smart-RTK: Multi-GNSS kinematic positioning approach on android smart devices with Doppler-smoothed-code filter and constant acceleration model. *Advances in Space Research*, 64(9), 1662–1674.

<https://doi.org/10.1016/j.asr.2019.07.043>

Zhu, F., Tao, X., Liu, W., Shi, X., Wang, F., & Zhang, X. (2019). Walker: Continuous and Precise Navigation by Fusing GNSS and MEMS in Smartphone Chipsets for Pedestrians. *Remote Sensing*, 11(2), 139. <https://doi.org/10.3390/rs11020139>

Zhu, H., Xia, L., Wu, D., Xia, J., & Li, Q. (2020). Study on Multi-GNSS Precise Point Positioning Performance with Adverse Effects of Satellite Signals on Android Smartphone. *Sensors*, 20(22), 6447. <https://doi.org/10.3390/s20226447>

Appendix A: Raw GNSS and IMU Measurements on Android Smartphones

This section provides a thorough review of raw GNSS and IMU measurements that are available on an Android device as well as the derivation of pseudorange measurements. A more substantiative review can be found in European GNSS Supervisory Authority (2017) along with further resources and open-source software.

Smartphones are each equipped with different receiver chips which provide various capabilities to receive multiple GNSS constellations including BeiDou, Galileo, etc., however, this project uses only GPS as an example of GNSS. The methods described in here are for GPS and can be adapted for other constellations.

API 24, which is used to connect Android applications with mobile sensors, does not provide direct GPS measurements such as pseudorange, carrier phase, and Doppler; however, the raw data logged from the GNSS sensor can be used to calculate these measurements. A list of variables of raw data is summarized here; they are split into a clock class (Table A.1) and a measurement class (Table A.2).

Table A.1: GPS Clock measurements

Field	Description
TimeNanos	Receiver's hardware clock value
FullBiasNanos	Difference between the receiver's clock and true GPS time since 0000Z, January 6, 1980
BiasNanos	Sub-nanosecond of FullBiasNanos
DriftNanosPerSecond	Receivers' clock's drift
HardwareClockDiscontinuityCount	Count of hardware clock discontinuities
LeapSecond	Leap second associated with the clock's time
ChipsetElapsedRealTimeNanos	Time since system boot

Table A.2: GPS measurements

Field	Description
ConstellationType	BeiDou, Galileo, GLONASS, GPS, QZSS, SBAS
Svid	Satellite ID
State	Sync state including Code lock, bit sync, frame sync
ReceivedSvTimeNanos	Received satellite time at the measurement time
ReceivedSvTimeUncertaintyNanos	Error estimate of ReceivedSvTimeNanos
Cn0DbHz	Carrier-to-noise density
TimeOffsetNanos	Time offset if measurements are asynchronous
CarrierCycles	Number of full carrier cycles between the satellite and receiver
PseudorangeRateMetersPerSecond	Pseudorange rate (Doppler)
PseudorangeRateUncertaintyMetersPerSecond	Error estimate of PseudorangeRateMetersPerSecond
AccumulatedDeltaRangeMeters	Valid, Cycle slip, or Loss-of-lock/Reset
AccumulatedDeltaRangeUncertaintyMeters	Carrier phase (accumulated delta range since last channel reset)
AccumulatedDeltaRangeState	Error estimate of AccumulatedDeltaRangeUncertaintyMeters
CarrierFrequencyHz	Carrier frequency of the tracked signal
AgcDb	Automatic Gain Control level

These raw measurements can be used to compute GPS time, pseudorange measurements, and Doppler rate measurements. The GPS reference time is computed in (A.1) using the internal hardware clock and bias to the true GPS time.

$$GPSTime = TimeNanos - (FullBiasNanos + BiasNanos) \quad A.1$$

The GNSS measurement time can be obtained in equation (A.2). It is noted that this is only applicable if there is no discontinuity in the received time.

$$t_{Rx_{GNSS}} = TimeNanos + TimeOffsetNanos - (FullBiasNanos + BiasNanos) \quad A.2$$

The pseudorange is obtained as a function between the received measurement (t_{Rx}) and transmitted time (t_{Tx}), therefore it is important that these times are in the same reference system. The measurement time $t_{Rx_{GNSS}}$ is provided in the GNSS reference system and some receivers may set the default of GNSS time to GPST (GPS time). In addition to aligning the reference system time,

both $t_{Rx_{GNSS}}$ and t_{Tx} are required to be in the same range which is dependant on the tracking status state.

The conversion of $t_{Rx_{GNSS}}$ to $t_{Rx_{GPST}}$ (GPST received time) is dependant upon the amount of time that has passed from the beginning of GPS time. This includes the computation of the GPS week number, day number, and millisecond number illustrated in (A.3).

$$\begin{aligned}
 & weekNumberNanos \\
 &= floor\left(\frac{-FullBiasNanos}{NumberNanoSecondsWeek}\right) \\
 &\quad * NumberNanoSecondsWeek \\
 \\
 & DayNumberNanos \\
 &= floor\left(\frac{-FullBiasNanos}{NumberNanoSecondsDay}\right) \tag{A.3} \\
 &\quad * NumberNanoSecondsDay \\
 \\
 & milliSecondsNumberNanos \\
 &= floor\left(\frac{-FullBiasNanos}{NumberNanoSeconds100Milli}\right) \\
 &\quad * NumberNanoseconds100Milli
 \end{aligned}$$

where:

$floor$ rounds each element to the nearest integer less than or equal to that element

$NumberNanoSeconds$ is the number of nanoseconds within one *Week*, *Day*, and 100 ms

The GNSS received measurement time can then be converted to GPST:

$$t_{Rx_{GPS}} = t_{Rx_{GNSS}} - weekNumberNanos \tag{A.4}$$

The pseudorange is then obtained as a function between the received and transmitted time:

$$\rho = \frac{t_{Rx_{GPS}} - t_{Tx_{GPS}}}{10^9} c \quad A.5$$

where:

ρ is the pseudorange

t_{Tx} is the ReceivedSvTimeNanos (expressed in nanoseconds)

c is the speed of light in a vacuum

The Doppler shift obtained by satellite movement is given by the device as:

$$\dot{\rho} = \text{PseudorangeRateMetersPerSecond} \quad A.6$$

In addition to the raw GNSS measurements, an Android smartphone can collect sensor measurements from the accelerometer, gyroscope, and magnetometer (if available). Table A.3 lists the sensor measurements that can be logged using Google application GNSSLogger (van Diggelen & Khider, 2016/2018).

Table A.3: IMU measurements

Sensor	Field	Description
Accelerometer	UncalAccelXMps2, UncalAccelYMps2, UncalAccelZMps2	Specific force measurement (m/s^2)
	BiasXMps2, BiasYMps2, BiasZMps2	Estimated accelerometer bias (m/s^2)
Gyroscope	UncalGyroXRadPerSec, UncalGyroYRadPerSec, UncalGyroZRadPerSec	Angular rate measurement (rad/s)
	DriftXRadPerSec, DriftYRadPerSec, DriftZRadPerSec	Estimated gyroscope drift (rad/s)
Magnetometer	UncalMagXMicroT, UncalMagYMicroT, UncalMagZMicroT	Magnetic field strength measurement (μT)
	BiasXMicroT, BiasYMicroT, BiasZMicroT	Estimated magnetometer bias (μT)

Appendix B: Conversion of Cartesian and Geodetic Coordinates in the *e*-Frame

Cartesian coordinates (x, y, z) can be converted to curvilinear coordinates (φ, λ, h) in the *e*-frame with the following procedure. Constant parameters for the WGS 84 reference ellipsoid are defined as (Noureldin et al., 2013):

- Semi-major axis: $a = 6378137.0$ m
- Flattening: $f = 1 / 298.257223563$ m

The eccentricity (e) of an ellipsoid is calculated by:

$$e^2 = \frac{a^2 - b^2}{a^2} \quad \text{A.1}$$

Where the semi-minor axis (b) is calculated from:

$$f = \frac{a - b}{a} \quad \text{A.2}$$

To begin, the radius of the parallel (p) and latitude (λ) are calculated in (A.3) and (A.4)

$$p = \sqrt{x^2 + y^2} \quad \text{A.3}$$

$$\lambda = \tan^{-1} \left(\frac{y}{x} \right) \quad \text{A.4}$$

The geodetic latitude is dependant on the prime vertical radius of curvature (N), iterations are used until a convergence is achieved. The following formulas are used in the iteration process until $|N - N_i|$ becomes insignificant.

$$N_k = \frac{a}{\sqrt{1 - e^2 \sin^2(\varphi)}} \quad \text{A.5}$$

$$h_k = \frac{p}{\cos(\phi)_{k-1}} - N_k \quad \text{A.6}$$

$$\varphi = \tan^{-1} \left(\frac{z}{p} \left(1 - \frac{N_k}{N_k + h_k} \right)^{-1} \right) \quad \text{A.7}$$

Finally, the longitude (λ) is calculated as:

$$\lambda = \tan^{-1} \left(\frac{y}{x} \right) \quad \text{A.8}$$

Appendix C: Results of Datasets 2-4

The full results for datasets 2-4 are detailed in this appendix. Specifically focussing on performance of the navigation solution with height, gyroscope bias, tilt angle offset, and accelerometer bias constraints. All datasets have a simulated GPS outage from 90 – 110 seconds and a closeup of the velocity and position errors during this outage is provided. A legend of each configuration of constraints applied is shown in Figure C.1.

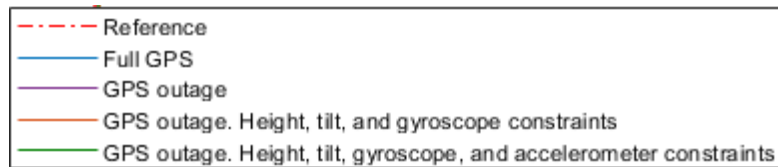


Figure C.1: Result configurations of updates

C.1 Dataset 2 Results

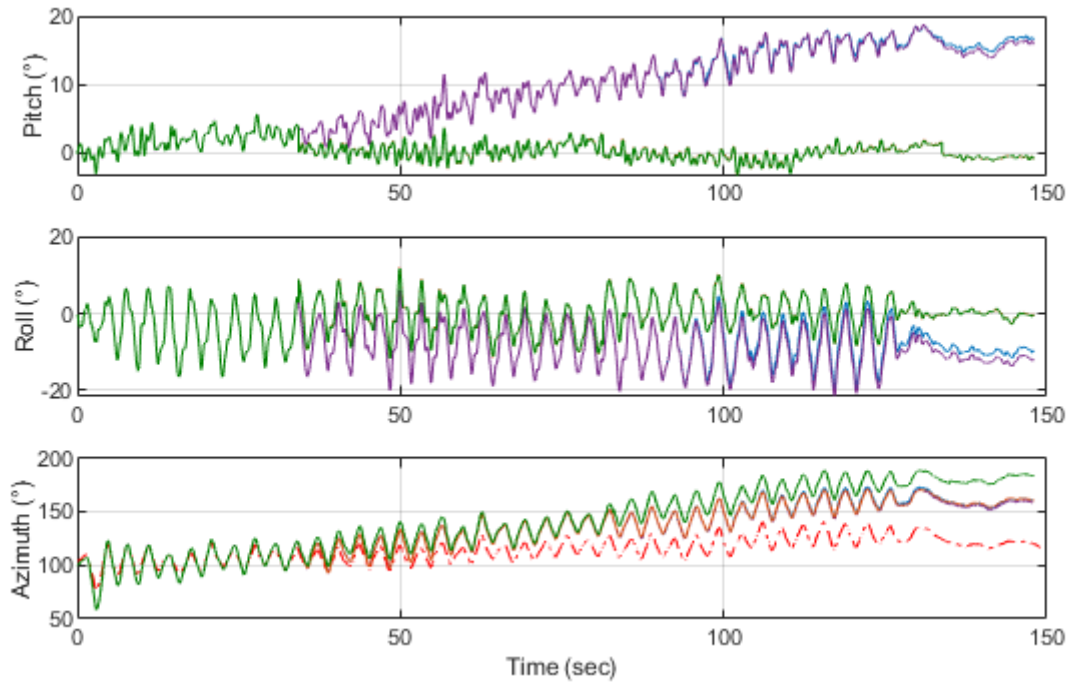


Figure C.2: Dataset 2 attitude with and without motion constraints

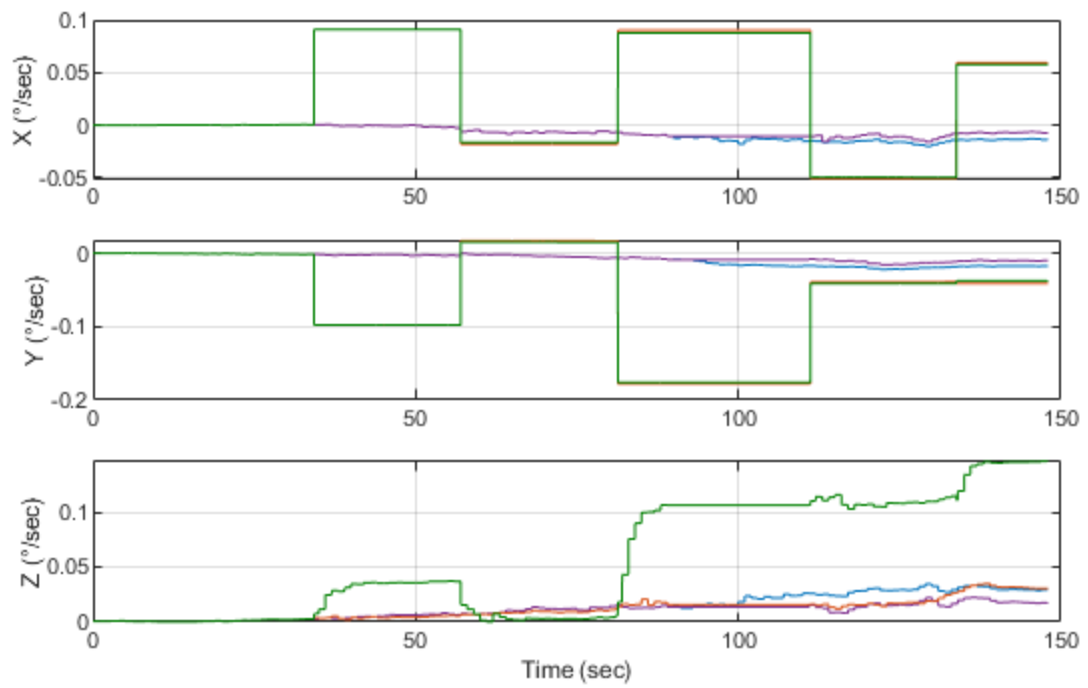


Figure C.3: Dataset 2 gyroscope bias with and without motion constraint

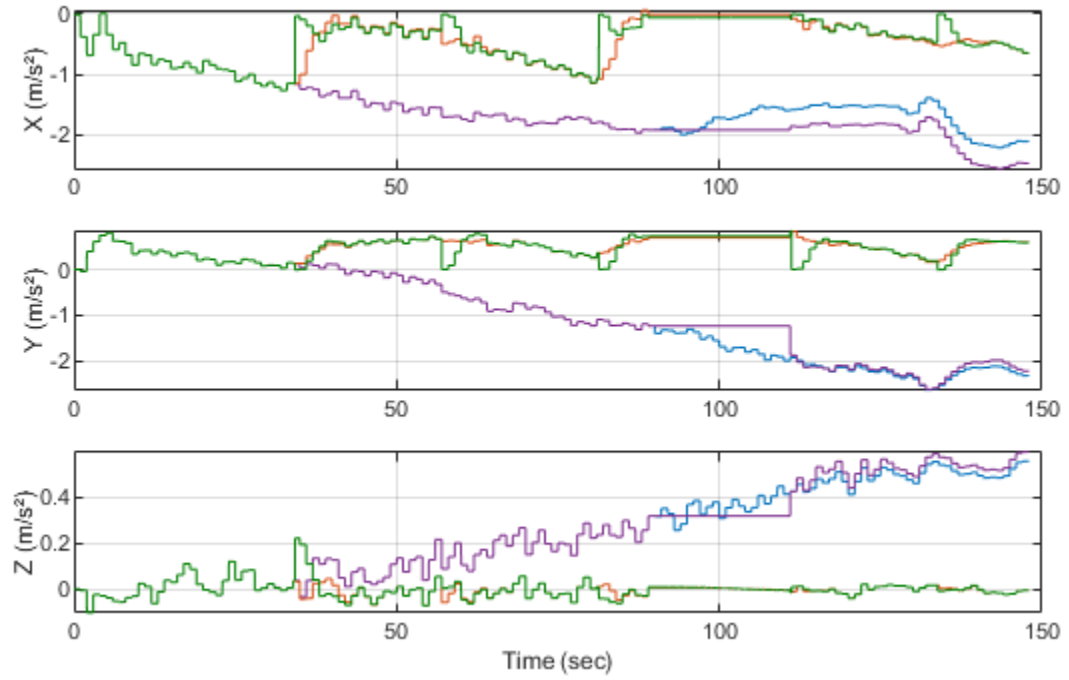


Figure C.4: Dataset 2 Accelerometer bias with and without motion constraints

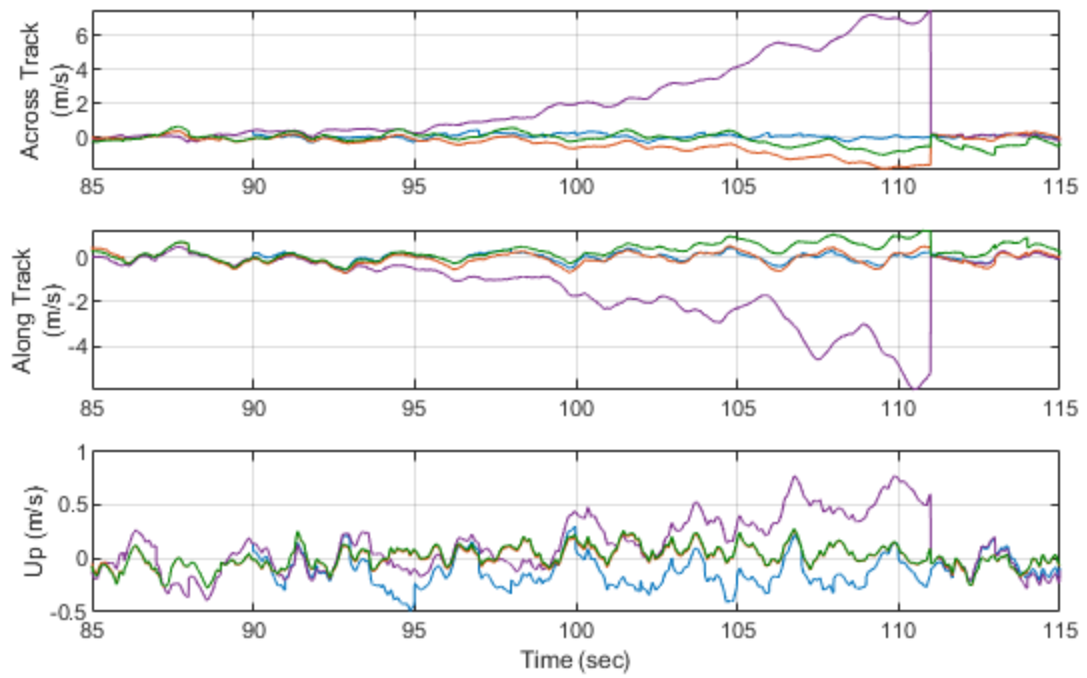


Figure C.5: Dataset 2 velocity errors during a GPS outage with and without motion constraints

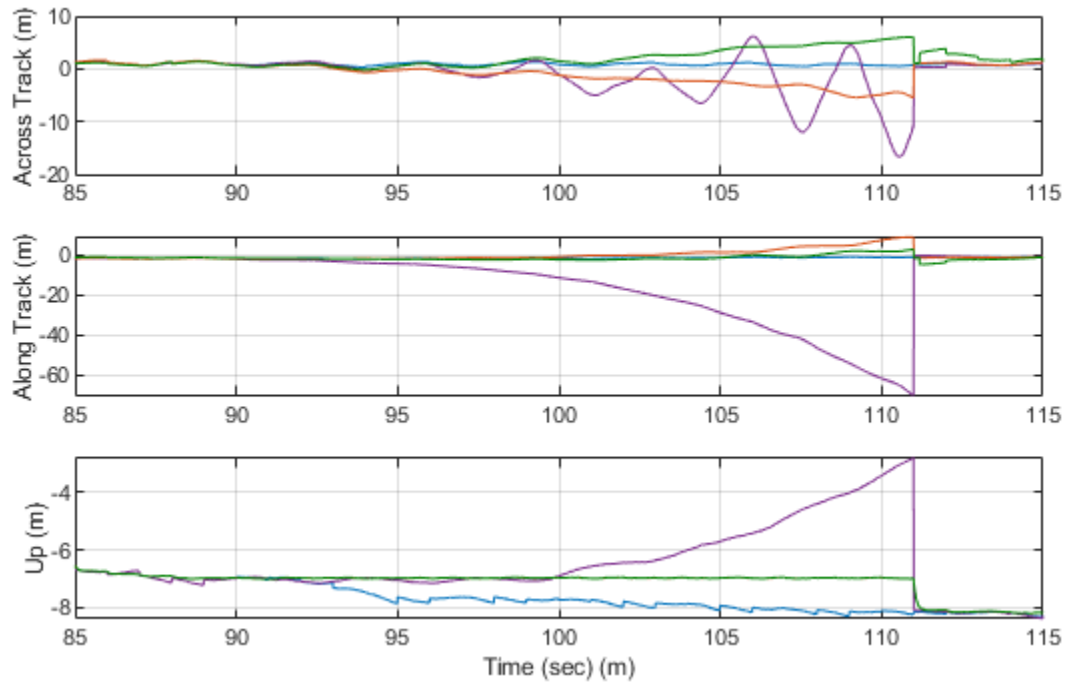


Figure C.6: Dataset 2 position errors during a GPS outage with and without motion constraints

C.2 Dataset 3 Results

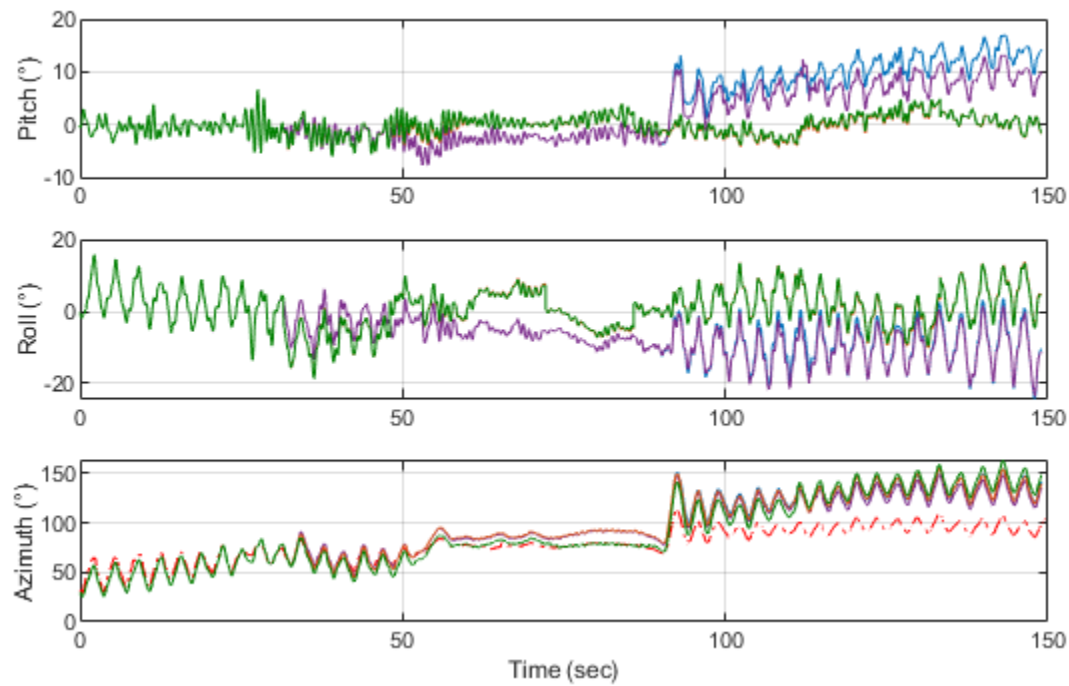


Figure C.7: Dataset 3 attitude with and without motion constraints

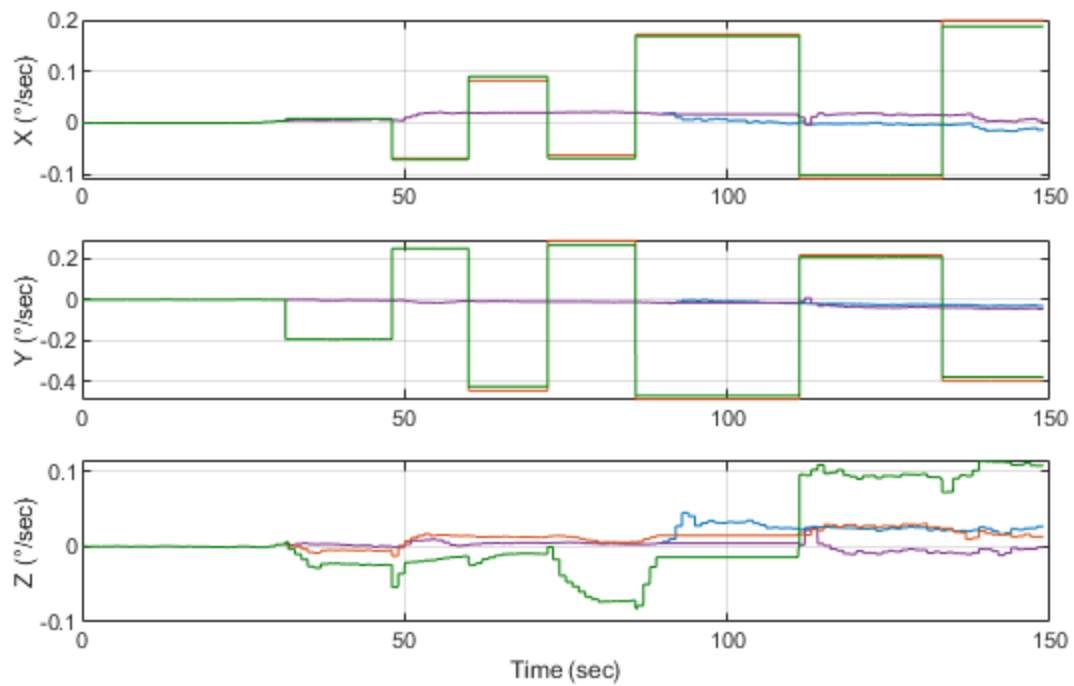


Figure C.8: Dataset 3 gyroscope bias with and without motion constraint

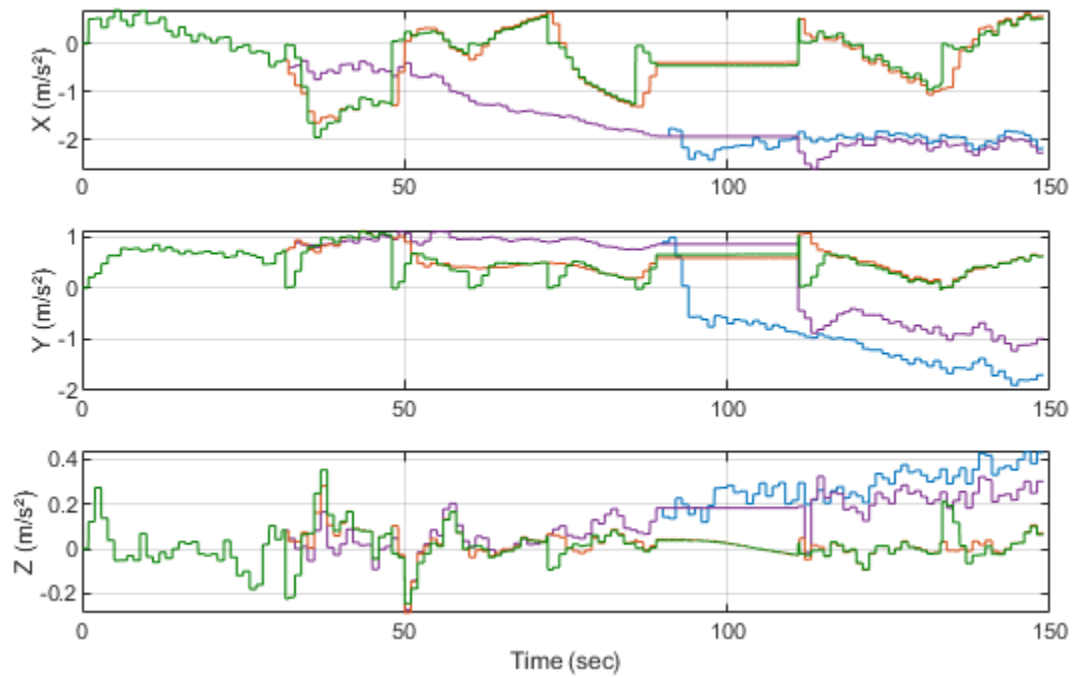


Figure C.9: Dataset 3 Accelerometer bias with and without motion constraints

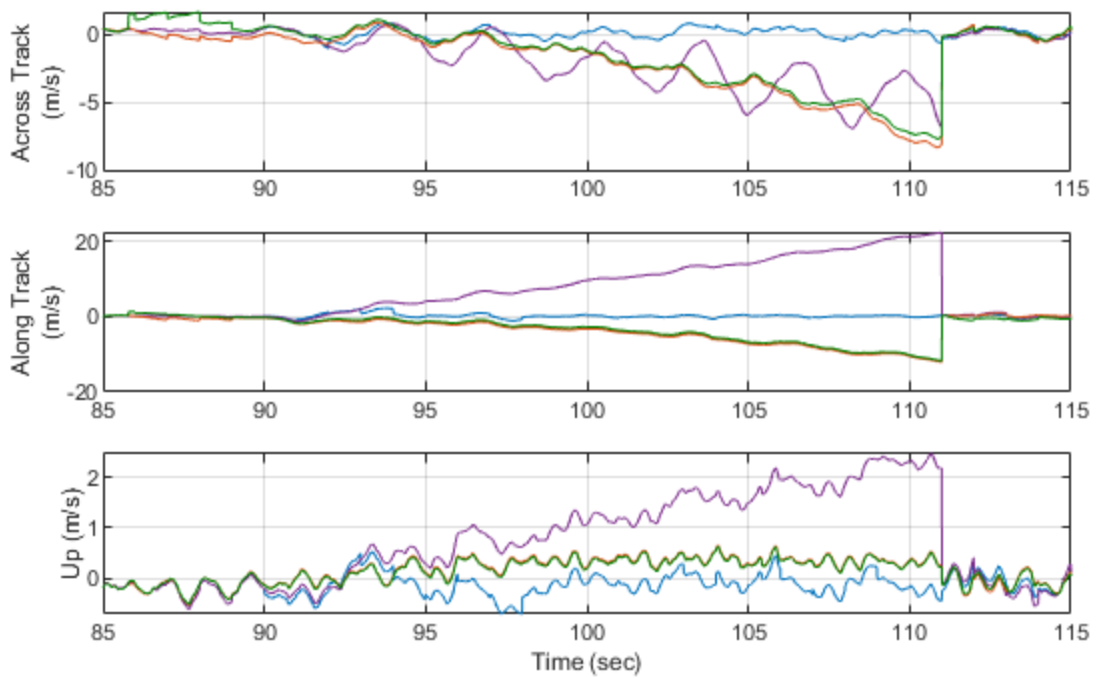


Figure C.10: Dataset 3 velocity errors during a GPS outage with and without motion constraints

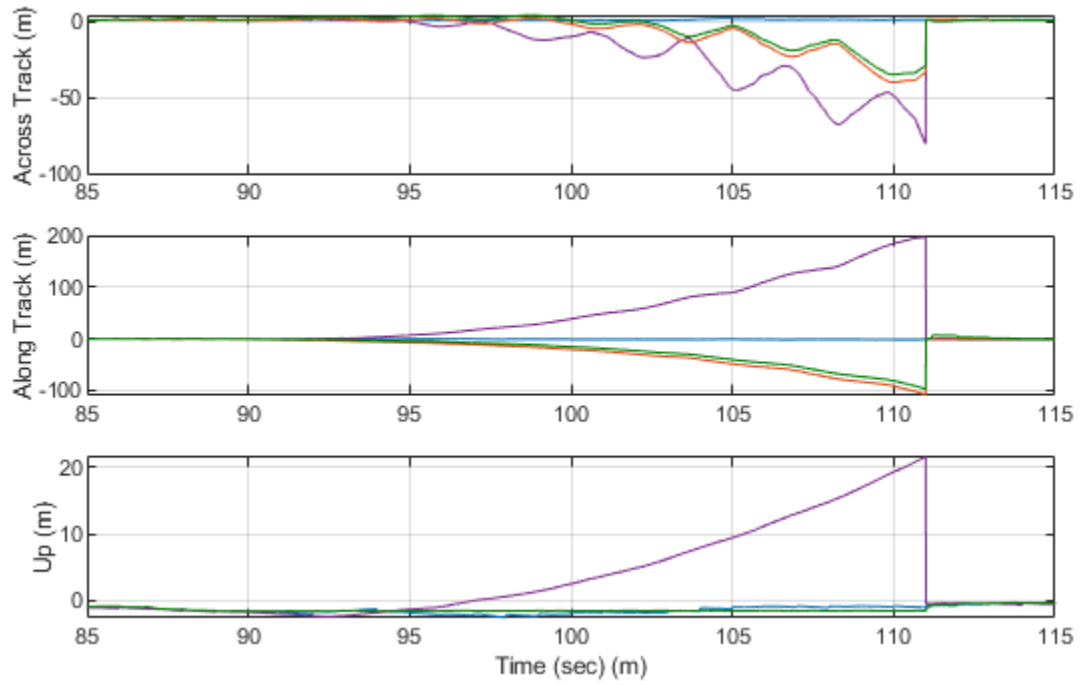


Figure C.11: Dataset 3 position errors during a GPS outage with and without motion constraints

C.3 Dataset 4 Results

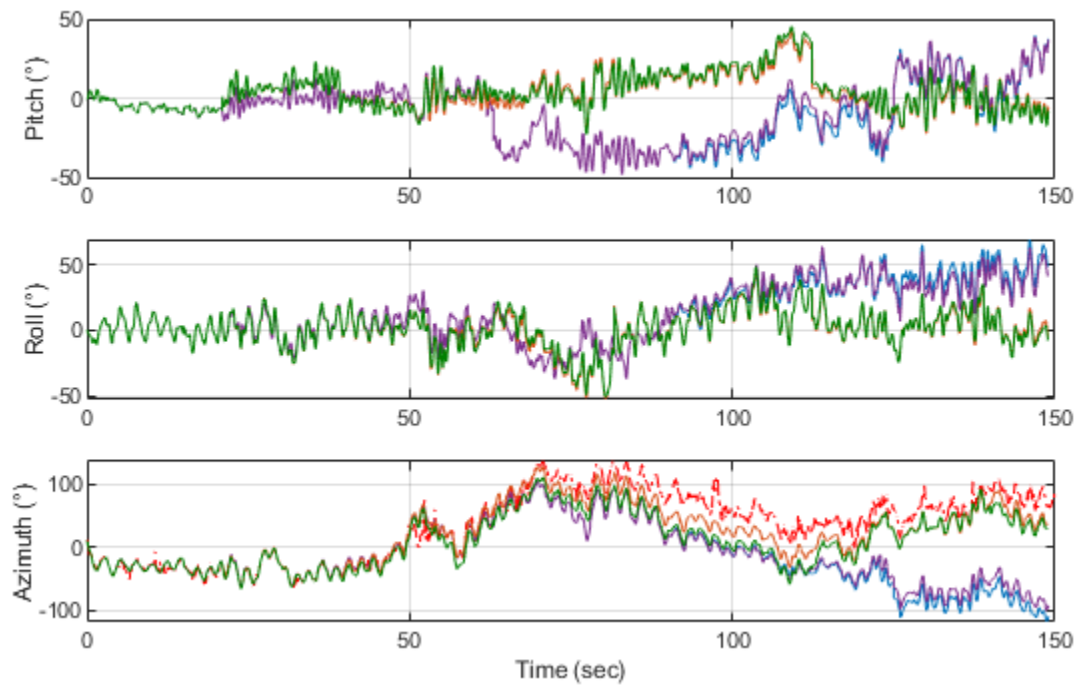


Figure C.12: Dataset 4 attitude with and without motion constraints

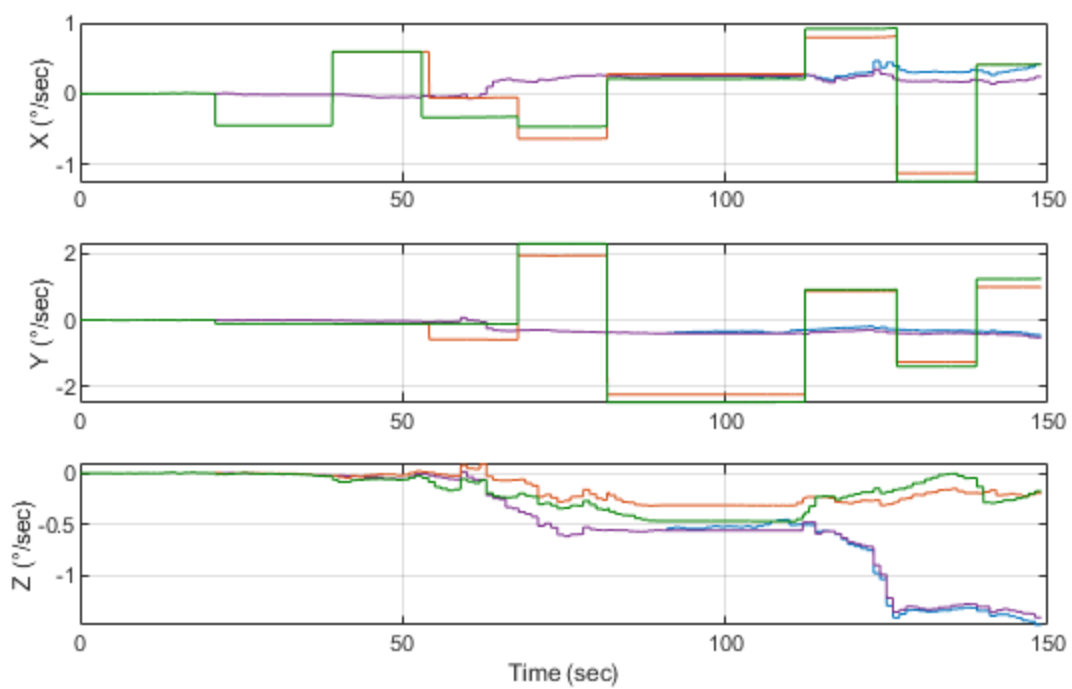


Figure C.13: Dataset 4 gyroscope bias with and without motion constraint

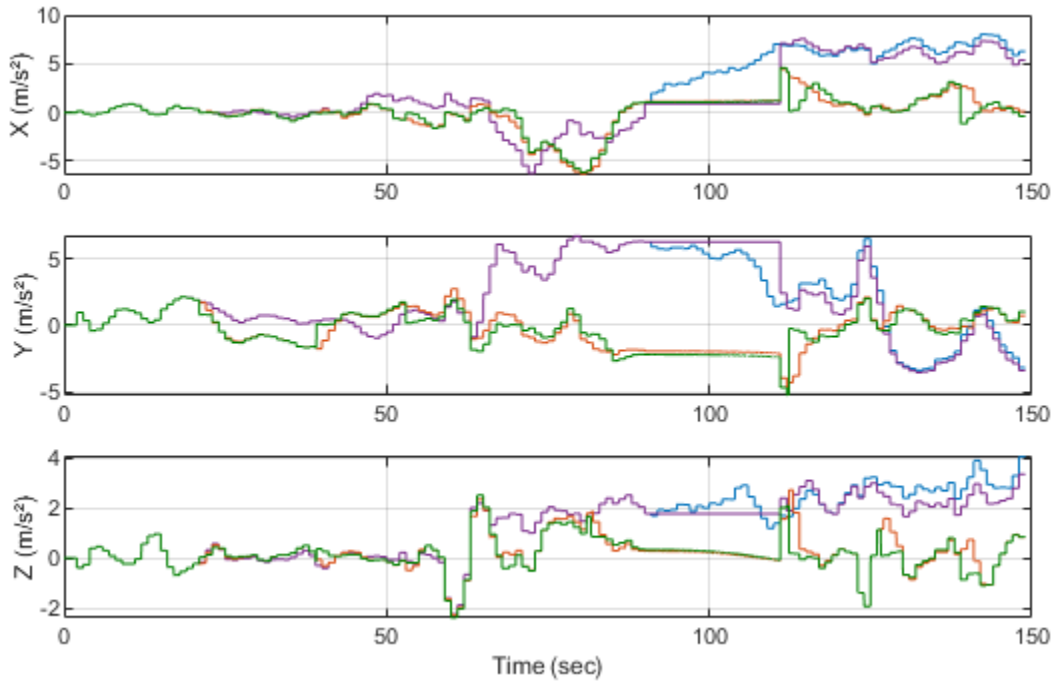


Figure C.14: Dataset 4 Accelerometer bias with and without motion constraints

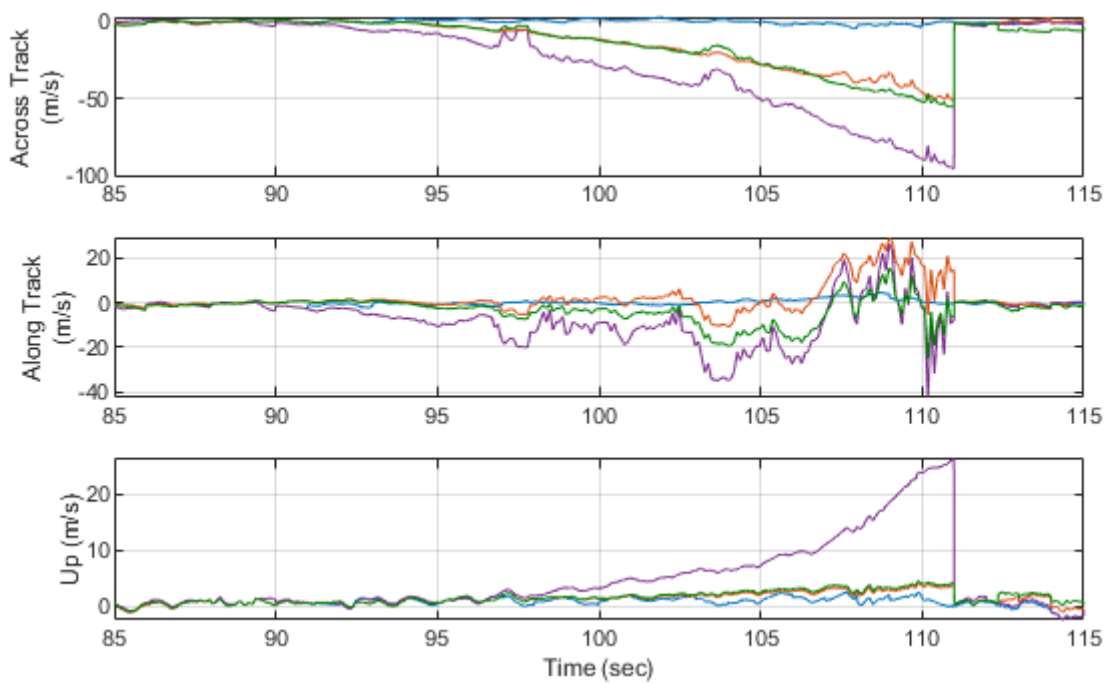


Figure C.15: Dataset 4 velocity errors during a GPS outage with and without motion constraints

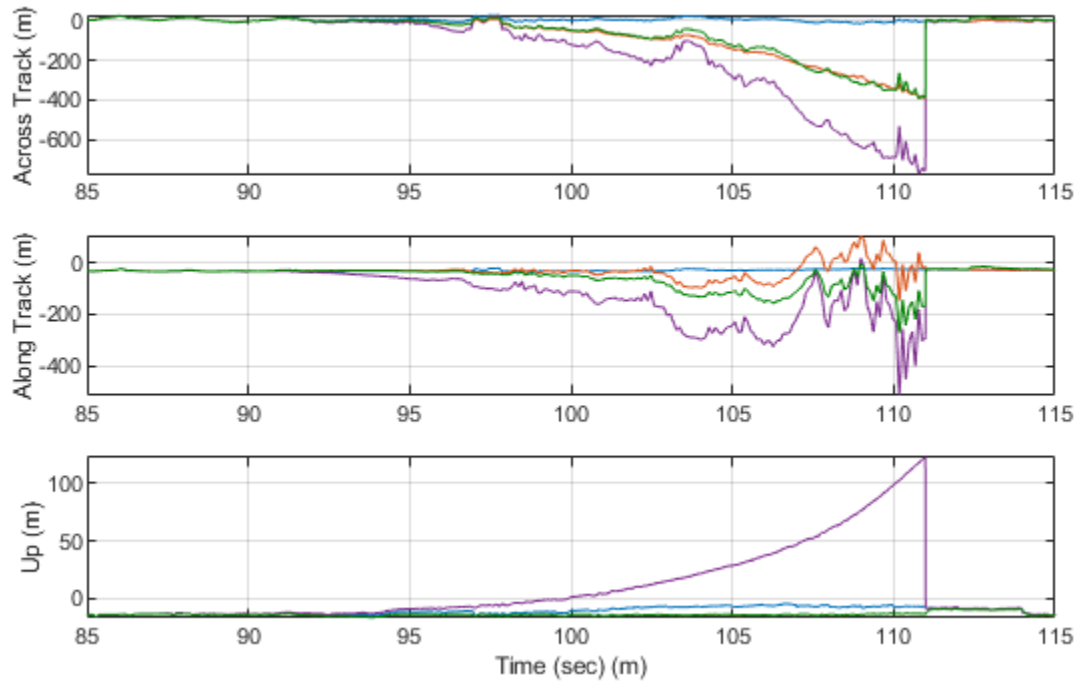


Figure C.16: Dataset 4 position errors during a GPS outage with and without motion constraints